2005

Geomechanics applied to reservoir development in the coso geothermal field

Andrew J. Nygren
University of North Dakota

Recommended Citation

Nygren, Andrew J., "Geomechanics applied to reservoir development in the coso geothermal field" (2005). *Theses and Dissertations*. 213.
https://commons.und.edu/theses/213

GEOMECHANICS APPLIED TO RESERVOIR DEVELOPMENT IN THE COSO GEOTHERMAL FIELD

by

Andrew J. Nygren
Bachelor of Science, University of North Dakota, 2003

A Thesis

Submitted to the Graduate Faculty

of the

University of North Dakota

in partial fulfillment of the requirements

for the degree of

Master of Science

Grand Forks, North Dakota
August
2005

This thesis, submitted by Andrew J. Nygren in partial fulfillment of the requirements of the Degree of Master of Science from the University of North Dakota, has been read by the Faculty Advisory Committee under whom the work has been done and is hereby approved.

Chairperson

This thesis meets the standards for appearance, conforms to the style and format requirements of the Graduate School of the University of North Dakota, and is hereby approved.

Dean of the Graduate School

Date

PERMISSION

Title	Geomechanics Applied to Reservoir Development in the Coso Geothermal Field
Department	Geological Engineering
Degree	Master of Science

In presenting this thesis in partial fulfillment of the requirements for a graduate degree from the University of North Dakota, I agree that the library of this University shall make it freely available for inspection. I further agree that permission for extensive copying for scholarly purposes may be granted by the professor who supervised my thesis work or, in his absence, by the chairperson of the department or the dean of the Graduate School. It is understood that any copying or publication or other use of this thesis or part thereof for financial gain shall not be allowed without my written permission. It is also understood that due recognition shall be given to me and to the University of North Dakota in any scholarly use which may be made of any material in my thesis.

Signature______________________________

Date ______________________________

TABLE OF CONTENTS

CHAPTER

LIST OF FIGURES

LIST OF TABLES

ACKNOWLEDGMENTS

The author expresses sincere appreciation to Dr. Ahmad Ghassemi for serving as the graduate committee chairperson and advisor throughout this project. The knowledge acquired under his tutelage is greatly appreciated. The author also acknowledges Dr. Scott Korom and Dr. William Gosnold for serving on the author's graduate committee.

ABSTRACT

The Coso geothermal field is located approximately 220 kilometers north of Los Angeles, CA. In 2002, a project began to develop the east flank of the Coso geothermal field into an enhanced geothermal system (EGS); in such a system water is injected via injection well(s) into hot dry basement rock through naturally occurring or stimulated fractures. The injected water gathers heat from the reservoir rock before being extracted for direct use or energy production. To develop such a reservoir, adequate understanding of the reservoir geomechanics is necessary. This thesis investigates the state of stress and rock fractures, the existing permeable fractures in the reservoir, and the effects of water injection into fractures at the Coso EGS.

A *lower bound* estimate of the magnitude of the maximum horizontal in-situ stress (S_{Hmax}) was obtained using a fracture mechanics approach incorporating thermal effects on drilling induced fractures in well 38C-9. The maximum principal stress was found to transition from horizontal ($\sigma_1 = S_{Hmax}$) to vertical ($\sigma_1 = S_v$). A fracture propagation study was applied to compare the estimate presented herein with other published estimates that utilized frictional faulting and rock strength theory. The results showed the lower bound estimate resulted in little or no fracture propagation away from the wellbore; published estimates predicted extensive fracture propagation away from the wellbore.

The state of the jointed rock mass was characterized based on formation micro-scanner (FMS) data as they applied to the joint network *fractures with significant aperture* (Rose et al, 2004). The joint network supported the stress regime concluded from the state of stress estimation. A linear and non-linear failure criterion was applied to investigate critically and non-critically stressed joints, also the pore pressure increase required to critically stress non-critically stressed joints was found. At the proposed injection depth, critically oriented joints with friction angles [25° were critically stressed.

A plane strain mathematical model was developed to investigate induced effects of water injection into a permeable deformable fracture. Three fracture geometries were considered: (i) injection/extraction from a line fracture, (ii) injection into an infinite radial fracture, and (iii) injection into a joint. Expressions for the induced pressure and temperature in the fracture and reservoir rock were developed and used to develop expressions for the induced thermoelastic, poroelastic, and combined thermo- and poroelastic fracture width changes, and the resulting induced fracture pressure. Analytic solutions were derived utilizing constant injection and leak-off assumptions.

It was found the poroelastic effects tend to close the fracture as a result of leak-off, while the thermoelastic effects tend to open the fracture as a result of the cold water injection into hot rock. For conditions in the Coso EGS, the thermoelastic effects are dominant. At early times and high injection rates, the poroelastic effects cannot be ignored when considering the induced pressure even though the effects on the fracture width are relatively small. The fluid/solid coupling incorporated into model (iii) can alter the fracture width and pressure.

CHAPTER I

INTRODUCTION

In recent years, there has been an increasing interest in the development of renewable energy resources such as wind, solar, and geothermal energy. Means of harvesting renewable energy sources, for example geothermal energy, have been around for some years. Energy production at the Geysers hydrothermal system, for example, in California began in 1960 producing 11 Mega Watts (MW) of electricity (http://www.eere.energy.gov/geothermal/history.html), and reached production peak in 1987 providing power to 1.8 million people (http://www.eere.energy.gov/geothermal/pdfs/egs.pdf). Since 1987, production has been declining as a result of depletion in water resources (Atkinson, 1998). Another notable example is the Coso geothermal system, which has been in operation since 1981 and currently generates roughly 270 MW of electricity (Monastero, 2002).

Due to continual decline in the Geysers and Coso power output, and in general a growing interest in use of renewable energy, the US Department of Energy has set a goal of producing 20,000 MW by use of the enhanced geothermal system (EGS) concept (http://www.eere.energy.gov/geothermal/pdfs/egs.pdf). The EGS concept involves two or more wells set up in an injection/extraction system (see Figure 1). Injected water travels through natural or man made fractures where it gathers heat (energy) from the surrounding hot crystalline basement rock. The heated water is then extracted for subsequent use.

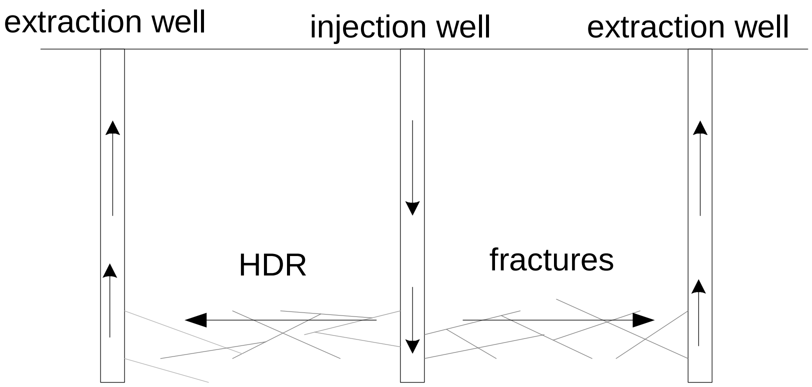

Figure 1: HDR Concept of an EGS Reservoir Energy Extraction System.

The Hot Dry Rock (HDR) concept (see Figure 1) of an EGS has been around since the early 1970s when it was first introduced and patented by scientists at the Los Alamos National Laboratory (Potter et al., 1974) and called HDR (Abe et al., 1999). The total amount of energy available in HDR has been estimated at 10 billion quads (a quad represents the energy equivalent of 180 million barrels of oil, and the US in 2001 used 90 quads) (Duchane and Brown, 2002), which is 300 times greater than the current fossil fuel resource base (Tester et al., 1989). However, early studies showed only a small fraction of this energy could be efficiently extracted. For example, at the Fenton Hill HDR site only 10 MW of energy production was attained. Reasons for this included equipment failure in the high temperature environment and high flow impedance. Impedance is defined as the ratio between the injection and extraction pressure difference to the extraction rate. In general the flow impedance should be less than 1 MPa-s/L (Murphy et al., 1999).

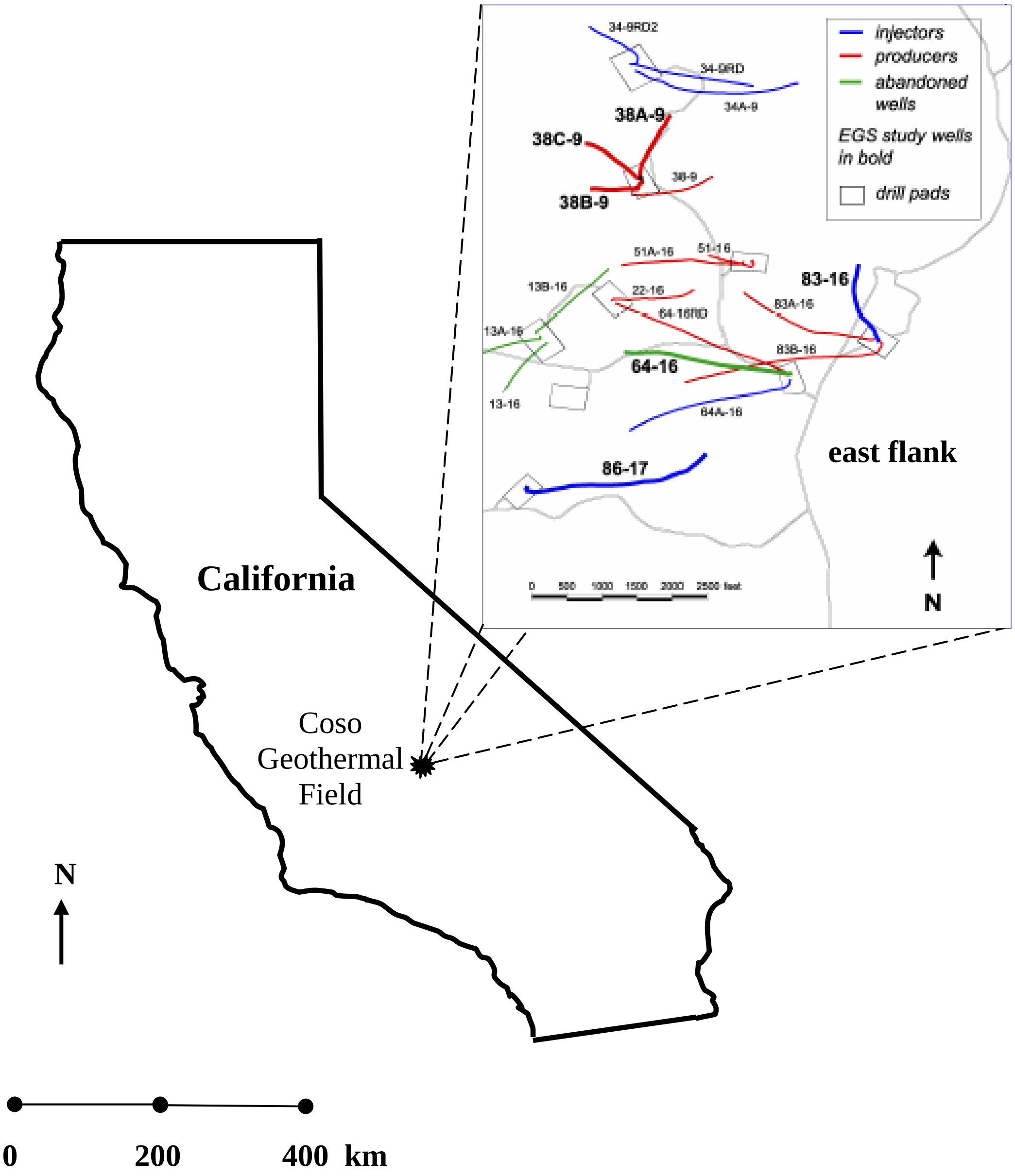

Figure 2. Location of Coso Geothermal Field and Wells (from Rose et al., 2004) in East Flank.

This thesis investigates the reservoir geomechanics of an EGS project at the east flank of the Coso geothermal field (see Figure 2). The investigation includes constraining the in-situ stress tensor, and utilizing it in the characterization of the existing fracture network to identify the critically stressed fractures which can serve as effective fluid pathways for the injected fluid. Furthermore the thesis seeks to understand the mechanical, hydraulic, thermal, and poroelastic effects of injecting water into fractures.

Overview of Coso Geothermal Field

History of Development

The Coso geothermal field is located approximately 220 kilometers north of Los Angeles, California, in Inyo County (see Figure 2). The field is owned by the US government and has been an area of growing interest since the 1960s when Dr. Carl F. Austin published a Navy report on the exploration for geothermal potential. Preliminary tests of heat flow were performed in the mid 1960s and 1970s. By the early 1980s it was established that the reservoir would meet the energy needs of the Naval Weapons Center (NWC) located in the Coso area. By 1990 there were three geothermal plants with a production potential of 250 megawatts. The energy is used by the NWC and the excess is sold to private utilities. Production in the eastern part of the field began in 1993. The eastern part of the Coso Geothermal field has the deepest production well, which is 10,455 feet or 3187 meters.

Geologic Setting

According to Adams et al. (2000), the Coso Geothermal Field has been in existence for roughly 300,000 years. There have been three occurrences of volcanic activity in the system's history. The first began roughly 307,000 year ago and produced low to moderate increases in temperature in the subsurface; little is known about this occurrence. The second resulted from magmatic activity beneath the dome field resulting in a high-temperature geothermal system in the southern and eastern part of the present day field. The third heated the east flank up in excess of 373º K, and reheated the southern part of the field.

The field lies in the eastern part of a major volcanic center that has 38 rhyolite domes. The dome field was subject to volcanic eruptions between 1.0 Ma and 40 ka. The youngest of the domes is Sugarloaf Mountain, which is located immediately to the west of the geothermal field. A fresh phreatic explosion crater surrounds a dome located just north of the field. It is hypothesized that the rhyolite and the geothermal field are related to the magma body located 5-20 km beneath the field. The northern edge of the field follows a northeast trending belt of active and fossil fumaroles. The east flank lies along a northerly trending fault zone (Adams et al., 2000).

History of EGS/HDR Development and Literature Review

A detailed review of the Fenton Hill, Rosmanowes, and Soultz-sous-Forêts EGS/HDR projects can be found in Tenzer (2001). Other reviews on the historical development of the HDR concept include Rummel et al. (1992), Jung et al. (1997), and Baumgartner and Jung (1998).

The HDR version of the EGS concept was largely developed at the Los Alamos National Laboratory (LANL) through experimental tests run at the Fenton Hill site in New Mexico (Hooper and Duchane, 2002). In the LANL HDR model, an injection/extraction system was connected by a single fracture created using hydraulic fracturing. Hydraulic fracturing is a reservoir stimulation technique, which has been used by the petroleum industry since the 1950s. It involves isolating a section of a borehole and pressurizing the section until a mode I (tensile) fracture propagates away from the borehole. Proppants, such as sand grains or synthetic beads, are then pumped into the fracture to keep the fracture open thereby increasing the permeability of the formation. Tests at the Fenton Hill site showed proppants were not needed because the artificial fractures were rough and uneven in the crystalline basement rock. The first test run at Fenton Hill involved an injection/extraction system of a 90 m fracture at a 3 km depth. The results were better than expected with low fluid losses and flow impedances observed. An energy capacity of 3 MW was attained; enough to power several hundred houses. The objective was then to deepen the wells to a 4.5 km depth, where the bottomhole temperature was 600º K, and connect the two deviated (approx. 30º from vertical) wells. Problems were encountered when attempting to increase the distance between the injection and extraction wells and increase the depth. These included mechanical problems attributed to the extremely high temperatures and failure to attain a hydraulic connection. Thus the deviated lower 1 km of the well was filled and the largest hydraulic stimulation operation in US history was conducted. Using the successful experience of utilizing microseismics surveys during injection/extraction operations at the HDR project at the Rosmanowes England; a seismic cloud indicating shear movement on joints was observed in the stimulation process, but a hydraulic connection was not achieved. Therefore the extraction well was deviated to intersect the seismic zone. Once connection was made the system yielded a capacity of 10 MW.

As already alluded to, the HDR project at the Rosmanowes Quarry in Cornwall, England used microseismics surveys during injection/extraction operations (subsequently used at the Fenton Hill site). During injection tests, a seismic cloud around the injection points was noted. This suggested a reservoir stimulation mechanism that differed from the early tests run at the Fenton Hill site. It was concluded that reservoir stimulation was a result of slip of existing joints rather than propagation of single hydraulically driven fracture. There are two main reasons for this. The first is that in most HDR, an existing joint network dominates the permeability because the matrix permeability is extremely low. The second is that sites favorable for HDR are tectonically active areas. The result is shear loading on joints creating conditions favorable for joint slip. Pine and Batchelor (1984) used the stress tensor of the Rosmanowes Quarry (a tectonically active area) and Mohr-Coulomb failure theory, and found slip can occur on critically oriented joints at pressures significantly below that required to hydraulically jack a joint. The three well system at Rosmanowes was studied for over three years. Circulation was ceased after it was recognized that heat was no longer being extracted along the flow path due to channeling of the flow.

Although the Fenton Hill and Rosmanowes site are no longer operational, they provided a framework for future HDR work. Notably the Fenton Hill site showed the HDR concept can be used to produce energy, and hydraulic fracturing in HDR environments may not require proppants. The Rosmanowes site showed that in HDR type environments flow through natural fractures is the dominant flow mechanism. Also, the Rosmanowes site showed slip of existing fractures can be a stimulation technique (rather than hydraulic fracturing), and can be monitored by use of microseismics.

The most noteworthy current HDR/EGS site is the Soultz-sous-Forêts site in France. This project began in 1987 with the drilling of a 2 km deep well. The temperature of the reservoir at 1 km depth was 394º K and at 2 km depth was 414º K, which indicated much of the heat was not flowing from the basement rock. It was concluded the heat was flowing from water circulation in the overburden sediment. The seismic data from hydraulic stimulation tests indicated an activated north-south trending fracture system. Accordingly, from 1989-1991 a second well was drilled to intersect this activated fracture system. During 1992 and 1993 the first main hole was deepened to a target depth of 3590 m, and the subsequent gathered data were used to deepen the second hole to 3890 m approximately 450 m south of the main hole. After completion, large scale production tests yielded positive results producing 8 MW of power. Recent work has been aimed at increasing the depth of the system to 5 km, and construction of an HDR power plant to hopefully generate 30 MW of power for commercial use.

Another recent project in the 1990s is the Dixie Valley EGS site in Nevada which expanded the results of Pine and Batchelor (1984) and showed these critically oriented fractures, when critically stressed, controlled permeability in areas of active tectonics (Barton et al., 1998). This is a quality of the Coso geothermal system. Therefore, accurate characterization of the reservoir geomechanics including the in-situ stress, existing jointing network, and prediction of the pressures at which these fractures will slip, as well as propagate is necessary for optimum development of an EGS.

Heat Extraction in EGS

The goals of geothermal reservoir modeling are to quantify the amount of energy the injected fluid can withdraw from the reservoir rock and to estimate how long energy can be economically extracted from the reservoir. Realization of this goal can benefit from understanding those mechanisms that control fracture permeability. This is achieved in this thesis by considering a single fracture to isolate and identify the fundamental mechanisms.

The single fracture approach has also been used in studying heat extraction potential in a reservoir. Early analyses of a single fracture assumed one-dimensional heat flow to allow for analytical solutions in impermeable (Bodvarsson, 1969) or permeable (Cheng and Ghassemi, 2001) rock. More complicated two- or three-dimensional semi-analytical solutions of heat extraction have utilized the boundary element method (e.g. Cheng et al., 2001 or Ghassemi et al., 2003) or finite element method (e.g. Kolditz, 1995; Kohl, 1995; Bower, 1997; Kolditz and Clauser, 1998). These studies have shown that the one-dimensional simplification can give erroneous results for large values of time.

Influence of Cold Water Injection in EGS

The behavior of fractures in response to injecting cold water has not been extensively studied with respect to EGS. The effects are mechanical, hydraulic, thermal, poroelastic, and chemical. These effects are typically coupled together and non-linear. Hydraulic effects (which have already been discussed) can be found in Pine and Batchelor (1984) or Hayashi and Ito (2003). Recent investigations of the thermal effects include Mossop and Segall (in-press), and Ghassemi et al. (2005). These works found the thermally induced stresses can dwarf the hydraulic effects of injection. Their results showed the thermoelastic induced stresses can play a dominant role in slip of existing joints. Ghassemi and Zhang (2004) studied the influence of poroelastic and thermoelastic processes on fracture width and pressure using a fully coupled model of a uniformly pressurized and cooled crack. However, the resulting changes in the fracture width pressure resulting from injection/extraction have not been addressed and are studied in this thesis.

Objectives and Methodology

The objectives of this study are:

1) Constrain the in-situ stress tensor in the east flank of the Coso EGS
2) Characterize the fracture network in the east flank of the Coso EGS
3) Identify critically stressed or least stable joint orientations in the east flank of the Coso EGS
4) Develop a mathematical model to investigate the role of various mechanisms in slip of existing joints; and also to address changes in fracture width and pressure resulting from elastic, thermoelastic, and poroelastic effects associated with cold water injection into a fracture.

These objectives are intrinsically related. The fracture network cannot be characterized without knowledge of the in-situ stress tensor. The critically stressed fractures cannot be identified without use of the in-situ stress tensor and the characterized fracture network. Finally, the mathematical model must be based off the identified critically stressed fractures.

Sign Convention and Units

In this thesis, compressive stress will be assumed positive, and tension will be assumed negative. This is done for continuity with conventional rock mechanics literature (e.g. Jaeger and Cook, 1976). The in-situ stress tensor will be calculated in U.S. customary units. This is for continuity in comparison with the other published in-situ stress estimates. However, SI units will be used for subsequent chapters of the thesis. For convenience the final summary of the estimated in-situ stress tensor is given in both SI and U.S. customary units.

CHAPTER II

IN-SITU STRESS ESTIMATION

Introduction

In early HDR projects, such as the Rosmanowes site, in-situ stress measurements were conducted using traditional methods already used by the petroleum and mining industry. The overburden stress (S_v) was measured using density logs, which is still the method used today. The minimum horizontal stress (S_{hmin}) was measured using hydraulic fracturing (see e.g. Pine et al., 1983), a method used in the petroleum industry since the late 1950s. Background on the fundamentals and theory of hydraulic fracturing stress measurements can be found in Hubbert and Willis (1957), Haimson and Fairhurst (1967), or Haimson (1968). The maximum horizontal stress (S_{Hmax}) was typically extrapolated via the Kirsch solution. However, EGS can be highly fractured. Therefore, use of the Kirsch solution in estimating S_{Hmax} seems unreasonable, because the Kirsch solution assumes linearly elastic, isotropic, homogeneous, impermeable rock. Therefore fracture mechanics methods incorporating pre-existing fractures were developed to account for this (e.g. Zoback et al., 1977; Rummel, 1987; and Abou-Sayed et al., 1978).

Recent techniques involving borehole imaging of drilling-induced tensile fractures and borehole breakouts have lead to effective methods in constraining the orientation of the in-situ stress tensor (see e.g. Moos and Zoback, 1990; Barton and Zoback, 1994; Brudy and Zoback, 1999; and Sheridan et al., 2003). A breakout is compressional failure at the borehole wall, and drilling induced tensile fractures are tensile failure at the borehole wall (see Figure 3). Both are functions of the material properties of the rock and the state of stress. By the Kirsch solution a breakout will occur at the zone of maximum compressional stress, which is in the direction of S_{hmin}. While drilling-induced tensile fractures will initiate at the zone of minimum compressional stress in the direction of S_{Hmax}.

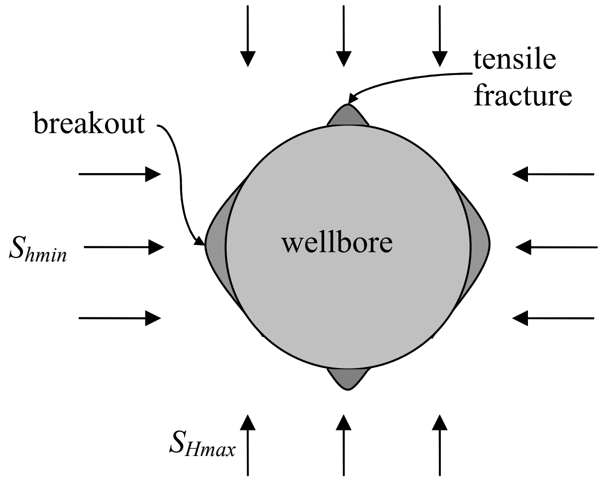

Figure 3. A Borehole Breakout and Drilling-Induced Tensile Fracture.

Previous Work at Coso Geothermal Field

For the Coso geothermal reservoir, the in-situ stress orientation has been constrained by Hickman and Sheridan (2004). The direction of S_v is assumed to be perpendicular to Earth's surface. The direction of the two horizontal principal stresses, S_{Hmax} and S_{hmin}, are then found by considering the orientations of drilling-induced tensile fractures in well logs. With the orientations of S_{Hmax} and S_v constrained, the orientation of S_{hmin} is determined as it must be orthogonal to S_{Hmax} and S_v. The S_{hmin} direction can also be determined by considering breakouts in well logs.

The magnitude of S_v can be estimated simply by using density well logs with the following equation:

$$S_v = \int_0^z \rho(z) g dz \tag{1}$$

where g is the acceleration due to gravity, z is the depth below the surface of the earth, and $\rho(z)$ is the density which can be a function of depth. In Coso, S_v was found to be 1.14 psi/ft (Sheridan et al., 2003). S_{hmin} can be estimated with reasonable accuracy by analysis of micro- or mini-hydraulic fracturing (HF) tests. The analysis of HF testing in well 38C-9 (see Figure 2) yielded a value of 0.66 psi/ft. Unfortunately, it is not as straight-forward to determine S_{Hmax}.

S_{Hmax} Estimation

Determination of S_{Hmax} Using Kirsch Solution

S_{Hmax} often is found indirectly by using the results of HF tests. This is done by considering the Kirsch solution for a circular wellbore in elastic rock. The result is the well known Hubbert and Willis (1957) equation:

$$S_{H\max} = 3S_{h\min} + T - p_b - p_o \tag{2}$$

where p_o is the pore pressure, T is the tensile strength of the rock, and p_b is the breakdown pressure. The benefits of this solution are that it is quick, easy, and, if conditions are right, can provide a fairly accurate measurement of S_{Hmax}. On the other hand, (2) assumes linearly elastic, isotropic, homogeneous, and impermeable rock, which is not always the case. Application of this equation to the HF test conducted at 3703 ft with values in Table 1 for well 38C-9 in Coso yields a value of 4941 psi at 3703 ft or 1.33 psi/ft assuming a linear stress gradient.

Table 1: Parameters Used for a Depth of 3703 ft.

Parameter	**Value**	**Reference or comments**
S_{hmin}	2444 psi	From HF test in well 38C-9
S_{Hmax}	S_{Hmax} (psi)	
p_{frac}	1234 or 1629 psi	Assumed equal to p_w or p_o
p_o	1234 psi	Sheridan et al., 2003
p_w	1629 psi	0.44 psi/ft gradient assumed
T_o	436 ºK	Well 38C-9 static survey
T_w	383 ºK	Drilling report
v	0.185	Rose et al, 2004
E	$9.43(10^6)$ psi	Rose et al, 2004
η	0.183	Calculated
α_T	$8(10^{-6})$ 1/ºK	Assumed for granite
r	6.125 in	38C-9 well log
k_T	0.00147 in^2/s	Assumed for granite
K_{IC}	1820 psi-$\text{in}^{1/2}$	Assumed for granite
p_b	1334 psi	HF test in well 38C-9
T	177 psi	HF test in well 38C-9

The thermoelastic effects can be accounted for by applying the principle of superposition and adding the induced thermal stresses to the elastic stress concentration. At the borehole wall the induced thermal stress is (Ritchie and Sakakura, 1956):

$$\sigma_{\theta\theta}^{\Delta T} = \frac{\alpha_T \mathrm{E} \Delta T}{1-v} \tag{3}$$

where α_T is the linear expansion coefficient, v is Poisson's ratio, ΔT is the temperature difference between the well and rock, and E is Young's modulus. Adding Eqn. (2) to (3) yields the Stephens and Voight (1982) thermoelastic solution for S_{Hmax}:

$$S_{H\max} = 3S_{h\min} + T - p_b - p_o + \frac{\alpha_T \mathrm{E} \Delta T}{1-v} \tag{4}$$

Eqn. (4) with the values in Table 1 yields a value of 35 psi at 3703 ft for S_{Hmax}. This is not reasonable. Adding poroelastic effects to (4) results in:

$$S_{H\max} = 3S_{h\min} + T - 2p_b(1-\eta) + \frac{\alpha_T \mathrm{E}\Delta T}{1-\nu} - 2\eta p_o \tag{5}$$

Eqn. (5) yields -36 psi (in tension) at 3703 ft, which is also unreasonable. Aside from the inherent limitations in elastic (or other constitutive models, i.e., thermoelastic, and/or poroelastic) stress analysis, this method is not reliable because it assumes that breakdown corresponds to tensile failure of the rock and fracture initiation. Often times this is not the case and breakdown pressure represents propagation of a pre-existing crack. A fracture mechanics approach considers a priori the existence of a critically oriented fracture at the wellbore wall, and views the breakdown as the beginning of unstable fracture propagation (Abou-Sayed et al., 1978; Detournay and Carbonell, 1994). Due to the high degree of fracturing in EGS environments this approach is more applicable. Fracture mechanics principles provide a framework for analysis of drilling-induced cracks.

Estimating S_{Hmax} from Drilling-Induced Fractures

The existence of a drilling induced fracture at 7650 ft, as shown in Figure 4, allows for S_{Hmax} estimation using a fracture mechanics approach. Drilling-induced cracks are mode I fractures that occur vertically in a fracture doublet 180° apart (Moos and Zoback, 1990; Sheridan et al., 2003). Rummel (1987) established a fracture mechanics analysis of drilling-induced tensile fractures under isothermal conditions. This considered loadings on the fracture which included S_{hmin}, S_{Hmax}, the wellbore pressure (p_w), and the fluid pressure in the fracture (p_{frac}). The latter can be equal to the wellbore pressure, the formation pore pressure, or some other distributed pressure. Thermally induced stresses from cooling of the formation by drilling mud can also be included (Brudy and Zoback, 1999).

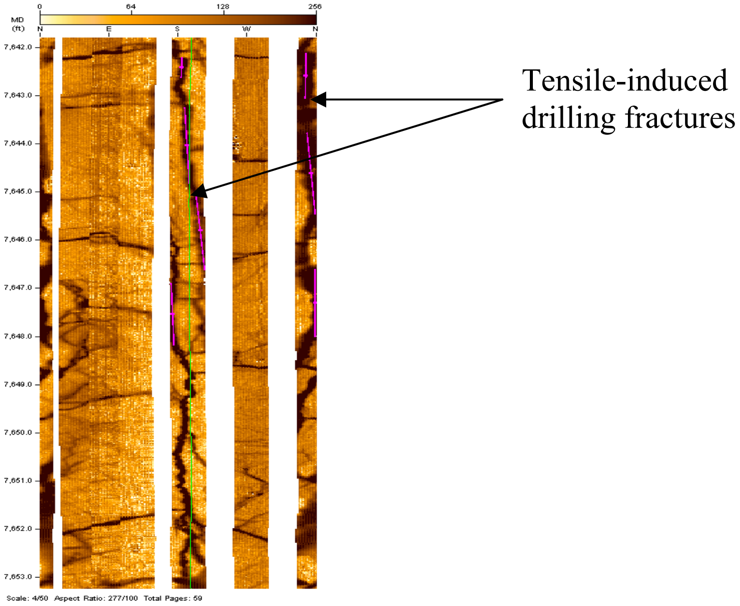

Tensile-induced drilling fractures

Figure 4. The Drilling-Induced Tensile Fracture Noted at 7650 ft. The Vertical Fracture Occurs in a Pair 180º Apart (from Sheridan and Hickman, 2004).

In order to predict the conditions for propagation of the fracture, the mode I stress intensity factor (K_I) is considered and compared to the rock's fracture toughness (K_{IC}). K_I is calculated by adding the contribution of various loads in Figure 5 based on the principle of superposition (Rummel, 1987; Brudy and Zoback, 1999). This will result in the following equation for K_I:

$$\begin{aligned} K_I(S_{H\max}, S_{h\min}, p_w, p_{frac}, \sigma_{\theta\theta}^{\Delta T}) &= K_I(S_{H\max}) + K_I(S_{h\min}) \\ &\quad + K_I(p_w) + K_I(p_{frac}) + K_I(\sigma_{\theta\theta}^{\Delta T}) + K_{IC} \end{aligned} \tag{6}$$

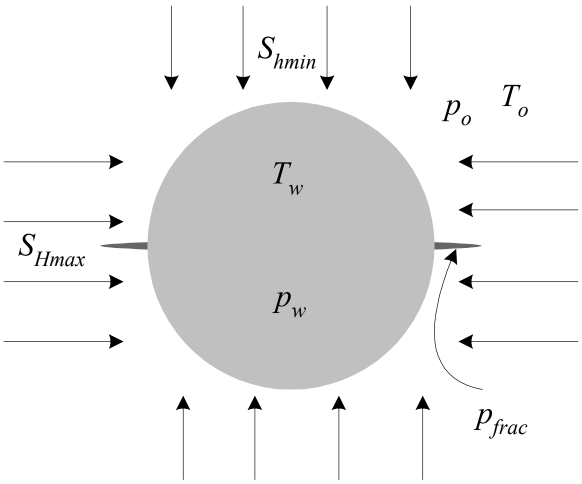

Figure 5. Problem Set up for S_{Hmax} Determination.

K_I defines the state of stress at the tip of a crack and is a function of the applied loading and geometry. In considering different loadings in Figure 5, we assume the geometry in Figure 6 for which Paris and Sih (1965) derived the following expression for K_I:

$$K_I = \sqrt{\pi a}\int_{-a}^{a} \sigma_y(x,0)\sqrt{\left(\frac{a+x}{a-x}\right)}dx \tag{7}$$

where σ_y is the loading on the crack plane. From (7) the expressions for the stress intensity factor caused by the different loadings (S_{Hmax}, S_{hmin}, p_w, p_{frac}, and $\sigma_{\theta\theta}^{\Delta T}$) can be established. The Kirsch solution is used to calculate the loads due to S_{hmin} and S_{Hmax}. Once the σ_y for each loading is established, it is substituted into Eqn. (7) and integrated resulting in the following expressions (Rummel, 1987):

$$K_I(S_{H\max}) = -2S_{H\max}\sqrt{r}\left(b^2 - \frac{1}{\pi b^7}\right)^{1/2} \tag{8}$$

$$K_I(S_{h\min}) = -S_{h\min}\sqrt{r}\left[(\pi b)^{1/2}\left(1-\frac{2}{\pi}\sin^{-1}\frac{1}{b}\right) + 2(b^2+1)\left(\frac{b^2-1}{\pi b^7}\right)^{1/2}\right] \tag{9}$$

$$K_I(p_w) = p_w\sqrt{r}\left(1.3\frac{b-1}{1+b^{3/2}} + 7.8\frac{\sin[(b-1)/2]}{2b^{5/2}-1.7}\right) \tag{10}$$

$$K_I(p_{frac}) = p_{frac}\sqrt{r}\left[(\pi b)^{1/2}\left(1-\frac{2}{\pi}\sin^{-1}\frac{1}{b}\right)\right] \tag{11}$$

where $b = 1.0+(\alpha/r) = a/r$.

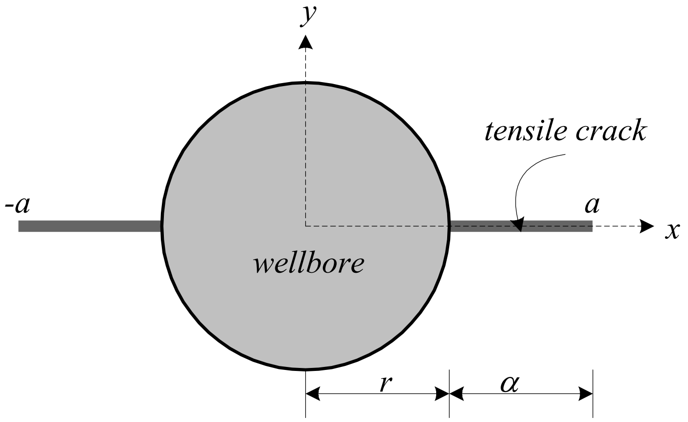

Figure 6. Geometry of Crack Considered by Paris and Sih (1965) for Calculation of Stress Intensity Factor.

This approach has been expanded by Brudy and Zoback (1999) to include the influence of the tangential thermal stresses. In this approach it is assumed the fracture never reaches the cooling front in the formation, because if the fracture goes beyond this point the tensile thermal stresses no longer act on the fracture. In their work, Brudy and Zoback (1999) obtain:

$$\begin{aligned} K_I(\sigma_{\theta\theta}^{\Delta T}) = \sigma_{\theta\theta}^{\Delta T}\sqrt{r}\left(\frac{1}{2}+\frac{1}{2}I_0^{-1}\right)\sqrt{\pi b}\left(1-\frac{2}{\pi}\sin^{-1}\left[\frac{1}{b}\right]\right) \\ +(1-I_0^{-1})\sqrt{\frac{b}{\pi}}\sqrt{b^2-1}-I_0^{-1}\sqrt{\pi b}\ln b \end{aligned} \tag{12}$$

$$I_0^{-1} \cong \frac{1}{\pi}\tan^{-1}\left(\frac{\pi}{B}\right)+\frac{-0.5772}{(\pi^2+B^2)}+\frac{1.9781B}{(\pi^2+B^2)^2} \tag{13}$$

$$B \cong \ln(1.26094\tau^*) \tag{14}$$

where $\tau^* = \frac{k_T T_c}{r^2}$, $\sigma_{\theta\theta}^{\Delta T} = \frac{\alpha_T \mathrm{E}\Delta T}{1-v}$ in which ΔT now is the difference of *the in-situ formation temperature and the formation temperature after cooling*, τ^* is the Froude number, B is the cooling front, T_c is the time of cooling, and k_T is the thermal diffusivity. Eqn. (12) is only valid if $T_c > 20$ hours (Stephens and Voight, 1982). Eqns. (8)-(14) are substituted into (6) and solved for S_{Hmax}. First, it is necessary to establish ΔT and T_c.

Determination of ΔT *and Cooling Time*

The temperature change is a key parameter in this analysis, and can be approximated based on the temperature record of the circulating mud. The temperature of the mud is often recorded at the surface. T_{out} is the temperature of the mud coming out of the well, and T_{in} is the temperature of the mud after returning to the annulus. These can serve to establish the extent to which the rock has been cooled. To do so, the following assumptions are made:

1) Fluid loss is neglected i.e. $q_{in}=q_{out}$.
2) Heat transfer from the formation to the mud is 100% efficient ($Q_{mud}=Q_{form}$)
3) Convective heat generation from the circulating mud is negligible.
4) The geothermal gradient is constant.
5) Heat transfer behaves the same for the mud entering and leaving the well.

These assumptions are illustrated in Figure 7. Applying these assumptions, the change in the formation temperature based on drilling reports is found to be 29º K.

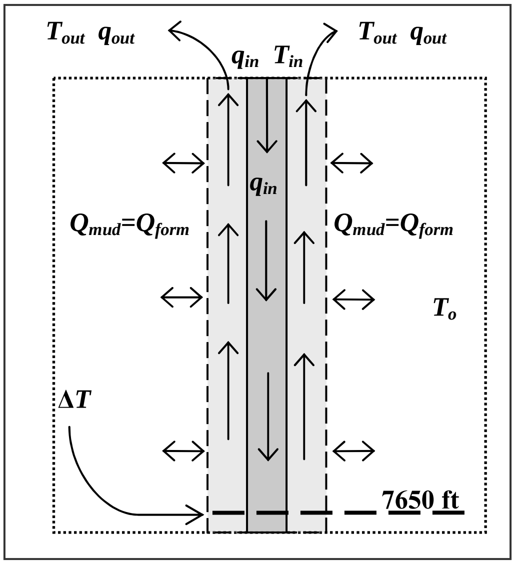

Figure 7. Idealized Mud Circulation in Well.

Due to incomplete data, T_c must also be estimated. This is achieved by considering the problem of cooling the formation around the wellbore as a function of mud circulation. A simple solution to this problem was presented by Edwardson et al. (1962). It assumes an infinite and homogeneous formation and neglects the effects of a mud cake, convective heat generation, and rate of radial heat flow from the wellbore once mud circulation ceases. Applying these assumptions Edwardson et al. (1962) solved the heat conduction equation given as:

$$\frac{\partial^2 T}{\partial r^2} + \frac{1}{r_D}\frac{\partial T}{\partial r_D} = \frac{\partial T}{\partial t_D} \tag{15}$$

where $r_D = \frac{a}{r}, t_D = \frac{K_r t}{c_{mud}\rho_{mud} r^2}$, K_r is the thermal conductivity of the formation, c_{mud} is the heat capacity of the mud, and ρ_{mud} is the density of the mud. The solution to (15) gives the temperature distribution as a function of radial distance and time (Edwardson et al., 1962):

$$\frac{\Delta T(r_D,t)}{\Delta T(0)} = q(0)P(r_D,t_D) + \sum_n \delta q(t_{Dn})P(r_D,t_D - t_{Dn}) \tag{16}$$

where $\Delta T(0)$ is the difference in temperature between the undisturbed formation and the drilling fluid, $\Delta T(r_D,t)$ is the temperature difference between the circulating fluid and the formation after some time (t) of cooling at some distance, r_D. The functions q and P are known functions with values given in Edwardson et al. (1962). In our case, the radial distance is known (r_D = 1), along with the ratio $\frac{\Delta T(r_D,t)}{\Delta T(0)} = \frac{29^\circ K}{434^\circ K}$, which is found using a static well log and from assumptions given above. The $\Delta T(0)$ value is obtained by taking the difference between the T_{in} of the mud and the undisturbed formation temperature. Therefore, the only unknown is the time (t) it takes to obtain the temperature disturbance of 29ºK / 434ºK.

A simple method for determining this time is proposed by Edwardson et al. (1962). The method requires knowledge of the total time since drilling past the depth of interest (7650 ft), and the well temperature at that depth at the end of that time period. This was determined using the static well log conducted after well completion. If the static well log is assumed to be representative of the temperatures immediately after well completion; the time since drilling past 7650 ft is found to be approximately 11 days or 264 hours (based on daily drilling reports). Then, based on the average annular mud velocities, the amount of circulation time is found to be 148 hours. The remaining time (116 hours) is assumed to correspond to the well being shut-in prior to measuring the equilibrium well temperatures.

The value of T_c is estimated iteratively. An initial guess for the cooling time is used to calculate the ratio $[(t+T_c)-t_{circ}]/t$ where t is the total time and t_{circ} is the circulation time. This ratio and the initial guess is read off graphs given in Edwardson et al. (1962) to yield a temperature disturbance, dT_1. Next, the ratio $[(t_{circ}+T_c)-t_{circ}]/t_{circ}$ is calculated and the corresponding temperature disturbance, dT_2 is read off the graph. The average of dT_1 and dT_2 is then used as the final temperature disturbance, dT_{final}. When dT_{final} equals the ΔT observed in the well, the corresponding time is assumed to be the time of cooling. Applying the aforementioned technique, the cooling time is found to be approximately 60 hours. It should be emphasized that this value is only a preliminary approximation that is based on a number of assumptions; however, as it turns out, this parameter does not have a significant impact in the estimation of S_{Hmax} (Brudy and Zoback, 1999).

Estimation of S_{Hmax} in Well 38C-9

With all the input parameters defined, (6) can be employed to estimate S_{Hmax}. The length of the drilling-induced fracture, L, and S_{Hmax} are unknowns. Also there is uncertainty associated with the time of cooling. Thus, S_{Hmax} vs. fracture length graphs are generated for various cooling times (Figure 8). The curves rapidly drop to a minimum value and then increase monotonically. The minimum value represents the stress level below which the fracture cannot propagate and thus represents a *lower bound* for S_{Hmax}. For a larger S_{Hmax} value, the fracture would have propagated an additional increment away from the wellbore. The implication of choosing the minima of the curves for S_{Hmax} is there is no further fracture extension. The fact no fluid loss or mud circulation problems were noted at this depth from well logs support this hypothesis. The implication then is a stationary fracture or a fracture that did not propagate far into the formation. The minimum values for different cooling times are listed in Table 2. All the values in Table 2 correspond to an initial fracture length of 0.09*r* or 0.55 inches (1.39 cm).

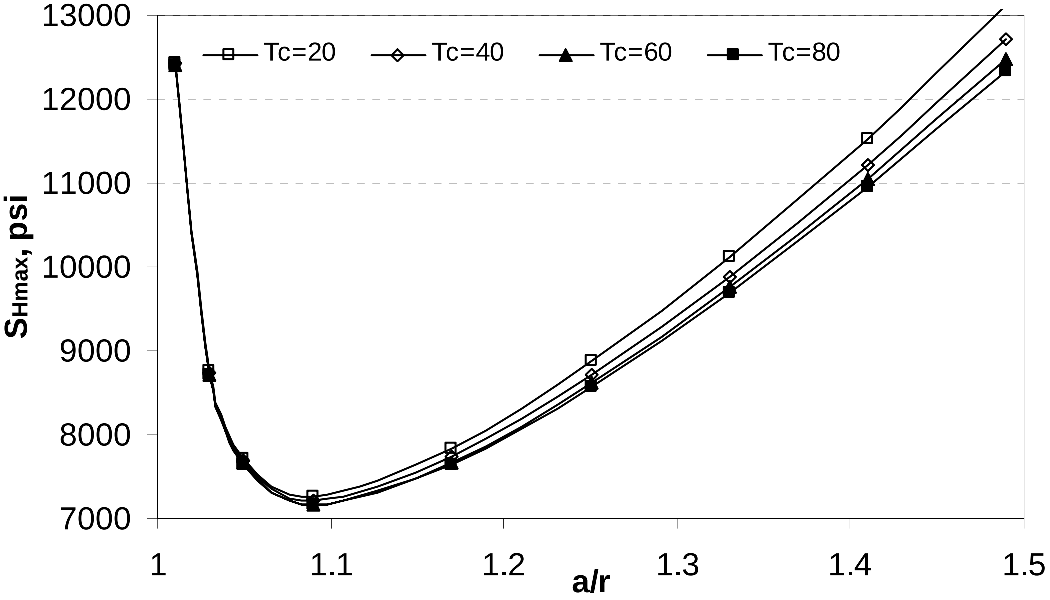

Figure 8. S_{Hmax} vs. Normalized Fracture Length for Different T_c Values (in Hours). The Minimum Values of the Curves Correspond to a *Lower Bound* Estimate of S_{Hmax}

In calculating the curves in Figure 8 it was assumed $p_{frac} = p_w$, which is an upper bound for p_{frac}. The lower bound for p_{frac} should also be considered, which is p_o. Examination of (6) shows the p_{frac} lower bound will provide an upper value for the S_{Hmax} *lower bound*. The p_{frac} upper bound will provide a lower value for the S_{Hmax} *lower bound*. These values are reported in Table 2.

Table 2. Minimum Values from S_{Hmax} Curves in Figure 8, and Mean and Standard Deviation of S_{Hmax} Estimates.

T_c, hr	S_{Hmax} (psi), $p_o = p_{frac}$	S_{Hmax} (psi), $p_w = p_{frac}$
20	9613	7267
40	9554	7209
60	9523	7178
80	9503	7157
Mean S_{Hmax}	**9548**	**7203**
St. Dev. of S_{Hmax}	**± 48**	**± 48**

This methodology for the drilling induced fracture at 7650 ft was repeated for all of the drilling induced tensile fractures reported in well 38C-9 when data were available. The results are shown in Figure 9. The lines of best fit show reasonable accuracy. Note that Figure 9 predicts non-zero horizontal stresses at the surface, which would not be unlikely in an active area of faulting such as Coso.

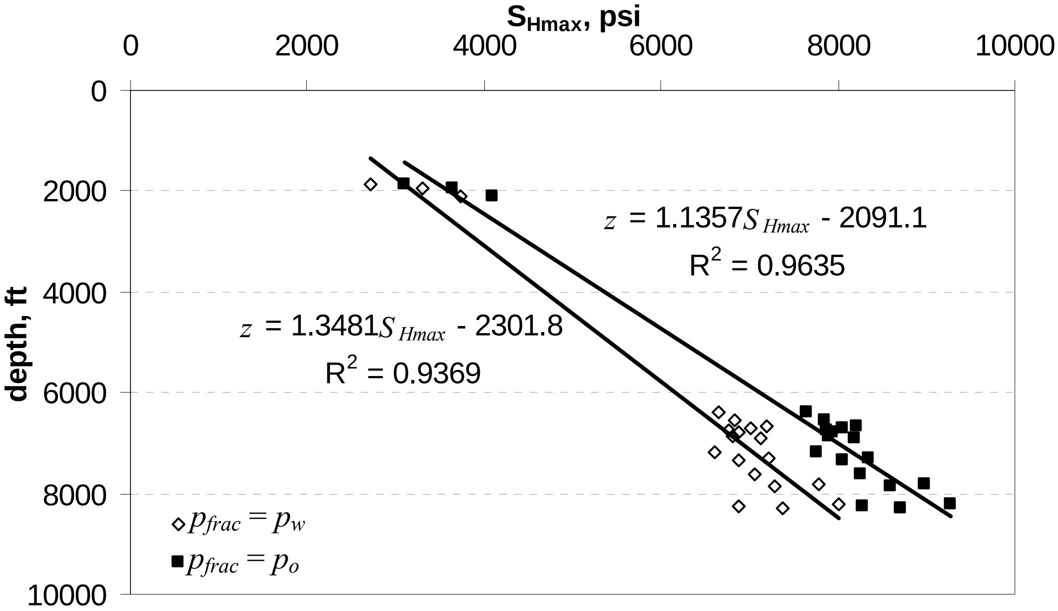

Figure 9. S_{Hmax} Estimate from Drilling-Induced Tensile Fractures and the Resulting Lines of Best Fit.

Comparison with other S_{Hmax} Estimates

A higher estimate of S_{Hmax} has been reported in Hickman & Sheridan (2004), ranging from roughly 1.33 psi/ft to 2.17 psi/ft. It is worthwhile to consider these values of S_{Hmax} and study their effect on the propagation behavior and length of the induced fractures. For this purpose, the stress intensity function (K_I) is calculated for each estimate of the S_{Hmax} at the depth of 7650 ft. It is assumed $p_{frac} = p_w$ allowing for K_I to be plotted versus the normalized fracture length (see Figure 10). For the K_I values above the K_{IC} (dashed line), the conditions are right for further fracture extension. The lower estimate (“inter”) from Sheridan and Hickman (2004) shows no fracture propagation while the upper estimate (“upper”) shows fracture propagation to 1.5*r*. If thermal stresses are included, the fracture would propagate from 1.37*r*-2.15*r* (2.27-7.04 inches) for the lower and upper value of the *upper bound* estimate, respectively. In considering our estimate it is found the lower value shows no fracture extension, while the upper value shows fracture propagation up to 1.3*r* (1.84 inches). If $p_{frac} = p_o$ is assumed, fracture extension to the end of the temperature perturbation (2.38*r*) is predicted except for the *lower bound* lower value. This result supports the use of the lower value of the *lower bound*.

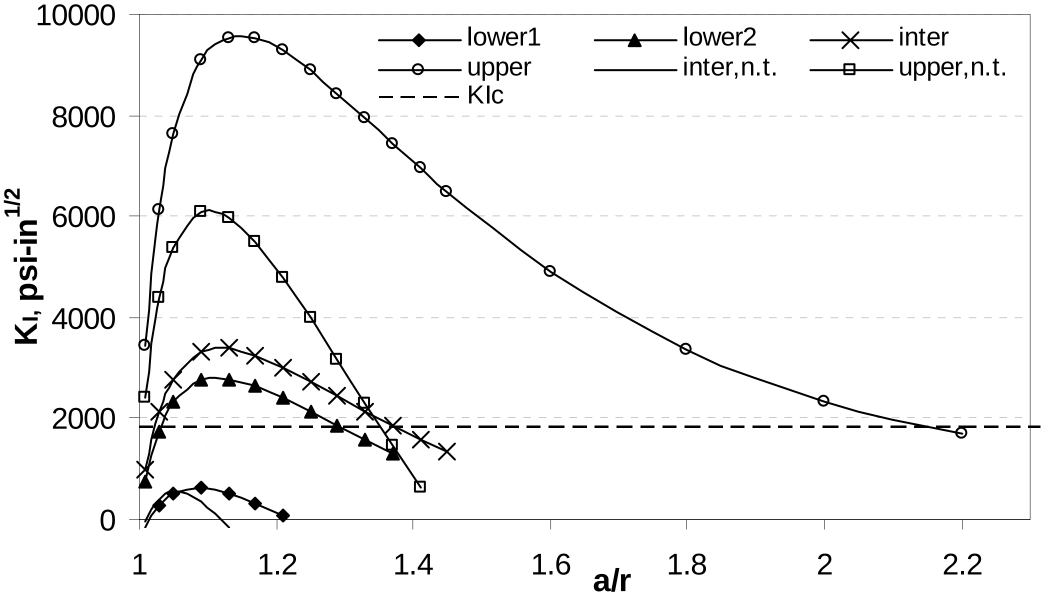

Figure 10: Stress Intensity Function for Various S_{Hmax} Estimates. Values above the Dashed Line (K_{IC}) Indicate Fracture Propagation (n.t. Implies no Thermal Stresses Used).

Stress Tensor Summary

The estimated stress tensor is summarized in Table 3. The S_{Hmax} estimates are given as:

$$S_{H\max} = 0.742z + 1707.4 \tag{17}$$

for z in ft, and S_{Hmax} in psi, and for S_{Hmax} in MPa and z in m:

$$S_{H\max} = 0.01678z + 11.78 \tag{18}$$

Table 3. Estimated In-Situ Stress Tensor for East Flank of Coso Geothermal Reservoir.

	Direction and depth	**Magnitude**	**Magnitude (in SI units)**	**Comments**
S_v	⊥ Earth surface	1.14 psi/ft	0.0258 Mpa/m	density logs
S_{hmin}	88° ±3° (5811-9408 ft or 1792-3867 m)	0.66 psi/ft	0.0149 Mpa/m	HF test
S_{Hmax}	172°±7° (690-3726 ft or 210-1136 m) 14°±16° (5811-9408 ft or 1792-3867 m)	Eqn. (17)	Eqn. (18)	frac mech. analysis
p_o	not applicable	0.33 psi/ft	0.00747 Mpa/m	well data

CHAPTER III

FRACTURE CHARACTERIZATION

State of Fractures and Fractured Rock Mass

To determine the response of the fractures in the vicinity of well 38C-9 under the current stress state; the recorded fracture strike, dip, and dip direction interpreted by a formation micro-scanner (FMS) are examined. Using FMS data from well 38C-9, Sheridan and Hickman (2004) have identified *fractures with significant aperture* within the total fracture population. Because of their increased aperture, these fractures can control permeability around well 38C-9.

There were two intervals of well 38C-9 recorded by the FMS: 690-3726 ft (210-1136 m), and 5881-9408 ft (1792-3867 m). The complete results of the FMS data are reported in Appendix A of Rose et al. (2003). The first interval has two distinct fracture trends. The first trend is in the interval 210-1136 m with dip directions in the NW and SE directions. The second subgroup is present in the interval of 709-1136 m and has dip directions of N and S (Sheridan and Hickman, 2004); the overall trend of the dips range from 30º to 70º. The lower interval has dip directions trending in the W-WNW and E-ENE; the dips increase with most of the fractures having dip angles of 60º-80º (Sheridan and Hickman, 2004). The differences observed in the upper portions of the fracture network and the lower portions of the fracture network indicate these fracture sets may have resulted from different stress regimes.

In light of this, it is worthwhile to consider the type of joints that can be theoretically expected in different faulting/stress regimes. First, consider the normal faulting regime shown in Figure 11a. According to the normal faulting regime, fractures strike in the direction of S_{Hmax}, and dip in the directions of S_{hmin}; the dips are comparable to the critical orientation (β_{crit}) shown in Figure 10a. The expression for β_{crit} is derived in the next section. According to the strike-slip faulting regime shown in Figure 11b, the fractures will dip in the vertical direction and strikes and dip direction will generally bisect the S_{Hmax} and S_{hmin} direction.

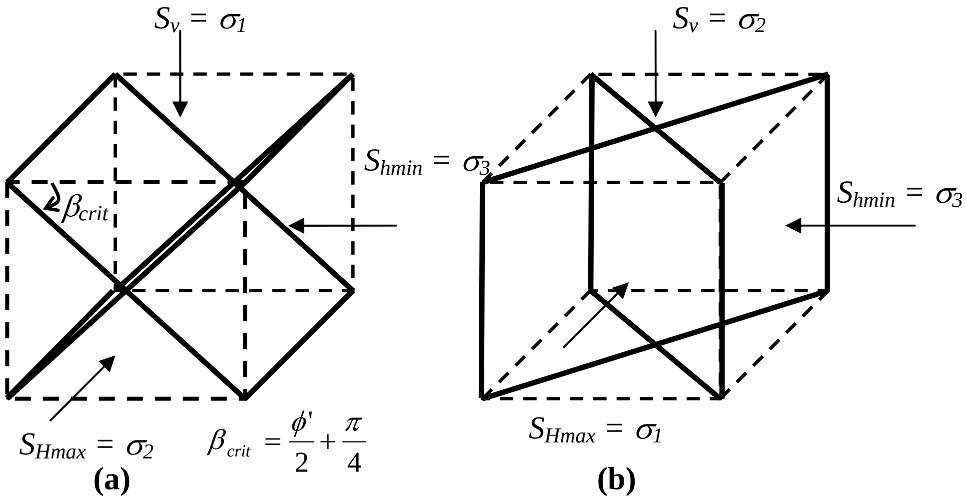

(a) **(b)**

Figure 11. (a) Normal Faulting Regime Joints, and (b) Strike-Slip Faulting Regime Joints.

Examining Table 3 and the characterization of the *fractures with significant aperture*, the stress regimes of certain intervals can be classified according to Figure 11. The most easily classified interval is 1792-3867 m in which the fractures show evidence of a normal faulting regime. Indeed, most of the fractures strike in the S_{Hmax} direction. Also of interest is that the fractures are dipping roughly at the predicted critical orientations for the intact rock (roughly 60º, Rose et al., 2004). In the top portion of the upper interval the fracture strike directions mirror that of a strike slip-faulting regime. If this is the case, the dips should be close to vertical, but the dips recorded were between 30º-70º. Even more surprising is the lower section of the upper interval where, in general, the fractures strike in the S_{hmin} direction, with a dip of 30º-70º. One explanation would be to consider the scenario when $\sigma_1 = S_v = S_{Hmax}$; this would possibly result in propagation of the fractures in the S_{hmin} direction because it would become, in a sense, σ_2. In considering the previous statement, the strikes of the *fractures with significant aperture* show evidence of a strike-slip faulting regime with transition to a normal faulting regime with increasing depth. The dips also suggest this situation is quite possible. Deviations from this trend occur at the top portion of the upper interval where vertical dips would be expected. This can be due to the fact that vertical joints are not always observed in logged vertical boreholes, because they would not be intersected.

Failure Criteria for Rock Fractures

Linear Failure Criterion

Slip along pre-existing discontinuities has been identified as mechanism for permeability enhancement in EGS. Therefore, it is of interest to consider slip of pre-existing joints in the east-flank of Coso. In doing so, we use data from well 38C-9 and investigate conditions that are conducive to joint slip. The *fractures with significant aperture* in the lower interval of well 38C-9 will be considered, because this is the depth where the injection has been proposed (approx. 7600-7700 ft or 2316-2347 m) (Sheridan and Hickman, 2004). In using a linear failure criterion it is assumed failure is independent of the intermediate principal stress, and occurs in the plane of maximum shear. Therefore, the S_v-S_{hmin} plane is assumed as the plane of failure. This interval can be modeled similarly to that seen in Figure 12.

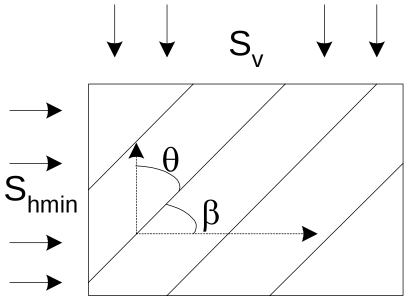

Figure 12. Idealized Model of *Fractures with Significant Aperture* in the Lower Interval of Well 38C-9.

To predict fracture slip, a failure criterion is needed. A linear failure criterion for the planes of weakness can be obtained by considering the normal and shear stresses acting on the plane of weakness:

$$\sigma_n = P_o + S_o \cos(2\beta) \tag{19}$$

$$\tau = S_o \sin(2\beta) \tag{20}$$

where $P_o = \frac{\sigma_1 + \sigma_3}{2}$ and $S_o = \frac{\sigma_1 - \sigma_3}{2}$ are the mean and deviatoric stress components respectively. Eqns. (19) and (20) are then substituted into a failure criterion for the joints, which will be defined as:

$$\tau_f = \sigma_n^{'} \tan\phi' \tag{21}$$

where τ_f is the shear stress at failure, $\sigma_n^{'}$ is the effective normal stress (σ_n- p_o) and ϕ' is the friction angle of the joint. Substitution of (19) and (20) into (21) yields (Jaeger and Cook, 1979; p. 106):

$$\sigma_1 - \sigma_3 = \frac{2\sigma_3 \tan\phi'}{(1 - \tan\phi' \cot\beta)\sin 2\beta} \tag{22}$$

ϕ' is not known but can be found from lab tests. Since this has not been accomplished yet, a range of typical ϕ' values from 35º-55º is assumed. Differentiating (22) with respect to β and setting it equal to zero yields (Jaeger and Cook, 1979; p. 107):

$$\begin{aligned} &\tan 2\beta_{crit} = -\cot\phi' \\ &or \\ &\phi' = 2\beta_{crit} - \frac{\pi}{2} \end{aligned} \tag{23}$$

Eqn. (23) represents the least stable joint orientation for a given friction angle (see Figure 10a). Applying (23) to Figure 12 shows β_{crit} equals 62.5º-72.5º, which agrees with the observed dips of 60º-80º. This implies the assumed values for the friction angle of the joints are reasonable.

Non-linear Failure Criterion

Much empirical evidence shows the failure envelope of rock is not linear, and tends to have parabolic or logarithmic behavior. To account for this an envelope developed by Barton et al. (1976, 1977, 1980) for jointed rock is chosen:

$$\tau_f = \sigma_n^{'} \tan\left[\phi_b + JRC \log_{10}\left(\frac{JCS}{\sigma_n^{'}}\right)\right] \tag{24}$$

where ϕ_b is the basic friction angle for a smooth surface, *JRC* is the joint roughness coefficient, and *JCS* is the joint wall compressive strength. In the absence of data a range of likely values is chosen. The *JRC* for granitic type rocks can be 5º (smooth and planar)-10º (smooth-undulating). Note when *JRC* = 0º (24) becomes (21). The *JCS* can have similar values to the uniaxial compressive strength (see for example Pine and Batchelor, 1984). The rock in the lower interval of well 38C-9 is hornblende-biotite-quartz diorite (HBQD), and has a uniaxial compressive strength of 193 MPa (Rose et al., 2004). From the *JRC* range chosen (5º-10º), the basic friction angle will be in the range 25º to 50º for continuity with the friction angles (35º-55º) chosen for the linear criterion. This empirical strength envelope takes into account the stress dependence the τ / σ'_n ratio has due to crushing and scaling effects on the joint (Pine and Batchelor, 1984). An example plot showing the deviations from linear are shown in Figure 13.

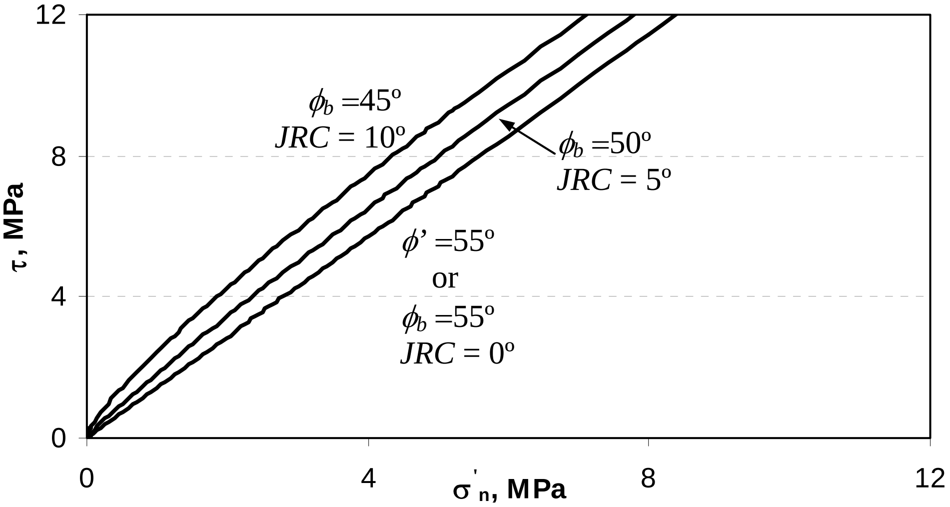

Figure 13. Failure Criteria for Slip of Joints.

Limiting Stress Conditions

Since the exact value of ϕ' is not known, it is of interest to look at the limiting value of the critical stress, *R*, for a range of possible friction angles. For the geometry of Figure 12, *R* is defined in Pine and Batchelor (1984); it also can be found by manipulation of (22):

$$R = \frac{\sigma_1'}{\sigma_3'} = \frac{1 + \tan\phi'\left(\sin 2\theta + \tan\phi' \cos 2\theta\right)^{-1}}{1 - \tan\phi'\left(\sin 2\theta + \tan\phi' \cos 2\theta\right)^{-1}} \tag{25}$$

The plots of *R* with respect to θ for different friction angles is shown in Figure 14, which shows that as the friction angle increases the limiting value *R* also increases. The $R_{1,3}$ value is also plotted, which is S'_v / S'_{hmin}. As shown in Figure 14, for ϕ' values less than

25º critically stressed joints can exist. The S'_{Hmax} / S'_{hmin} value, from (18), will vary with depth and is given as:

$$R_{2,3} = \frac{S'_{H\max}}{S'_{h\min}} = 1.246 + \frac{1576.97}{z} \qquad (26)$$

Eqn. (26) shows that the limiting stress ratio is hyperbolically related to the depth. The implication of this is that at very shallow depths all existing joints will be critically stressed, however as the depth is increased (26) approaches 1.246. Therefore, it can be concluded from Figure 14 that joints at great depths will not be critically stressed. The minima of each curve represent the least stable joint orientation which are 18º, 23º, 28º, and 33º for ϕ' = 55º, 45º, 35º, and 25º, respectively. All of these values are within the observed jointing network in the lower interval of well 38C-9.

Limiting Stress Gradient

To better understand the implication of (26) on the behavior of joints with respect to depth, it is of interest to plot limiting stress gradients with respect to the existing in-situ stress gradients given in Table 3. The limiting stress gradients represent *R* values as a function of depth for a given friction angle and its corresponding critical orientation, β_{crit}. Figure 15 shows two such limiting stress gradients along with the in-situ stress profiles. The ϕ' = 20º curve represents a critically stressed joint in the S_v-S_{hmin} plane, whereas the ϕ' = 35º curves represent a joint that is stable in the S_v-S_{hmin} plane. It is readily seen that

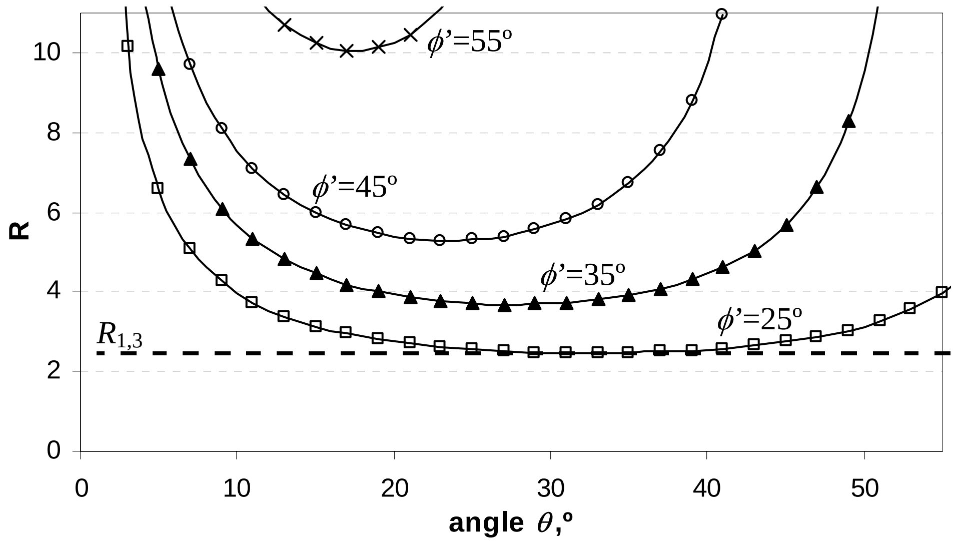

Figure 14. R Values for the Range of Friction Angles Chosen. $R_{1,3}$ Represents In-Situ Value.

joints with the ϕ’ = 20º and ϕ’ = 35º are critically stressed in the S_{Hmax}-S_{hmin} plane to a depth of 2010 m and 650 m, respectively. Figure 15 also shows that the S_v curve and S_{Hmax} curve intersect at 1306 m. Thus at depths above 1306 m, $\sigma_1 = S_{Hmax}$, and below 1306 m, $\sigma_1 = S_v$. There are two conclusions drawn from this. The first is that the in-situ stress is transitioning from a strike-slip type stress regime to a normal type stress regime. This supports the earlier characterization of the *fractures with significant aperture* population, in which the jointing network theoretically supported a strike-slip type stress regime transitioning to a normal type stress regime with increasing depth (see Figure 11). The second is that when considering injection above 1306 m, the S_{Hmax}-S_{hmin} plane is the failure plane whereas below this depth the S_v-S_{hmin} plane is the failure plane. Since the proposed injection depth is well below 1306 m, the S_v-S_{hmin} plane is the failure plane. It should be noted that S_{hmin} may not be zero at the surface, however, in the absence of data it is assumed zero at the surface.

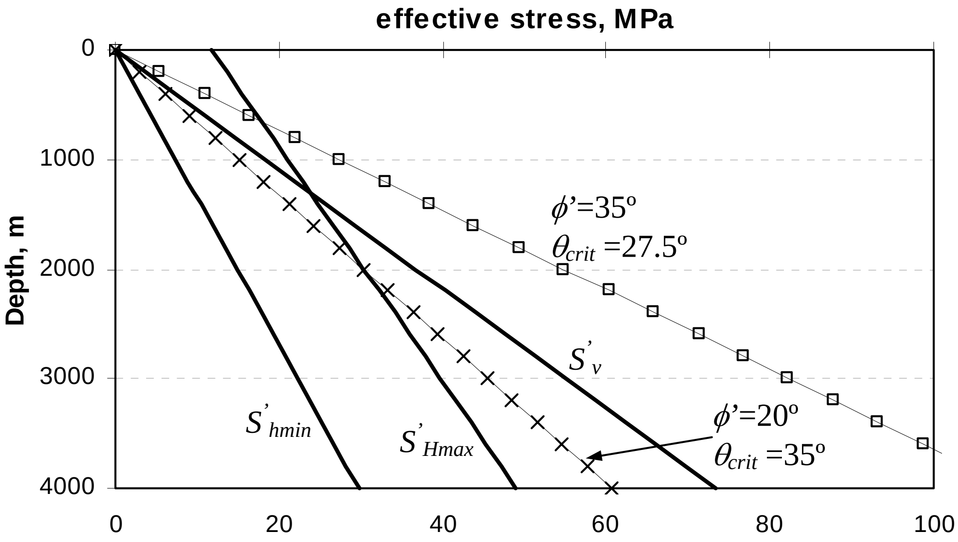

Figure 15. Measured Stress Gradients and Limiting Stress Gradients.

Critical Pore Pressure on Joints

Since joints at the injection depth of 2316 m appear not to be in a critical state unless ϕ' is less than 25°. It is of interest to determine the amount of pressure needed for critically stressing the joints and inducing slip. Upon stimulation of a reservoir, a unit increase of fluid pressure on a fracture will decrease the effective stress by a unit according to Terzaghi's definition of effective stress. The critical pore pressures to initiate slip for intact rock and for a joint are shown in Figure 16. The Mohr-Coulomb diagrams show these values to be different, because for intact rock failure will occur at some critical orientation. But, for a pre-existing joint, the failure is constrained to a given joint orientation.

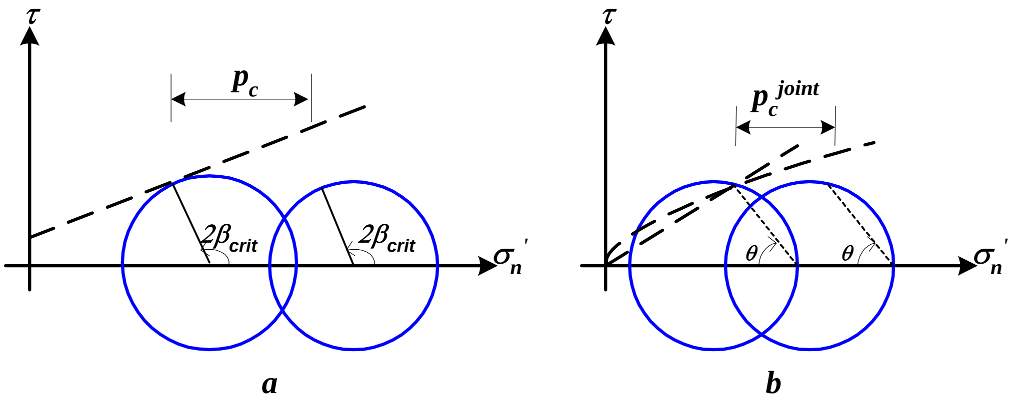

Figure 16. (a) Shows Critical Pore Pressure for Intact Rock, and (b) Shows Critical Pore Pressure for Joints (Non-Linear and Linear).

To investigate the additional pore pressure needed to activate the existing fracture network the following equation is applied (Goodman, 1980; p. 165):

$$p_c^{joint} = \sigma_3 + 2S_o\left[\sin^2(90-\beta) - \frac{\sin(90-\beta)\cos(90-\beta)}{\tan\phi'}\right]$$

(27)

A plot of (27) is shown in Figure 17 for various friction angles. All the curves decrease until a critical orientation is reached and then increase. The critical pore pressure (p_c^{joint}) and the additional pore pressure ($p_o^{+} = p_c^{joint} - p_o$) for the observed joint dip angles in the range of 60º-80º are reported in Table 4 for the linear failure criterion, and in Table 5 for the non-linear failure criterion. The values for Table 5 are calculated at the injection depth of 2316 m where p_o = 17.3 MPa. The non-linear criterion was iteratively solved, because σ_n' cannot be isolated in (24). This was accomplished by first expressing (20) in terms of σ_n'; then calculating σ_n' and τ using (19) for a given θ. Next, the pore pressure was increased/decreased until τ and σ_n' intersected (24) at a single point. This process was then repeated for a different θ. Inspection of Table 4 and Table 5 shows their differences are negligible except for when ϕ_b = 45° and *JRC* = 10° (see Figure 12), therefore, this non-linear criterion will only be considered. The critical pore pressure for this case is also plotted in Figure 17.

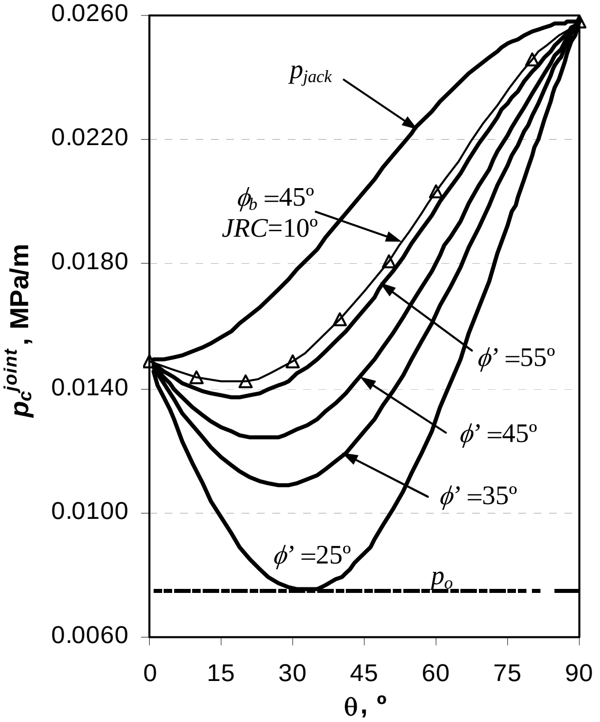

Figure 17. Critical Pore Pressures Needed for Slip and Jacking on Various Joint Orientations and Friction Angles; the Non-Linear Envelope Corresponds to the Depth 2316 m.

Table 4. Critical Pore Pressure (p_c^{joint}) and Additional Pore Pressure, in MPa/m Needed to Activate Joints for Different ϕ' and β Values.

	β = 60°		**β = 70°**		**β = 80°**	
ϕ'	**p_c^{joint}**	**p_o^+**	**p_c^{joint}**	**p_o^+**	**p_c^{joint}**	**p_o^+**
35°	0.0109	0.00347	0.0112	0.00375	0.0126	0.00514
45°	0.0129	0.00548	0.0127	0.00525	0.0134	0.00594
55°	0.0144	0.00689	0.0138	0.00629	0.0140	0.00649

Table 5. Critical Pore Pressure and Additional Pore Pressure (in MPa) Needed to Initiate of Slip on Three Different Joint Orientations for Various ϕ_b and *JRC* Values.

		β = 60º		**β = 70º**		**β = 80º**	
ϕ_b	***JRC***	**p_c^{joint}**	**p_o^{+}**	**p_c^{joint}**	**p_o^{+}**	**p_c^{joint}**	**p_o^{+}**
25º	10º	26.89	9.59	27.67	10.37	26.89	9.59
30º	5º	25.48	8.18	26.37	9.07	29.67	12.37
35º	10º	30.94	13.64	30.51	13.21	31.97	14.67
40º	5º	30.38	13.08	29.90	12.60	31.44	14.14
45º	10º	34.46	17.16	33.03	15.73	33.23	15.93
50º	5º	33.76	16.46	32.37	15.07	32.71	15.41

The hydraulic jacking pressure (p_{jack}) is also plotted in Figure 17. Hydraulic jacking occurs when the normal stress on the joint equals zero. By setting (19) equal to zero the following expression is arrived at:

$$p_{jack} = P_o - S_o \cos(2\theta) \tag{28}$$

Eqn. (28) shows when θ = 0º or 90º, $p_{jack} = p_c$. It is evident the joints orientated from θ =10º-30º (β = 60º-80º) are among the first to slip, and for shallower dipping orientations the required pore pressure increases vastly such that after a given orientation jacking can be initiated in near vertical joints first. The joint orientation at which this occurs can readily be found by setting (28) equal to (27) and solving for θ. When θ = 0 (p_{jack} minimum), the following relation can be derived:

$$\tan^2 \phi = \cot \theta \tag{29}$$

Application of (29) for ϕ' = 35º, 45º, 55º yields θ = 55º, 45º, and 35º, respectively. This occurs at θ = 30º for the non-linear curve which varies from the orientation of the linear model by 14%. This deviation shows that considerations of the non-linear envelope should not be ignored. In noting the similarity between Figure 14 and Figure 17, it follows that for a ϕ' = 25º, the curve is tangent to the ambient pore pressure line at θ = 34º.

Growth and Direction of Shearing

When non-horizontal joints slip, shear growth can occur upward or downward. This can be predicted by considering the difference in the pressure increase per unit depth required for slip above and below the injection point. If the pressure increment difference is positive, downward shear growth is expected as slip propagates downward where less pressure is required. This is a function of the variation of joint properties and in-situ stress with depth. Indeed, a change in shear growth can occur at a critical depth if the stress gradient is non-linear. The downward or upward shear growth can therefore, be expressed as (Pine and Batchelor, 1984):

$$\frac{dp_o^+}{dz} = \frac{1}{2}\left(\frac{d\sigma_1^{'}}{dz} + \frac{d\sigma_3^{'}}{dz}\right) - \frac{\sin 2\theta + \tan\phi' \cos 2\theta}{2\tan\phi'}\left(\frac{d\sigma_1^{'}}{dz} - \frac{d\sigma_3^{'}}{dz}\right) \tag{30}$$

where z is depth. Upward growth is predicted for positive values of (30) and negative values predict downward growth. The derivatives on the right hand side of (30) are the values given in Table 1 minus the pore pressure gradient. Solving (30) for the ratio ($d\sigma_1^{'}/d\sigma_3^{'}$), it is found that upward growth, (30) is positive, is predicted when (Pine and Batchelor, 1984):

$$\frac{d\sigma_1^{'}}{d\sigma_3^{'}} < R \tag{31}$$

Eqn. (31) and Figure 14 can therefore predict shear growth. In general, for critically stressed fractures downward shear growth is expected, and for non-critically stressed fractures upward growth is expected. Therefore, upward shear growth can be expected at the injection depth of 2316 m for $\phi' > 25^{o}$. However, at depths above 1306 m ($S_{Hmax} = \sigma_1$), Eqn. (31) predicts downward growth until the critical depth. For example, the $\phi' = 35^{o}$ curve in Figure 15 predicts downward growth till 650 m.

The direction of shearing can also be addressed, and as shown in Pine and Batchelor (1984) negative or positive values of the following equation imply the direction of shearing:

$$\frac{d\{\tau_f - \tau(z)\}}{dz} = \frac{dp_o^+}{dz}\tan\phi' \qquad (32)$$

Eqn. (32) is the derivative of the failure criterion (21) with respect to depth, and therefore describes the rate of change or direction of shearing (failure). In a critically stressed area where $\tau > \tau_f$, (32) predicts downward shearing, i.e., p_o^+ needed to induce slip decreases with depth. On the other hand, if the p_o^+ needed to induce slip increases with depth ($\tau < \tau_f$) upward shearing will occur. For the injection depth of 2316 m, ϕ' values greater than 25^{o} result in upward shearing, and for ϕ' values less than 25^{o} downward shearing can occur on critically oriented joints. Again note that at depths above 1306 m, the critical depth represents a change in the direction of shearing. The direction of growth and the direction of shearing can therefore be extrapolated from Figure 14 thus showing the importance of the limiting stress ratio R in the prediction of not only failure, but also the direction of growth and shearing.

CHAPTER IV

MATHEMATICAL MODEL FOR PREDICTING THE EFFECTS OF WATER INJECTION INTO A FRACTURE

In this chapter the general equations governing fluid flow and heat transport in a deformable fracture are developed. Special solutions are also presented for simple cases. These solutions will be used in subsequent chapters under various conditions to investigate the response of the fracture aperture and fluid pressure to injection. Three problem geometries will be considered:

I. Injection/extraction from a line fracture

II. Injection into infinite radial fracture

III. Injection into a joint

In developing these models the following assumptions are applicable:

(i) The reservoir is infinite in extent and behaves as linearly elastic, isotropic, homogenous rock.

(ii) Heat conduction and water leak-off between the rock mass and fracture occur only in the direction perpendicular to the fracture.

(iii) The aperture of the fracture is considerably smaller than its length.

(iv) All thermal properties of the fluid and rock are constant.

(v) Fluid flow is steady state and laminar.

(vi) Rock displacement resulting from thermoelastic and poroelastic loads is zero parallel to the fracture.

(vii) Heat storage and dispersion in the fracture will be ignored (Cheng et al, 2001).

Other assumptions specific to the geometry will be stated in the mathematic formulation. References to the above assumptions will be denoted by the corresponding Roman numeral in the text.

Injection/Extraction from a Line Fracture

Mathematic Model

The geometry of interest is shown in Figure 18. The reservoir is assumed to be of constant height and infinite horizontal extent. It is insulated at the top and the bottom. The fracture is a vertical plane penetrating the entire height of the reservoir. Hence, the solution geometry is two-dimensional, as shown in Figure 18b. Actually, this is a quasi-two-dimensional heat conduction model (Bodvarsson, 1969; Gringarten, 1975; Lowell, 1976). This is similar to the plane strain approximation that will be used when considering the solid mechanics aspect of the problem. For the injection/extraction problem, it is assumed *the injection pressure is below or near the minimum in-situ stress so that fluid/solid coupling can be neglected.*

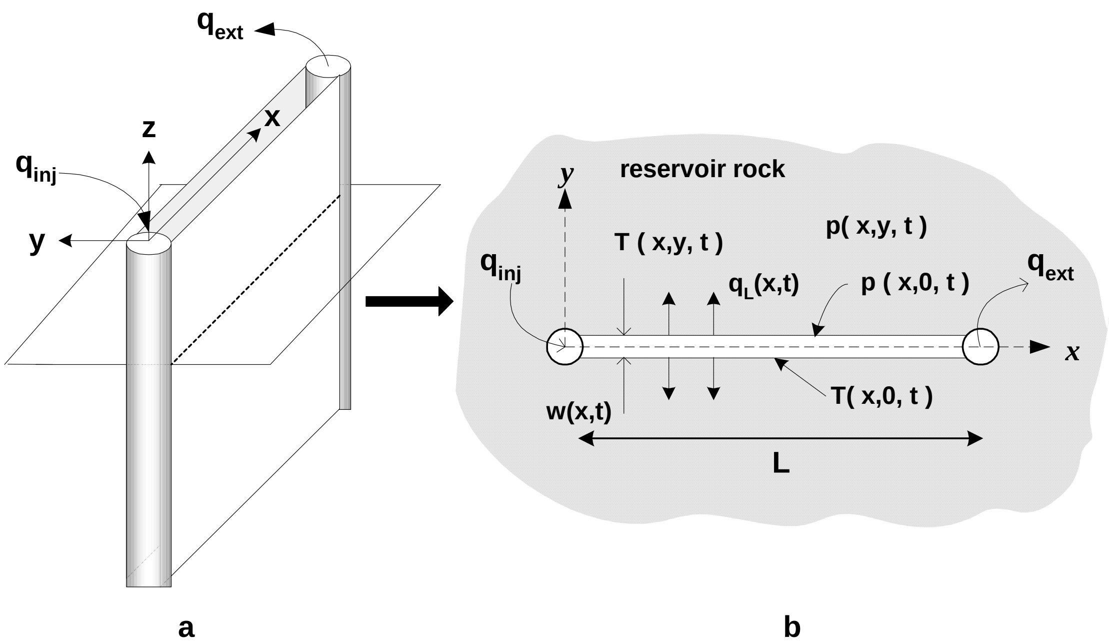

Figure 18. Model for Injection/Extraction from a Line Fracture (a) Idealized View of Heat Extraction from an EGS, (b) Solution Domain of the Mathematical Problem.

Fluid Flow in Line Fracture

We begin by considering Figure 19 which shows the mass balance of a representative elementary volume (REV) of a line fracture. The REV utilizes assumption (v). By conservation of mass, the continuity equation becomes:

$$v(x,t)w(x,t) - v(x,t)w(x,t) - \frac{\partial\left[w(x,t)v(x,t)\right]}{\partial x} - 2q_L(x,t) = 0 \tag{33}$$

where $v(x,t)$ is the average fluid velocity, $w(x,t)$ is the fracture aperture, $q_L(x,t)$ is the leak-off velocity. The discharge per unit height of fracture is given as:

$$q(x,t) = w(x,t)v(x,t) \tag{34}$$

Eqn. (33) and (34) can be combined to yield the fluid continuity equation:

$$\frac{\partial q(x,t)}{\partial x} + 2q_L(x,t) = 0 \tag{35}$$

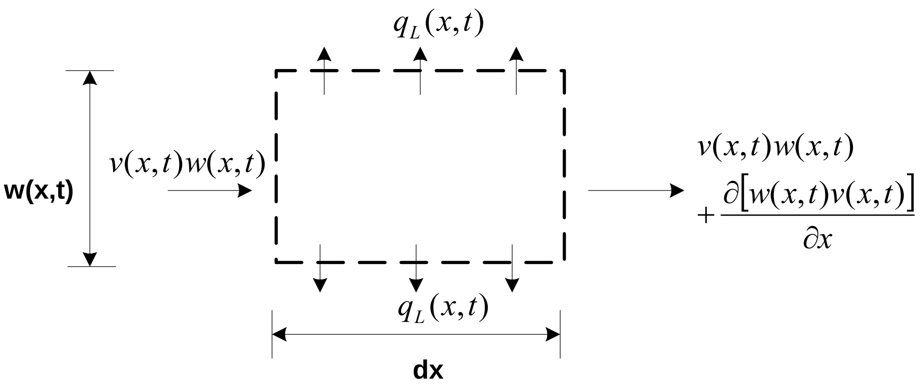

Figure 19. REV of Mass Balance in Line Fracture.

The second equation needed to describe fluid flow is the momentum equation, which relates the velocity to the pressure gradient. By assumption (iii) and (v) the momentum equation is:

$$\frac{\partial p(x,0,t)}{\partial x} = -\frac{12\mu_f}{w^3(x,t)} q(x,t) \tag{36}$$

where $p(x,0,t)$ is the pressure on the fracture surface, and μ_f is the dynamic fluid viscosity. Eqn. (36) is known as the cubic law and is derived in Appendix A. In reality viscosity is a function of pressure and temperature; however these effects will be ignored.

Fluid Flow in Reservoir Rock

In this section, the coupling effect between the flow in the reservoir rock and elastic deformation is assumed small and negligible. Utilizing this assumption and Figure 20, the pore pressure in the rock is governed by the diffusion equation:

$$\nabla^2 p(x,y,t) = \frac{1}{c_D}\frac{\partial p(x,y,t)}{\partial t} \tag{37}$$

where c_D is the consolidation coefficient, and $\nabla^2 = \frac{\partial^2}{\partial x^2} + \frac{\partial^2}{\partial y^2}$ is the Laplacian operator.

Utilizing assumption (ii) reduces Eqn. (37):

$$\frac{\partial^2 p(x,y,t)}{\partial y^2} = \frac{1}{c_D}\frac{\partial p(x,y,t)}{\partial t} \tag{38}$$

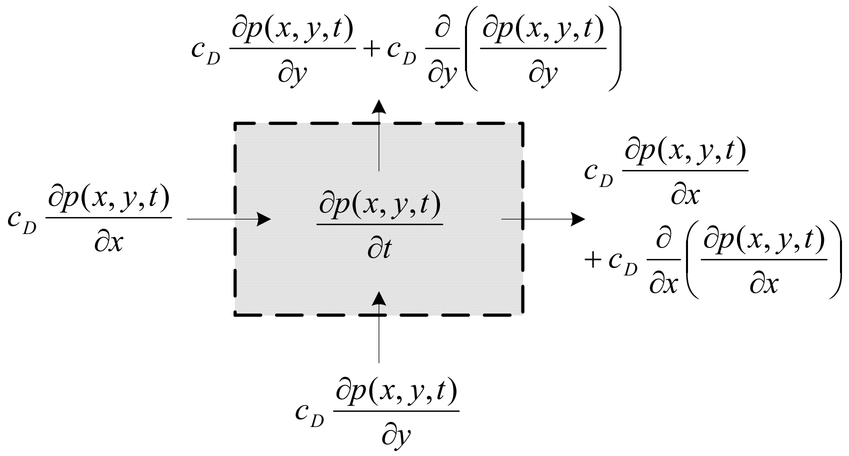

Figure 20. REV of Mass Balance in Reservoir Rock.

The boundary and initial conditions for the system (fracture and reservoir) are:

$$p^*(x,y,0) = 0 \tag{39}$$

$$p^*(L,0,t) = 0 \tag{40}$$

where $p^* \equiv p(x,y,t) - p(L,0,t)$ is the pore pressure changed by injection. As will be shown, Eqns. (39) and (40) can be applied to the diffusion equation (38) and the flow equation (36) to form the solution system; Eqn. (36) is solved first and the result used in (38).

Heat Transport in Line Fracture

Considering the heat balance over a fracture segment as shown in Figure 21, and neglecting the heat storage and dispersion in the fracture (assumption vii) yields the heat transport equation:

$$
\begin{aligned}
&-\rho_f c_f \frac{\partial q(x,t)T(x,y,t)}{\partial x} + 2K_r \left.\frac{\partial T(x,y,t)}{\partial y}\right|_{y=0} \\
&-2\rho_f c_f q_L(x,t)T(x,0,t) = 0
\end{aligned}
\tag{41}
$$

where ρ_f is the fluid density, c_f is the specific heat of the fluid, and K_r is the rock thermal conductivity. Substituting the fluid continuity equation (35) into (41) results in the following for the heat transport equation:

$$
\frac{\partial T(x,0,t)}{\partial x} = \frac{2K_r}{\rho_f c_f q(x,t)} \left.\frac{\partial T(x,y,t)}{\partial y}\right|_{y=0}
\tag{42}
$$

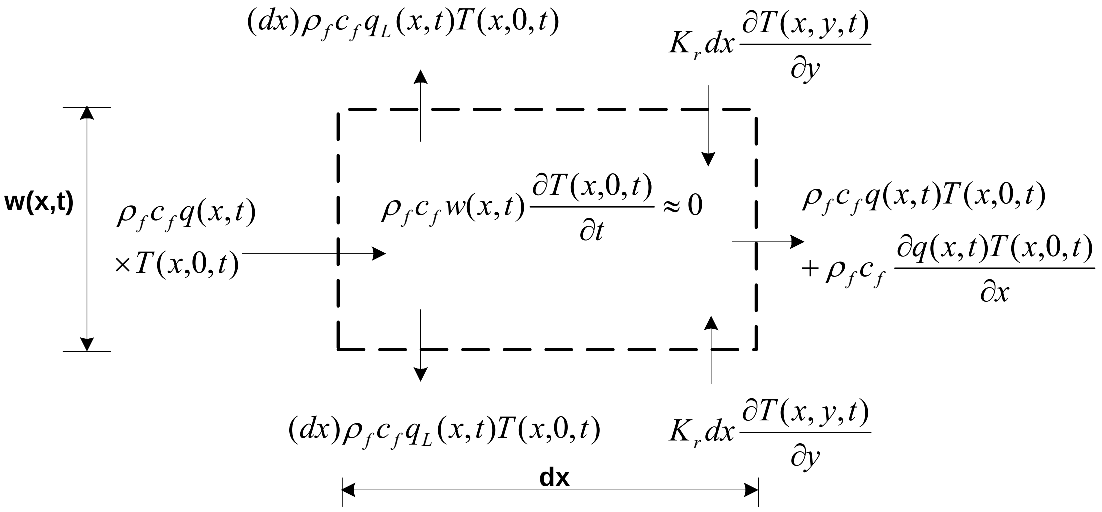

Figure 21. REV of Heat Balance in Line Fracture.

Heat Transport in Reservoir Rock

The REV of heat transport in the rock is shown in Figure 22. Applying the conservation of energy and assumption (ii) results in the heat conduction equation in the reservoir rock:

$$
\frac{\partial^2 T(x,y,t)}{\partial y^2} = \frac{\rho_r c_r}{K_r} \frac{\partial T(x,y,t)}{\partial t}
\tag{43}
$$

where ρ_r is the rock density and c_r is the specific heat of the rock. Combining (43) with the fluid mass balance (35) gives:

$$\frac{K_r}{\rho_r c_r}\frac{\partial^2 T(x,y,t)}{\partial y^2} - \frac{\partial T(x,y,t)}{\partial t} - q_L(x,t)\frac{\partial T(x,y,t)}{\partial y} = 0 \tag{44}$$

The initial and boundary conditions of the system are:

$$T(x,y,0) = T_{ro} \tag{45}$$

$$T(0,0,t) = T_{fo} \tag{46}$$

where T_{ro} is the initial rock temperature and T_{fo} is the prescribed temperature of the fluid at the injection point. As will be shown, Eqns. (45) and (46) can be applied to heat transport equations (44) and (42) to form the solution system; Eqn. (44) is solved first and the result used in (42).

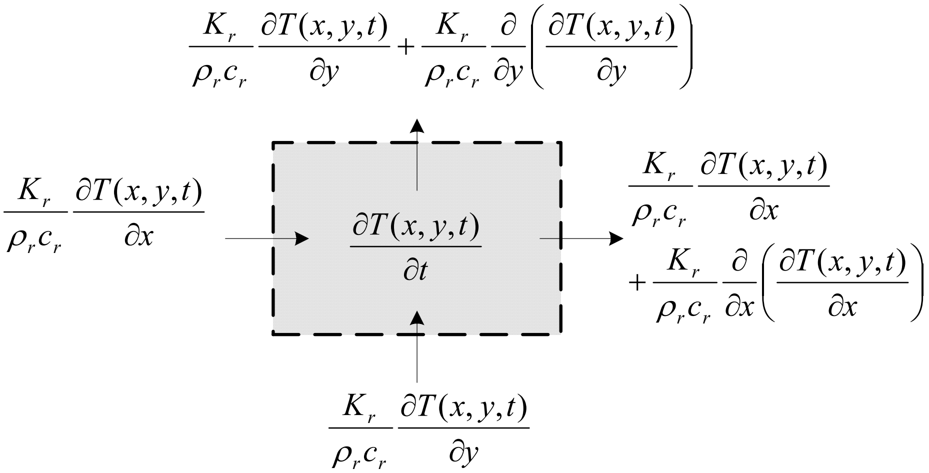

Figure 22. REV of Heat Balance in Reservoir Rock.

The equations derived above allow for calculating the temperature and pressure in the fracture and the reservoir rock. These temperature and pressure fields will result in body forces acting on the fracture and the rock. These induced body forces, by equilibrium conditions will induce displacements on the system. These displacements as they relate to the fracture width, and resulting pressure distribution in the fracture are addressed in the next section.

Fracture Aperture Changes from Thermoelastic and Poroelastic Effects

Elastic deformation of the fracture aperture can occur due to pressurization of the fracture. For the time being, this effect is ignored to focus on the deformation associated with heat extraction and fluid diffusion into or out of the rock. Fluid diffusion into the rock will cause the rock to dilate resulting in a reduction of the fracture aperture. Thermoelastic deformation can occur as a result of temperature differences between the fluid and the rock. Cold water injection into hot rock will cause the rock to contract thus increasing the fracture aperture. The pressure and temperature effects are related to deformation by a Navier type equation (McTigue, 1986; Palciauskas and Domenico, 1982):

$$G\nabla^2\vec{\mathbf{u}}(x,y,t)+\frac{G}{1-2v}\nabla\left[\nabla\cdot\vec{\mathbf{u}}(x,y,t)\right]=3K\alpha_T\nabla T(x,y,t)+\alpha\nabla p(x,y,t) \tag{47}$$

where G is the shear modulus, $\vec{\mathbf{u}}(x,y,t)$ is the displacement vector, K is the drained bulk modulus, α_T is the linear expansion coefficient, α is the Biot's effective stress coefficient, $\nabla\cdot=\frac{\partial\vec{\mathbf{u}}_{\mathbf{x}}}{\partial x}+\frac{\partial\vec{\mathbf{u}}_y}{\partial y}$ is the divergence operator, and $\nabla=\frac{\partial}{\partial x}+\frac{\partial}{\partial y}$ is the gradient operator. A complete derivation of (47) can be found in Appendix B. Once the pressure and temperature is known, the induced width changes can be found once the displacement is found by:

$$w(x,t)=2\vec{\mathbf{u}}(x,0,t) \tag{48}$$

Simplified plane strain model. In order to investigate the influence of poroelastic and thermoelastic processes on the fracture geometry, a plane strain model can be used to reduce the problem complexity (e.g., Ghassemi and Cheng, 2005). Utilizing assumption (vi), Eqn. (47) becomes:

$$\frac{\partial^2 u_y(x,y,t)}{\partial y^2} = \chi \frac{\partial T(x,y,t)}{\partial y} + \frac{\eta}{G}\frac{\partial p(x,y,t)}{\partial y} \tag{49}$$

where $\chi = \frac{\alpha_T(1+v)}{1-v}$. Eqn. (49) is integrated from y to ∞ utilizing the assumption that u_y = 0 at ∞:

$$-\frac{\partial u_y(x,y,t)}{\partial y} = \chi\left[T(x,y,t) - T(x,\infty,t)\right] + \frac{\eta}{G}\left[p(x,y,t) - p(x,\infty,t)\right] \tag{50}$$

At this point it is noted (50) is the expression for strain (e_{yy}), which is also assumed zero at ∞. Eqn. (50) can be integrated again from y to ∞ yielding:

$$-u_y(x,y,t) = \chi\int_0^\infty \Delta T(x,y,t)dy + \frac{\eta}{G}\int_0^\infty \Delta p(x,y,t)dy \tag{51}$$

where:

$$T(x,y,t) - T(x,\infty,t) = \Delta T(x,y,t) \tag{52}$$

$$p(x,y,t) - p(x,\infty,t) = \Delta p(x,y,t) \tag{53}$$

Differentiating (51) with respect to time yields:

$$-\frac{\partial u_y(x,y,t)}{\partial t} = \chi\int_0^\infty \frac{\partial \Delta T(x,y,t)}{\partial t}dy + \frac{\eta}{G}\int_0^\infty \frac{\partial \Delta p(x,y,t)}{\partial t}dy \tag{54}$$

Assuming one dimensional heat conduction and fluid diffusion, solutions of (38) and (44) can be substituted into (54) to obtain a solution. But, first performing the integration and applying (48) results in:

$$\frac{\partial w(x,t)}{\partial t} = \frac{2\chi K_r}{\rho_r c_r} \left. \frac{\partial \Delta T(x,y,t)}{\partial y} \right|_{y=0} - 2\chi q_L(x,t)\Delta T(x,0,t) + \frac{2\eta c_D}{G} \left. \frac{\partial \Delta p(x,y,t)}{\partial y} \right|_{y=0} \tag{55}$$

Eqn. (55) can be integrated when the temperature and pressure solutions are known, to calculate the variation of fracture width. The initial condition required to complete the solution system is:

$$w(x,0) = w_o \tag{56}$$

where w_o is the initial fracture aperture.

Constant Leak-Off Solution

Poroelastic Effects

For constant leak-off, q_{Lo}, and constant injection rate, q_o, the flow equation (35) becomes:

$$q(x) = q_o - 2q_{Lo}x \tag{57}$$

with $q_{Lo} = \frac{mq_o}{2L}$ where a fluid loss coefficient, *m*, can be expressed as the ratio between the extraction and injection rate (Cheng and Ghassemi, 2001). When $m = 0$ the $q_o = q_{ext}$, and when $m = 1$, $q_{ext} = 0$. Substituting (57) into (36) and applying the boundary condition in (40) gives:

$$p^*(x,0,t) = K_1^d x^2 - K_2^d x + K_2^d L - K_1^d L^2 \tag{58}$$

where $K_1^d = \frac{12\mu_f q_{Lo}}{w_o^3}$ and $K_2^d = \frac{12\mu_f q_o}{w_o^3}$. To determine the pressure in the reservoir, the Laplace transform is applied to the diffusion equation (38) resulting in:

$$\frac{\partial^2 \widetilde{p}(x,y,s)}{\partial y^2} = \frac{s}{c_D}\partial\widetilde{p}(x,y,s) \tag{59}$$

where *s* is the Laplace transform parameter. The solution to (59), applying the inherent boundary condition of a bounded solution, is:

$$\widetilde{p}(x,y,s) = \widetilde{p}(x,0,s)\exp\left(-y\sqrt{\frac{s}{c_D}}\right) \tag{60}$$

Inverting (60) to the time domain results in:

$$p^*(x,y,t) = p^*(x,0,t)erfc\left(\frac{y}{2\sqrt{c_D t}}\right) \tag{61}$$

and applying (58) yields:

$$p^*(x,y,t) = \left(K_1^d x^2 - K_2^d x + K_2^d L - K_1^d L^2\right)erfc\left(\frac{y}{2\sqrt{c_D t}}\right) \tag{62}$$

Ignoring the temperature effects for the time being; substitution of (62) into (55) will give the following simple integral equation to solve:

$$w_p(x,t) = \frac{-2\eta\sqrt{c_D}\,\Delta p^*_{poro}(x,0,t)}{G\sqrt{\pi}}\int\frac{1}{\sqrt{t}}dt \tag{63}$$

where $\Delta p^*_{poro}(x,0,t)$ is the pressure that induces poroelastic width changes, and the *p* subscript implies poroelastic width changes. Completing the integration and applying (56) results in:

$$w_p(x,t) = \frac{-4\eta\sqrt{tc_D}\,\Delta p^*_{poro}(x,0,t)}{G\sqrt{\pi}} + w_o \tag{64}$$

One can now apply the assumption that no fluid is lost and the poroelastic stress effect is negligible. Therefore, when $q_{Lo} = 0$, Eqn. (64) becomes:

$$w_p(x,t) = w_o \tag{65}$$

In hydraulic fracturing literature leak-off is often considered in the mass balance without addressing the poroelastic stresses. This manner of considering leak-off (when $q_{Lo} \neq 0$: permeable without poroelasticity) results in a lower pressure in the fracture. With poroelasticity the reduction in pressure is not as large. In this case, the amount of pressure reduction is found by subtracting the pressure change obtained for the impermeable case from the pressure change for the permeable poroelastic case. Utilizing (58) this is found to be:

$$\begin{aligned}\Delta p^*_{poro}(x,0,t) &= \left(K_2^d L - K_2^d x\right) - \left(K_1^d x^2 - K_2^d x + K_2^d L - K_1^d L^2\right) \\ &= K_1^d\left(L^2 - x^2\right)\end{aligned} \tag{66}$$

Eqn. (66) thus represents the change in pressure caused by leak-off and its associated poroelastic width changes. Substitution of (66) into (64) results in:

$$\omega_p(x,t) = -\frac{4\eta K_1^d\sqrt{tc_D}}{w_o G\sqrt{\pi}}\left(L^2 - x^2\right) + 1 \tag{67}$$

where $\omega_p(x,t) = w_p(x,t)/w_o$ is the normalized poroelastic net fracture width. The pressure distribution can be found by substituting (67) into momentum equation (36) to yield:

$$\frac{\partial p(x,0,t)}{\partial x} = \int \frac{12\mu_f(q_o - 2q_{Lo}x)}{\left[\dfrac{-4\eta K_1^d\sqrt{tc_D}}{G\sqrt{\pi}}\left(L^2 - x^2\right) + w_o\right]^3} dx \tag{68}$$

Eqn. (68) cannot readily be integrated, therefore numerical integration is applied using Simpson’s 3/8 rule is given as:

$$\int_0^L f(x)dx = \frac{L}{n}\sum_{i=1}^{n} w_i f(x_i)dx \tag{69}$$

where n is the total number of intervals (i), and w_i are weighting factors, which are:

$$w_i = \frac{3}{8}, \frac{7}{6}, \frac{23}{24}, 1, 1, \ldots, 1, 1, \frac{23}{24}, \frac{7}{6}, \frac{3}{8}; \quad for\ i = 1, \ldots, n \tag{70}$$

Thermoelastic Effects

For convenience, the dimensionless temperature deficit is introduced:

$$T_D(x, y, t) = \frac{T_{ro} - T(x, y, t)}{T_{ro} - T_{fo}} \tag{71}$$

Applying (71) to the heat transport equations (42) and (44) and applying the Laplace transform yields:

$$\rho_f c_f (q_o - 2q_{Lo}x) \frac{\partial \widetilde{T}_D(x, 0, s)}{\partial x} = 2K_r \left. \frac{\partial \widetilde{T}_D(x, y, s)}{\partial y} \right|_{y=0} \tag{72}$$

$$\frac{K_r}{\rho_r c_r} \frac{\partial^2 \widetilde{T}_D(x, y, s)}{\partial y^2} - q_{Lo} \frac{\partial \widetilde{T}_D(x, y, s)}{\partial y} - s\partial \widetilde{T}_D(x, y, s) = 0 \tag{73}$$

The boundary condition is also transformed into Laplace space:

$$\widetilde{T}_D(0, 0, s) = \frac{1}{s} \tag{74}$$

The solution of ordinary differential equation (ODE) (73) applying the inherent boundary condition of a bounded solution is (i.e. the temperature should be bounded and cannot go to infinity):

$$\widetilde{T}_D(x, y, s) = \widetilde{T}_D(x, 0, s) \exp\left(\frac{\rho_r c_r q_{Lo} \lambda}{2K_r} y \right) \tag{75}$$

where $\lambda = 1 - \sqrt{1 + \frac{4K_r s}{\rho_r c_r q_{Lo}^2}}$. Eqn. (75) is substituted into (72) resulting in:

$$\tilde{T}_D(x,0,s) = \frac{1}{s}\left(1 - \frac{2q_{Lo}}{q_o}x\right)^{-\frac{\rho_r c_r \lambda}{2\rho_f c_f}} \tag{76}$$

Eqn. (76) utilizes (74) and was first derived by Cheng and Ghassemi (2001) as a special case for their general solution of heat extraction with spatially variable leak-off.

In order to find the induced width change we first note the following relationship between (71) and (52):

$$-T^{\Delta} \times T_D(x,y,t) = \Delta T(x,y,t) \tag{77}$$

where $T^{\Delta} = T_{ro} - T_{fo}$. Applying (77) to (55) and transforming into the Laplace domain results in:

$$\tilde{\omega}_t(x,s) - \frac{1}{s} = \frac{-2T^{\Delta}\chi K_r}{s w_o \rho_r c_r} \left.\frac{\partial \tilde{T}_D(x,y,s)}{\partial y}\right|_{y=0} + \frac{2T^{\Delta}\chi q_{Lo}}{s w_o}\tilde{T}_D(x,0,s) \tag{78}$$

where the *t* subscript represents thermoelastic width changes. Substitution of (75) into (78) gives:

$$\tilde{\omega}_t(x,s) - \frac{1}{s} = \frac{-T^{\Delta}\chi q_{Lo}\lambda}{s w_o}\tilde{T}_D(x,0,s) + \frac{2T^{\Delta}\chi q_{Lo}}{s w_o}\tilde{T}_D(x,0,s) \tag{79}$$

Simplifying (79) and utilizing (76) for $\tilde{T}_D(x,0,s)$ yields:

$$\tilde{\omega}_t(x,s) = \frac{T^{\Delta}\chi q_{Lo}(2-\lambda)}{s^2 w_o}\left(1 - \frac{2q_{Lo}}{q_o}x\right)^{-\frac{\rho_r c_r \lambda}{2\rho_f c_f}} + \frac{1}{s} \tag{80}$$

Eqn. (80) must be numerically inverted, which is done using the Stehfast (1970) method.

The combined poroelastic and thermoelastic width changes can be found by adding the numerically inverted (80) to (67). The resulting pressure distribution is found by substitution of the width into (36) and numerically integrated using Simpson's 3/8 rule.

Impermeable Solution

The impermeable case does not involve any leak-off and thus no poroelastic effects are expected (see Eqn. 65). The water temperature and extent of rock cooling are however different. When $q_L(x,t) = 0$, the heat transport equations (72) and (73) become:

$$\rho_f c_f q_o \frac{\partial \tilde{T}_D(x,0,s)}{\partial x} = 2K_r \left. \frac{\partial \tilde{T}_D(x,y,s)}{\partial y} \right|_{y=0} \tag{81}$$

$$\frac{K_r}{\rho_r c_r} \frac{\partial^2 \tilde{T}_D(x,y,s)}{\partial y^2} - s\partial \tilde{T}_D(x,y,s) = 0 \tag{82}$$

The solution to (82) is:

$$\tilde{T}_D(x,y,s) = \tilde{T}_D(x,0,s) \exp\left(-y\sqrt{\frac{\rho_r c_r s}{K_r}} \right) \tag{83}$$

Substitution into (81), solving the resulting ODE, and applying (74) yields:

$$\tilde{T}_D(x,y,s) = \frac{1}{s} \exp\left[-\left(y\sqrt{\frac{\rho_r c_r s}{K_r}} + \frac{2\sqrt{K_r \rho_r c_r s}}{\rho_f c_f q_o} x \right) \right] \tag{84}$$

Eqn. (84) can be analytically inverted to the time domain:

$$T_D(x,y,t) = erfc\left(\frac{x}{\rho_f c_f q_o} \sqrt{\frac{K_r \rho_r c_r}{t}} + \frac{y}{2} \sqrt{\frac{\rho_r c_r}{K_r t}} \right) \tag{85}$$

Eqn. (85) was first derived by Bodvarrson (1969).

When there is no leak-off the solution Eqn. (85) can be substituted into the expression for the derivative of width with respect to time, Eqn. (55). Completing the integration and applying (56) results in:

$$\omega_t(x,t) = \xi_1 \exp\left(-\xi_2 x^2\right) - x\xi_3 erfc\left(x\sqrt{\xi_2}\right) + 1 \tag{86}$$

where, $\xi_1 = \frac{4\chi T^{\Delta}\sqrt{K_r t}}{w_o\sqrt{\pi\rho_r c_r}}$, $\xi_2 = \frac{K_r\rho_r c_r}{\left(q_o c_f \rho_f\right)^2 t}$, and $\xi_3 = \frac{4\chi T^{\Delta} K_r}{w_o q_o \rho_f c_f}$.

Injection into an Infinite Radial Fracture

Mathematical Model

The geometry of interest is shown in Figure 23. Axisymmetry will be assumed, allowing for the θ direction to be ignored. The fracture is flat and infinite in extent. Other applicable assumptions were postulated in the previous section. The derivations for fluid flow, heat transport, and deformation are similar to those derived in the previous section. Therefore REV analysis will not be shown, and derivations will be brief as because the techniques are similar to those applied in the previous section.

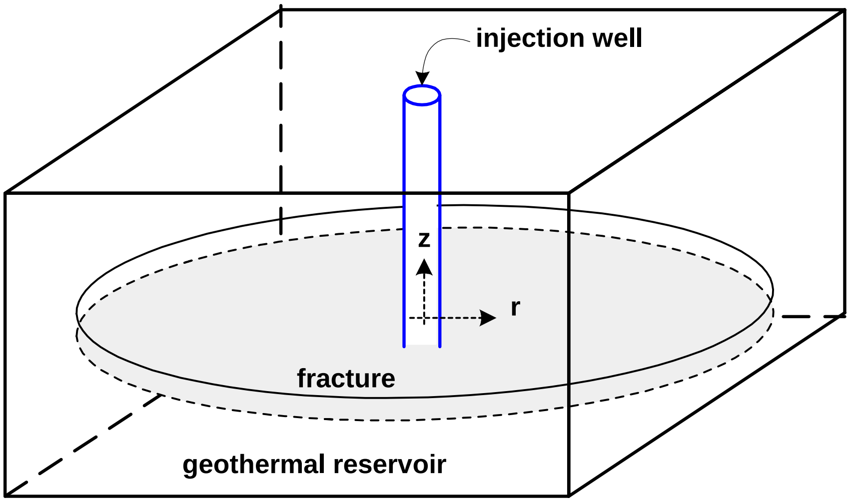

Figure 23. Mathematical Model for Injection into Infinite Radial Fracture.

Fluid Flow in Infinite Radial Fracture and Reservoir Rock

The only notable difference is that the flow rate per unit height is now a function of r:

$$q(r,t) = \frac{Q(r,t)}{2\pi r} \tag{87}$$

where $Q(r,t)$ is the injection rate. Utilizing (87) the momentum equation (36) now becomes:

$$\frac{\partial p(r,0,t)}{\partial r} = -\frac{6\mu_f}{\pi r w^3(r,t)} Q(r,t) \tag{88}$$

and the diffusion equation becomes:

$$\frac{\partial^2 p(r,z,t)}{\partial z^2} = \frac{1}{c_D}\frac{\partial p(r,z,t)}{\partial t} \tag{89}$$

The boundary and initial conditions for this solution system become:

$$p^*(r,z,0) = 0 \tag{90}$$

$$\frac{\partial p^*(\infty,0,t)}{\partial r} = 0 \tag{91}$$

Note that (91) is a no flow boundary condition, which accommodates the infinite domain; Eqns. (88)-(91) form the solution system.

Heat Transport in Infinite Radial Fracture and Reservoir Rock

Similarly to (42), the heat transport in the fracture becomes:

$$\frac{\rho_f c_f Q(r,t)}{2\pi r}\frac{\partial T_D(r,0,t)}{\partial r} = 2K_r \left.\frac{\partial T_D(r,z,t)}{\partial z}\right|_{z=0} \tag{92}$$

and similarly to (44) the heat transport in the reservoir rock becomes:

$$\frac{K_r}{\rho_r c_r}\frac{\partial^2 T_D(r,z,t)}{\partial z^2} - \frac{\partial T_D(r,z,t)}{\partial t} - q_L(r,t)\frac{\partial T_D(r,z,t)}{\partial z} = 0 \tag{93}$$

The initial and boundary conditions of the system are:

$$T_D(r,z,0) = 0 \tag{94}$$

$$T_D(0,0,t) = 1 \tag{95}$$

Eqns. (92)-(95) are the solution system for the temperature.

Fracture Aperture Changes from Thermoelastic and Poroelastic Effects

The time dependent width equation is:

$$\begin{aligned}\frac{\partial w(r,t)}{\partial t} &= \frac{-2T^{\Delta}\chi K_r}{\rho_r c_r}\left.\frac{\partial T_D(r,z,t)}{\partial z}\right|_{z=0} \\ &+ 2T^{\Delta}\chi q_L(r,t)T_D(r,0,t) + \frac{2\eta c_D}{G}\left.\frac{\partial \Delta p(r,z,t)}{\partial z}\right|_{z=0}\end{aligned} \tag{96}$$

Eqn. (96) is identical to (55) because the differences in the model geometry have been incorporated into the temperature and pressure solution systems. Note that the expression for the displacements would be different in the cylindrical coordinate system; however, the axisymmetric assumptions lead to an equation that is identical to the case of one-dimensional line fracture problem.

Impermeable Solution

As the flow varies in the radial direction, it can be expected that leak-off should also be radially varying. But, using a radially variable leak-off creates difficulty in obtaining a simple solution. Therefore, the leak-off is modeled using the Carter leak-off model given as:

$$q_L(r,t) = \frac{C_\ell}{\sqrt{t}} \tag{97}$$

where C_ℓ is the leak-off coefficient that is obtained experimentally in the lab or in the field. However this will not yield a useful solution as will now be shown. Utilizing (97) the fluid velocity becomes:

$$v(r,t) = \frac{Q_o}{2\pi\, r\, w_o} - 2\frac{C_\ell}{\sqrt{t}} \tag{98}$$

Expressing in flow rate per unit height:

$$q(r,t) = \frac{Q_o}{2\pi\, r} - 2\frac{C_\ell w_o}{\sqrt{t}} \tag{99}$$

Ignoring the fluid-solid coupling, (99) can be substituted into the momentum equation (88) and integrated:

$$p^*(r,0,t) = -K_1^R \ln\left(\frac{r}{R}\right) + \frac{K_2^R}{\sqrt{t}}\left(r - R\right) \tag{100}$$

where $K_1^R = \frac{6\mu_f Q_o}{\pi w_o^3}$, $K_2^R = \frac{24\mu_f C_\ell}{w_o^2}$, and R is a reference fracture radius which must be sufficiently large such that $\frac{\partial p^*(R,0,t)}{\partial r} \approx 0$. The solution to (89) is similar to the line fracture solution (61):

$$p^*(r,z,t) = p^*(r,0,t) \times erfc\left(\frac{z}{2\sqrt{c_D t}}\right) \tag{101}$$

Ignoring thermal effects (101) can be substituted into (96):

$$\frac{\partial w_p(r,t)}{\partial t} = -\frac{2\eta\sqrt{c_D}}{G\sqrt{\pi t}} \Delta p^*_{poro}(r,0,t) = \frac{-2\eta K_2^R \sqrt{c_D}}{G\sqrt{\pi}\, t}\left(R - r\right) \tag{102}$$

Integrating both sides with respect to time and applying the boundary condition $\omega_p(R,0) = 1$ results in:

$$\omega_p(r,t) = \frac{-2\eta K_2^R \sqrt{c_D}\,(R-r)}{G\sqrt{\pi}\, w_o} \ln(t) + 1 \tag{103}$$

Using input values from Table 6 (pg. 69) and typical values of C_ℓ (in the range of 8.05E-5 m/s$^{1/2}$ to 4.02E-4 m/s$^{1/2}$ see e.g. www.calfrac.com; Jeffrey and van As, 2003) in Eqn. (103) does not yield a substantial difference in the width, as shown in Figure 24. As a result, the constant leak-off solution will not provide reasonable results. Therefore, only an impermeable solution will be considered. Eqn. (103) differs from (67) in the logarithmic, rather than square root, relationship between width change and time. This is a result of the $\sqrt{t}$ (see Eqn. 100) incorporated into the leak-off. The reason that a constant leak-off solution used for the line fracture does not work for an infinite radial fracture is the radial varying flow. In this case, not only is the flow rate per unit lateral extent (height in the rectangular case) no longer constant, but the area exposed to leak-off is continually increasing with radial distance. Therefore, the assumption of a constant leak-off is not suitable, and thus leads to unreasonable results.

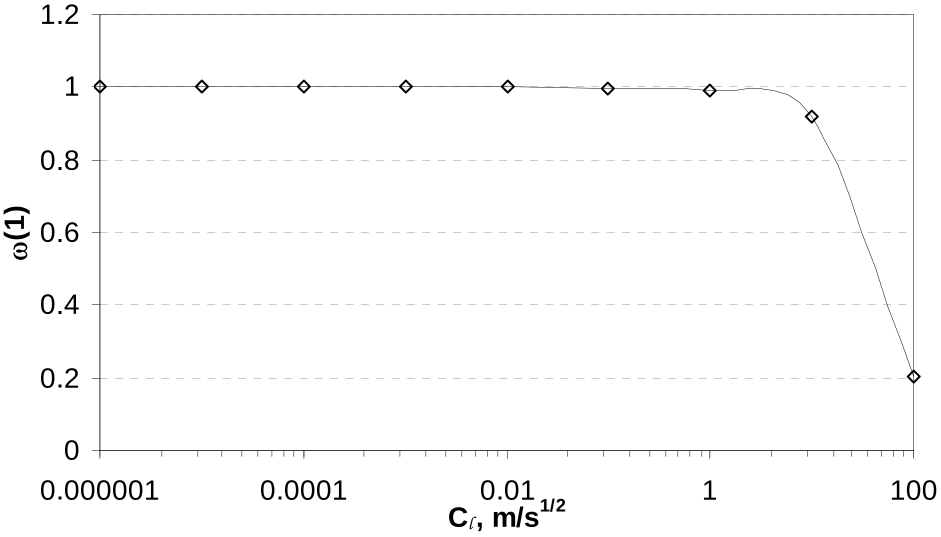

Figure 24. Dimensionless Width at r = 1 for Various Values of C_ℓ after 5 years of Injection.

When there is no leak-off the heat transport equations become:

$$\frac{Q_o \rho_f c_f}{2\pi r}\frac{\partial T_D(r,0,t)}{\partial r} = 2K_r \left.\frac{\partial T_D(r,z,t)}{\partial z}\right|_{z=0} \tag{104}$$

$$\frac{K_r}{\rho_r c_r}\frac{\partial^2 T_D(r,z,t)}{\partial z^2} = \frac{\partial T_D(r,z,t)}{\partial t} \tag{105}$$

Applying (94) and (95) and following similar steps shown in (81)-(85) the solution is:

$$T_D(r,z,t) = erfc\left[\left(\frac{\pi K_r}{Q_o \rho_f c_f} r^2 + \frac{z}{2}\right)\sqrt{\frac{\rho_r c_r}{K_r t}}\right] \tag{106}$$

Eqn. (106) is given in Ghassemi et al. (2003). Substitution of (106) into (96) and integrating the resulting expression with the initial condition $\omega_t(r,0) = 1$ yields the following solution:

$$\omega_t(r,t) = \xi_1 \exp\left(-\pi^2 \xi_2 r^4\right) - \pi \xi_3 r^2 erfc\left(\pi\sqrt{\xi_2} r^2\right) + 1 \tag{107}$$

where, $\xi_1 = \frac{4\chi T^\Delta \sqrt{K_r t}}{w_o \sqrt{\pi \rho_r c_r}}$, $\xi_2 = \frac{K_r \rho_r c_r}{\left(Q_o c_f \rho_f\right)^2 t}$, and $\xi_3 = \frac{4\chi T^\Delta K_r}{w_o Q_o \rho_f c_f}$.

The above analyses provide a framework for estimating the width and pressure variation associated with fluid injection/extraction into fracture and injection into infinite fracture. But, it is often of interest to assess the impact of poroelastic and thermoelastic effects when only injecting water into a system of joints. This can benefit from the study of the impact of water injection into a joint.

Injection into a Joint

In the previous sections the fluid/solid coupling was ignored, because it was assumed the injection pressure was near the S_{hmin}, and the fluid extracted was assumed to equal that of injection plus leak-off volume. However, when only injecting into a joint the pressure will build up in the fracture. This will induce changes in the pressure and in turn in the fracture width. The result is fluid-solid coupling which must be incorporated into this model. The geometry of interest is shown in Figure 24, which shows injection into the center of a symmetric joint of length 2*L*. From this problem assumptions (i)-(vii) are applicable. The joint is subject to a far field principal compressive stress, σ_n. Furthermore, it will be assumed the fracture has a finite width at its tip and the fluid pressure at the tip is constant and equal to the reservoir pressure; and there is no fracture propagation. An impermeable solution to this problem is reported in Savitski (2001). An elastic solution to this problem incorporating fracture propagation is given in Adachi (2002). A fully coupled pressure dependent, non isothermal treatment of this problem is given in Ghassemi and Zhang (2004) for a uniformly pressurized crack. For our purposes, the poroelastic and thermoelastic effects will be modeled using a partially-coupled approach used in the injection/extraction problem. Finally, effects caused from shear slip of a joint (e.g., joint dilation and stress redistribution) are not accounted for.

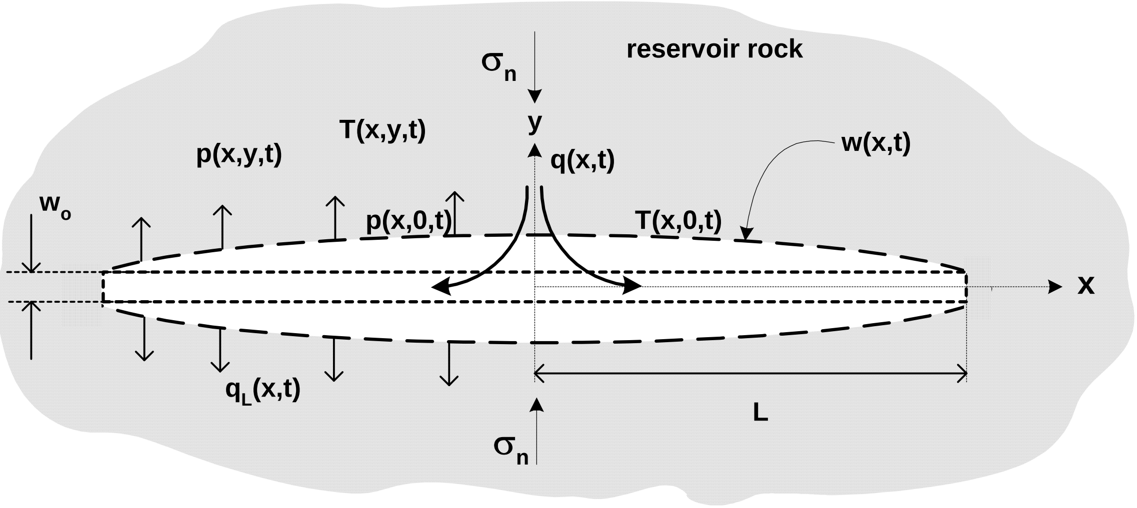

Figure 25. Mathematical Model for Injection into a Joint.

Mathematic Model

Fluid Flow in a Joint

The fluid flow in the joint will be assumed to obey the cubic law equation, which is derived in Appendix A. The expression is similar to Eqn. (35), except that the temporal changes in the width need to be incorporated into the mass balance. Combining mass balance and the momentum equation results in:

$$\frac{\partial w(x,t)}{\partial t} = -\frac{\partial q(x,t)}{\partial x} - 2q_L(x,t) = \frac{1}{12\mu_f}\frac{\partial}{\partial x}\left(w^3(x,t)\frac{\partial p}{\partial x}\right) \tag{108}$$

Fluid-Solid Deformation

Utilizing our plane strain condition, the pressure is related to the fracture width by (Sneddon, 1969):

$$p = -\frac{E'}{4\pi}\int_{-L}^{L}\frac{w(s',t)-w_o}{(s'-x)^2}ds \tag{109}$$

where *E'* is the plane strain Young's modulus given as $E/(1-v^2)$, and *s'* is given as a reference point on the fracture. Eqn. (109) is a *Hadamard finite-part integral* (Hadamard, 1923). The inverse form of (109) can be found utilizing the properties of *Hadamard finite-part integrals* given in Hadamard (1923).

Boundary and Initial Conditions

Eqn. (108) and (109) form a coupled set. The boundary and initial conditions applicable to these equations are:

$$a)\ w(L,t) = w_o \qquad b)\ p(L,t) = \sigma_n - p = p_{net} > 0$$

$$c)\ \frac{-w^3(x,t)}{12\mu_f}\left.\frac{\partial p}{\partial x}\right|_{x=0+} = \frac{q_o}{2} \qquad d)\ p(x,0) = p_{net} \tag{110a,b,c,d}$$

The first two boundary conditions assume that because of pressure loss associated with viscous effects, the fluid never actually reaches the tip of the joint, and thus pressure remain unchanged implying the width does not change at the end of the fracture. The third condition assumes both halves of the joint receive the same amount of fluid resulting from constant injection. The last assumption indicates the initial pressure in the joint required for the joint to have an initial aperture.

Steady State Solution

Although, the fracture width is assumed to change with time due to thermal and poroelastic effects, the variation can be ignored in the mass balance by assuming they proceed very slowly. Utilizing (57) to account for a constant leak-off allows (108) to become:

$$w^3(x)\frac{\partial p}{\partial x} = \frac{12\mu_f\left[q_o - (mq_o x/L)\right]}{2} \tag{111}$$

The solution system of (109) and (111) subject to (110) is coupled and non-linear implying a numerical solution. In light of this it is convenient to transform (109)-(111) into dimensionless parameters. Therefore we now define:

$$\tau = \frac{tq_o}{Lw_o} \qquad \xi = \frac{x}{L} \qquad \omega(\xi) = \frac{w(x)}{w_o} \qquad \overline{P}(\xi) = \frac{p_{net}(x)L}{E'w_o}$$
$$\gamma = \frac{q_o(1-m\xi)12\mu_f L^2}{w_o{}^4 E'} \qquad \overline{P}_{net} = \frac{p_{net}L}{E'w_o} \tag{112}$$

Substitution of (112) into (109) and (111) simplify the system to:

$$\overline{P}(\xi) = \frac{-1}{4\pi}\int_{-1}^{1}\frac{\omega(s')-1}{(s'-\xi)^2}ds \tag{113}$$

$$-\omega^3(\xi)\frac{\partial \overline{P}}{\partial \xi} = \frac{\gamma}{2} \tag{114}$$

Eqn. (110) becomes:

$$\omega(1,\tau)=1 \quad \overline{P}(1,\tau)=\overline{P}_{net} \quad \overline{P}(\xi,0)=\overline{P}_{net} \quad -\omega^3(\xi)\frac{\partial \overline{P}}{\partial \xi}\bigg|_{\xi=0+}=\frac{\gamma}{2} \qquad \text{(115a,b,c,d)}$$

Two numerical techniques will be utilized to obtain the pressure and crack opening. Eqn. (113) will be addressed first. This equation lends itself to the displacement discontinuity (DD) method (e.g. Crouch and Starfield, 1983). In the DD method, the fracture trace only is considered turning the problem into a one dimensional problem rather than a two dimensional problem. Figure 26 shows this discretization of the fracture trace. The first step is to divide the fracture trace in Figure 26 into *N* number of odd elements. This is done to permit placing the nodes at the center of each element, and to allow the center of the middle element to be the injection point. By symmetry of the problem (Figures 25 and 26) only the right side of the joint will be considered. Therefore, the number of elements used in the simulation is odd and equals $n = (N + 1)/2$. From Figure 26 the distance between the centers of neighboring elements and dimensionless nodal coordinate can readily be found:

$$\Delta\xi=\frac{2}{2n-1} \qquad \xi_i=\frac{2i}{2n-1} \qquad \text{(116a,b)}$$

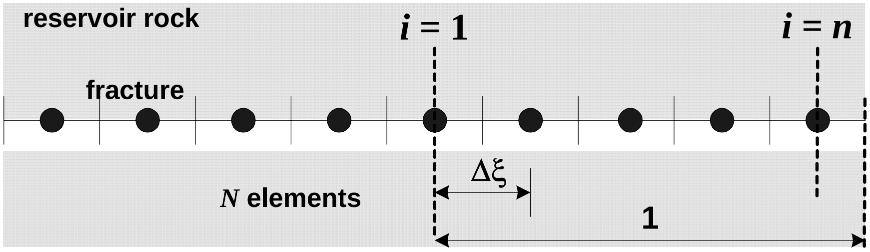

Figure 26. Discretization of Fracture Trace.

The integral in (113) must be discretized according to Figure 26. The result will be an influence coefficient matrix A_{ij} which sums the effects of each element (principle of superposition). This will create a set of n linear equations relating the width opening to the corresponding pressure at each node in Figure 26, and can be written in condensed form as:

$$\overline{P}_i = \sum_{i=1}^{n} A_{ij}\left(\omega_j - 1\right) \tag{117}$$

where

$$A_{ij} = \begin{cases} \dfrac{\Delta\xi}{4\pi}\left(\dfrac{1}{\left(\Delta\xi/2\right)^2 - \left(\xi_i - \xi_j\right)^2} + \dfrac{1}{\left(\Delta\xi/2\right)^2 - \left(\xi_i + \xi_j\right)^2}\right) & if\ j \geq 2 \\ \dfrac{\Delta\xi}{4\pi}\left(\dfrac{1}{\left(\Delta\xi/2\right)^2 - \left(\xi_i\right)^2}\right) & if\ j = 1 \end{cases} \tag{118}$$

The subscript *i* represents the influenced element (spatial coordinate), and *j* represents the displacement discontinuity at the influencing node. A more complete explanation of (118) is shown in Appendix C. Also, Eqn. (117) and (118) are derived in Crouch and Starfield (1983). Note in (118) that when $j \geq 2$ another term is added. This is a result of symmetry about the *x*-axis. If this second term was not included then the displacements on the top (1st quadrant in Figure 25) would only be calculated.

The flow equation (114) is also discretized using a forward difference approximation between each of the nodes:

$$-\left(\frac{\omega_{i+1} + \omega_i}{2}\right)^3 \frac{\overline{P}_{i+1} - \overline{P}_i}{\Delta\xi} = \frac{\gamma}{2} \tag{119}$$

or

$$\overline{P}_i = \frac{4\gamma\Delta\xi}{\left(\omega_{i+1} + \omega_i\right)^3} + \overline{P}_{i+1} \tag{120}$$

The index range of i is 1 to n-1. Eqns. (117) and (120) can then be iteratively solved to give a solution for the pressure and width. This is accomplished by assuming an initial normalized width (e.g. $\omega_i = 1$). The initial width array can be substituted into (120), which will give a pressure array of nodal pressures (since initially $\overline{P}_n = \overline{P}_{net}$). This pressure array is then substituted into (117) where the width array is solved for. The new width array is substituted back into (120) to yield a new pressure array. This is continued in an iterative process till the new and old pressure and width arrays are equal. Note that for the first iteration, the pressure at the last node $\overline{P}_n$ equals $\overline{P}_{net}$, however, this is not the case for subsequent iterations (i.e. the pressure at the last node $\overline{P}_n$ is not equal to $\overline{P}_{net}$ after the first iteration, see Figure 26). This is because the last node is not at the fracture tip but is a distance $\Delta\xi/2$ away from the fracture tip. Therefore, at the n^{th} node the pressure is set equal to a forward difference approximation with the fracture tip (where $\overline{P} = \overline{P}_{net}$):

$$\overline{P}_n = \frac{4\gamma(\Delta\xi/2)}{\left(1 + \omega_n\right)^3} + \overline{P}_{net} \tag{121}$$

Eqn. (121) was arrived at utilizing similar steps to (119) and (120).

Poroelastic Effects

The normalized poroelastic width change, $\omega_p(x,t)$, is found by utilizing the derived line fracture width solution (67) and adding it to the permeable elastic solutions (elastic solution with leak-off). The corresponding pressure is then numerically integrated. Note that $K_1^d(x) = \frac{12\mu_f q_{Lo}}{w^3(x)}$ is now used in (67) because of the fluid/solid coupling.

Thermoelastic Effects

The thermoelastic induced width change, $\omega_t(x,t)$, is incorporated by adding the numerically inverted result of (80) to the calculated width in the numerical solution. This is illustrated in Figure 26. *Note that the time must be small enough such that the boundary condition* (*115b*) *is still satisfied* (*i.e.* $\omega_t(x,t)$ *at* $x = L$ *must be* 1). The point will be explored further in Chapter VII.

Parameter Values

The presented mathematical models and solutions had many associated parameters. Typical values for hornblende biotite quartz diorite and water are given in Table 6.

Table 6. Parameters Used for Mathematical Model Calculations.

Parameter	**Value**	**Units**	**Reference**
w_o	0.001	m	Assumed
v	0.185	-	Rose et al. (2004)
α_T	0.000008	1/ºK	Assumed
T^{Δ}	80	ºK	Ghassemi et al. (2003)
K_r	2.88	W/m-ºK	Assumed
ρ_r, ρ_f	2820, 1000	kg/m^3	Rose et al. (2004)
c_r, c_f	1170, 4200	J/kg-ºK	Assumed
μ_f	0.001	N-s/m^2	Assumed
G	27500	MPa	Rose et al. (2004)
c_D	0.000022	m^2/s	Assumed
η	0.183	-	calculated from Rose et al. (2004)

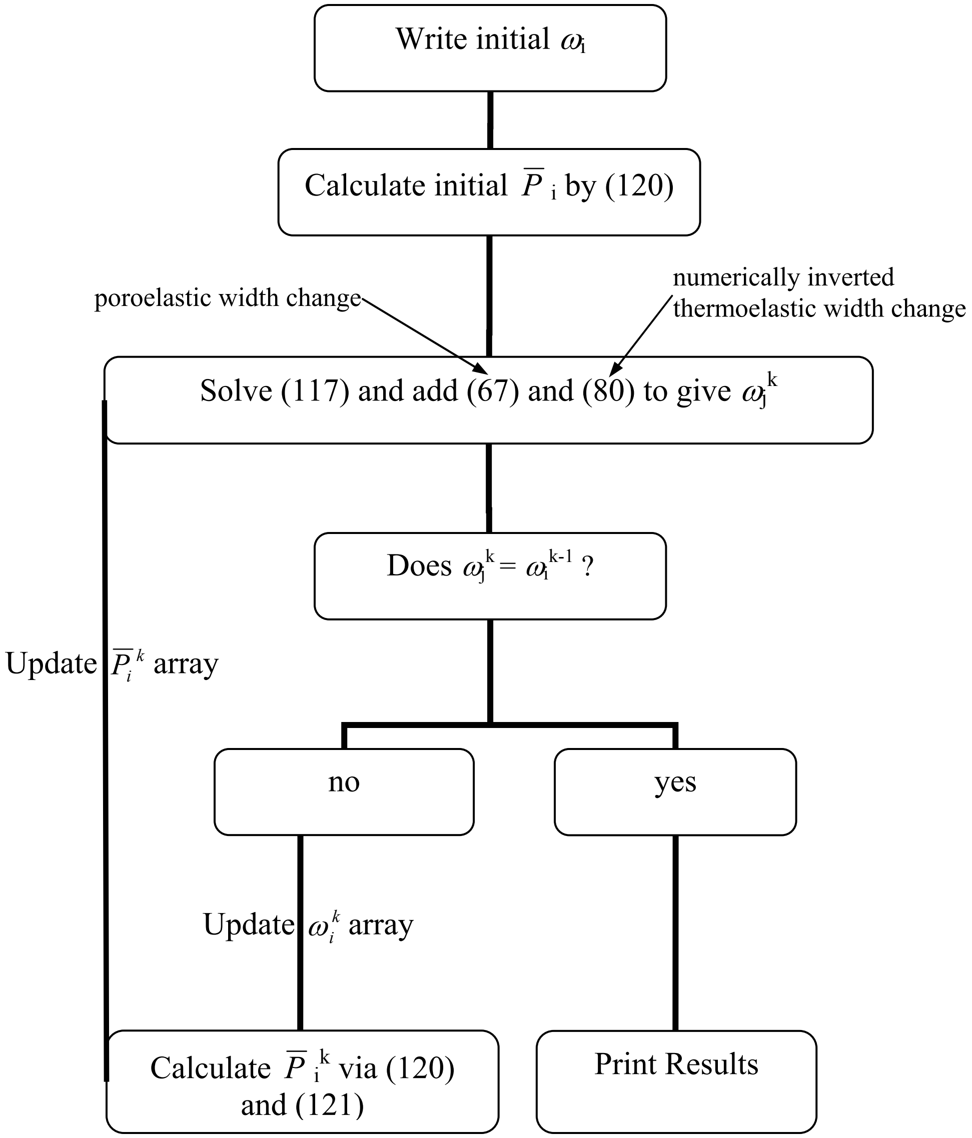

Figure 27. Flowchart for Fluid-Solid Coupling with Thermoelastic and Poroelastic Effects for each *k* Step. Note (67) is Poroelastic Width Change, and (80) is Thermoelastic Width Change.

CHAPTER V

MECHANICAL EFFECTS OF WATER INJECTION/EXTRACTION INTO A LINE FRACTURE

In this chapter the expressions derived in Chapter IV for thermoelastic and poroelastic effects of injection/extraction into a line fracture (Model I) are applied to fractures of the type found in Coso. It is of interest to investigate these effects on fracture permeability. As implied in such works as Pine and Batchelor (1984) and Barton et al. (1998) these critically stressed fractures can control permeability. Thus, the fracture permeability enhancement is considered by estimating the injection rate required to critically stress a fracture using the injection/extraction model for a line fracture. The magnitude of slip and fracture dilation, and stress redistribution is not considered at this time. We will then include the poroelastic effects, thermoelastic effects, and combined poroelastic and thermoelastic effects to investigate their effect on fracture permeability.

The Onset of Joint Slip in an Injection/Extraction Operation

In Chapter III the pressure needed to critically stress a fracture in the Coso EGS was quantified. It is now of interest to estimate the minimum injection rate needed to critically stress a fracture to possibly enhance its permeability in an injection/extraction system (see Figure 18). To investigate this, the simple model of a line fracture is used that assumes:

i) The system is isothermal

ii) Fluid/Solid coupling is negligible *iii)* The rock is impermeable

iv) Constant injection rate, $q(x,t) = q_o$

All other relevant assumptions are given in Chapter IV. Note that assumptions (*iii*) and (*i*) allow the poroelastic and thermoelastic effects to be ignored, respectively. Utilizing all of the assumptions, the momentum equation (36) becomes:

$$\frac{\partial p^*(x,t)}{\partial x} = -\frac{12\mu_f q_o}{w_o^3} \tag{122}$$

where $p^*(x,t) = p^*(x,0,t)$ is the pressure change or the induced pressure in the fracture. The boundary condition for (122) is:

$$p^*(0,t) = p_o^+ \tag{123}$$

where p_o^+ is the pressure increase required to critically stress the fracture at the injection point ($x = 0$) (see Figure 16, 17, and 28). Completing the integration in (122) and applying (123) gives:

$$p^*(x,t) = -\frac{12\mu_f q_o}{w_o^3} x + p_o^+ \tag{124}$$

Eqn. (124) is geometrically illustrated in Figure 28; it allows us to find the minimum injection rate necessary to critically stress the fracture. By similar triangles in Figure 28, (122) is set equal to - p_o^+ / L (mathematically a negative slope); solving the resulting expression for the injection rate yields:

$$q_o^{joint} = \frac{p_o^+ w_o^3}{12 L \mu_f} \tag{125}$$

Figure 28 also shows if the pressure at $x = 0$ would be greater than p_o^+ , then it can be expressed in terms of p_o^+ using a weighting factor, n. This is done to account for the variation of p_o^+ with respect to different joint orientations (see Figure 17) and will be elaborated on later in the section.

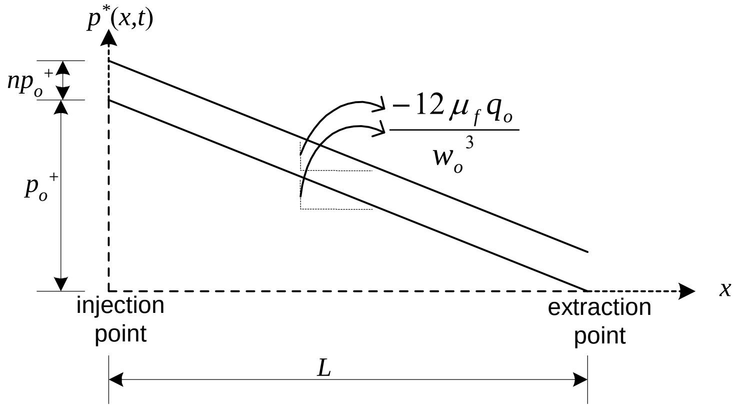

Figure 28. Induced Pressure Distribution to Critically Stress a Fracture.

It is readily observed from (125) that the injection rate is inversely related to the fracture length. In light of this, a long fracture of length 1000 m is chosen in an effort to obtain realistic injection rates. The other parameters in (125) are specified in Table 6. The results for the observed joint orientations at the injection depth of 2316 m are given in Table 7 and also Figure 29 for all joint orientations. For most joint orientations, the calculated values are high considering typical injection values are 5E-7 to 2E-4 m^2/s (e.g. Cheng et al., 2001). These injection rates will critically stress joints in the range of $\theta = 21^\circ$-44° for a friction angle of 25º.

Table 7. Injection Rates (in m^2/s) Needed to Critically Stress a Joint for Various Orientations.

	β = 60º	β = 70º	β = 80º
ϕ'	q_o	q_o	q_o
35º	0.001029	0.001112	0.001524
45º	0.001625	0.001556	0.001761
55º	0.002043	0.001865	0.001924

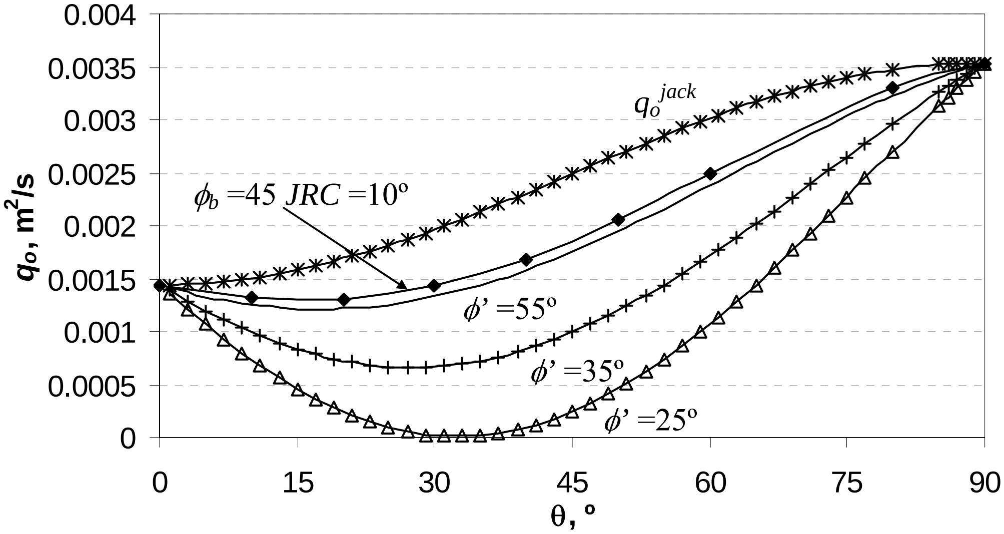

Figure 29. Injection Rates Required to Critically Stress and Jack a Fracture.

Figure 29 also shows the injection rate required for jacking, q_o^{jack}, can readily be found by substitution of (p_{jack} -p_o) into (125) for p_o^+. Using the ratio of the injection rate needed for injection pressures of $(n+1)p_o^+$ and p_o^{jack}, along with the expression for p_c^{joint}, Eqn. (27), and p_c^{jack}, Eqn. (28); the following expression is obtained:

$$\frac{q_o^{jack}}{q_o^{joint}} = \frac{p_c^{jack} - p_o}{p_c^{joint} - p_o} = \frac{A - \cos(2\theta)}{A - \dfrac{\sin(2\theta)}{\tan\phi'} - \cos(2\theta)} = \begin{cases} < n+1 & critically\ stressed \\ \geq n+1 & jacking \end{cases} \tag{126}$$

where $A = \dfrac{\sigma_1' + \sigma_3'}{\sigma_1' - \sigma_3'}$ is the ratio of the mean effective stress to the deviatoric stress. Eqn. (126) is plotted in Figure 30 and can be employed to determine the joints most conducive to slip before jacking. The results for the case of n = 1 can be illustrated in Figure 30. It is observed that jacking would occur except for the case of ϕ' = 35° where jacking would not occur for joints orientated at θ =15°-55°. Note also Figure 30 shows at a critical orientation, an upper bound friction angle allows injection to critically stress the entire joint ($n = 1$) without jacking. To investigate this, the inflection point of (126) is found by applying the following expression:

$$\frac{d}{d\theta}\left(\frac{q_o^{jack}}{q_o^{joint}}\right)=\frac{2\sin(2\theta)}{A-\dfrac{\sin(2\theta)}{\tan\phi}-\cos(2\theta)}-\frac{\left[A-\cos(2\theta)\right]}{\left(A-\dfrac{\sin(2\theta)}{\tan\phi}-\cos(2\theta)\right)^2}\left(-2\frac{\cos(2\theta)}{\tan\phi}+2\sin(2\theta)\right)=0 \tag{127}$$

Inspection of (127) shows θ cannot be determined analytically; therefore it must be solved for iteratively, which yields a $\theta_{q(\max)}$ of 32.5º or 33º. Letting A approach ∞, $\theta_{q(\max)}$ approaches 45º. The curve in Figure 30 also approaches the line $q_o^{jack} / q_o^{joint} = 1$. This shows that as the loading approaches hydrostatic conditions, all orientations become equal to $\theta_{q(\max)}$. As A approaches 1 (uniaxial loading), $\theta_{q(\max)}$ approaches 0º which is the orientation when $q_o^{joint} = q_o^{jack}$. Indeed, at $A = 1$, jacking will occur for all orientations since $\sigma'_3 = 0$. Also note that as A decreases, the q_o^{jack} / q_o^{joint} value increases greatly at $\theta_{q(\max)}$. This will continue to occur until the confining pressure is so low that jacking will prevail at pressurization. Since the in-situ stress is not uniaxial, the stress conditions will be conducive to critically stress joint orientations near or at $\theta_{q(\max)}$.

The upper bound of the friction angle for critically stressing a joint at an injection rate of $(n+1)q_o^{joint}$ can now be found for $\theta_{q(\max)}$. By setting Eq. (127) equal to $n+1$, substituting $\theta_{q(\max)}$ for θ, and solving for ϕ' we obtain:

$$\phi'_{\max}=\tan^{-1}\left(\frac{(n+1)\sin(2\theta_{q(\max)})}{A-\cos(2\theta_{q(\max)})}\right)$$

(128)

Applying Eq. (128) with n=1, yields a $\phi'_{\max}$ of 42.88° or 43° (see Figure 30); this implies injection rates that correspond to a $2p_o^+$ injection pressure will not jack the joint for ϕ' values greater than 43°.

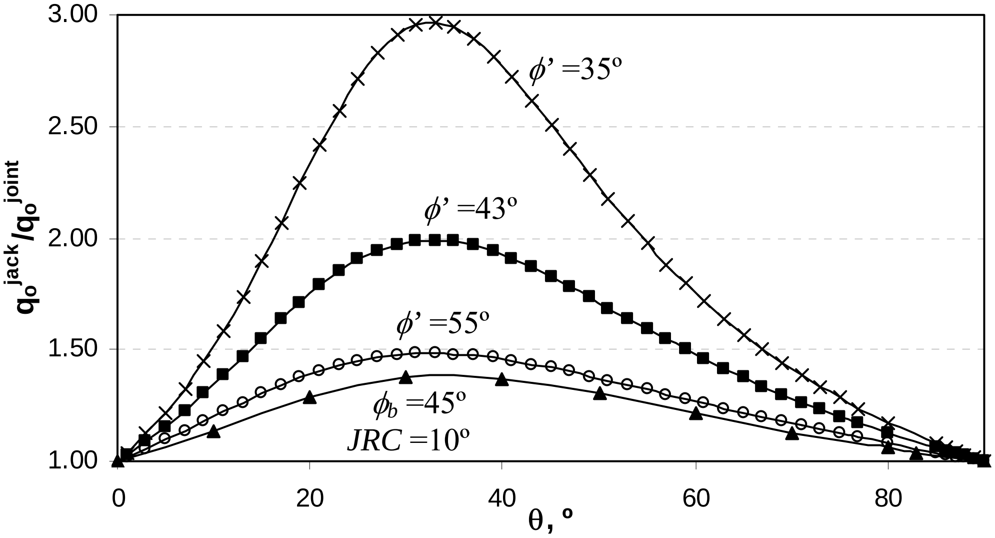

Figure 30. q_o^{jack} / q_o^{joint} for Various Friction Angles.

Finally, Figure 30 also shows a curve for a non-linear failure model, which deviated up to 7.88% from the corresponding linear failure envelope. This shows non-linear joint failure envelopes cannot always be ignored in considering the critical injection rates.

The above analysis did not take into account fluid loss into the reservoir rock. Thus, it is of interest to investigate how the pressure distribution and fracture aperture will change when fluid loss is considered. This is accomplished next by using the constant leak-off solutions derived in Chapter IV for injection/extraction into a line fracture.

Influence of Fluid Leak-off on Fracture Width and Pressure

The problem considered is the same as in the previous section except now the rock is permeable (L = 1000 m and see Table 6 for other parameters). A high and low injection rate of 1E-4 m^2/s and 1E-5 m^2/s, respectively, will be used. The fluid flow and fracture deformation (fluid/solid coupling) is ignored in this problem as it will be considered in Chapter VII.

Before presentation of the induced effects associated with fluid loss note the following definitions:

- $\Delta p^*_{i-j}(x,t)$: *is induced pressure change from the i case minus induced pressure change from the j case*.
- $\Delta \omega_{i-j}(x,t)$: *is the induced width change from the i case minus induced width change from j case*.
    - where *i* and *j* can be: *e* = elastic case, *p* = poroelastic case, *t* = thermoelastic case, *tp* = combined thermoelastic and poroelastic case, *imp* = impermeable case, *perm* = permeable case

Isothermal Poroelastic Effects

Figure 31 shows the temporal variation of the normalized net fracture width ($\omega_p(x,t) = w_p(x,t)/w_o$) resulting from poroelastic effects at the inlet for different leak-off values and injection rates. It is observed that the rate of aperture increase resulting from rock expansion is initially large and decreases with time. This can be explained by inspecting Eqn. (67) which indicates the fracture opening is related to the $\sqrt{t}$. It is also noted that a smaller injection rate results in a smaller width change. This is because the pressure difference responsible for the width change is smaller (see Eqn. 67). The steady-state poroelastic effects considered herein is proportional to the difference in pressure between the fracture and the rock. Hence a higher injection pressure means a higher poroelastic effect.

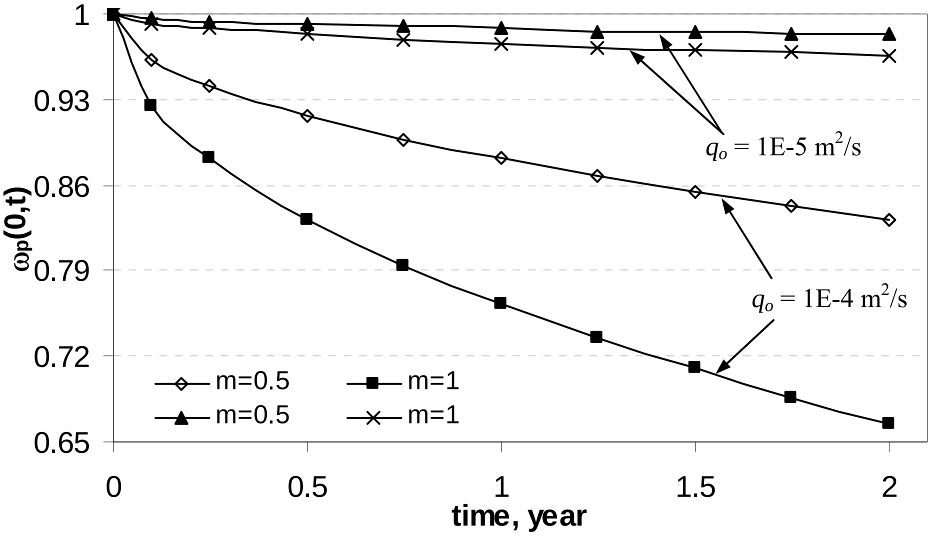

Figure 31. Normalized Net Fracture Width at the Inlet from Poroelasticity for Different Injection Rates.

Next, the normalized net fracture width along the fracture trace resulting from poroelastic deformation is plotted in Figure 32 for different values of *m* and injection rates after 6 months of injection. The contraction of the fracture is relatively small. This can be attributed to the high value of *G* and low value of c_D. The maximum reduction of width occurs at the injection point, because this is where the poroelastic induced pressure $\Delta p^*_{poro}(x,0,t)$ is the highest. In other words, as fluid in the fracture is lost to the reservoir rock, the pressure difference between the fracture and the reservoir rock also decreases along its length (by the momentum equation and pressure balance) thus decreasing the induced poroelastic width changes along the crack. It is also observed that as the injection rate is increased, the differences between the width changes for different *m* values become more pronounced. This was also observed in Figure 31 and is a result of larger variations between the induced pressure and reservoir pressure.

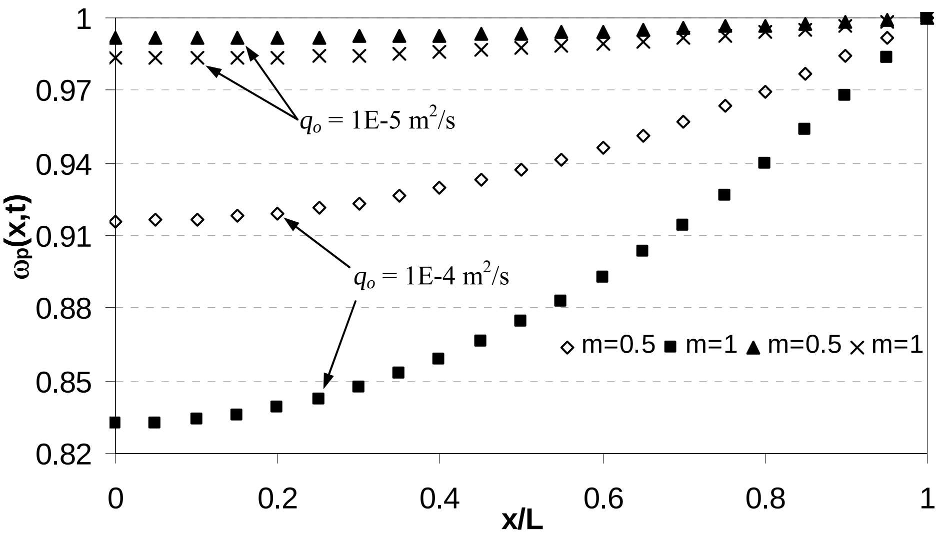

Figure 32. Normalized Net Fracture Width Showing the Influence of Poroelasticity after 6 Months of Injection.

The corresponding pressure distribution in the fracture for the elastic case (Eqn. 58) and the poroelastic case (Eqn. 68 numerically integrated) normalized with respect to the *isothermal impermeable injection pressure* ($p^*_{imp}(0,t)$ = 1.2 MPa for q_o = 1E-4 m^2/s and $p^*_{imp}(0,t)$ = 0.12 MPa for q_o = 1E-5 m^2/s) is plotted in Figure 33. The elastic case appears as solid lines, and the poroelastic case appears as symbols. The results show an increase in pressure as a result of the reduction in the width. However, although the width contracts due to the poroelastic effects, the contraction is not pronounced enough for the pressure to increase above the impermeable elastic case. Indeed, increasing the injection rate could increase the pressure for the poroelastic case above the impermeable elastic case as will be shown in Chapter VII. For the injection rate of q_o = 1E-5 m^2/s the differences are nearly negligible. This is because of the small width contraction observed in Figure 32. Also, note that as the leak-off increases, the pressure profile becomes more parabolic. This is due to mass balance (under constant leak-off conditions) because increasing the leak-off decreases the amount of fluid in the fracture thus resulting in a decreased pressure gradient in the momentum equation (36). For severe cases of leak-off ($m = 1$) Figure 33 shows almost no pressure gradient because at $x = L$, $q(L,t) = 0$

To further illustrate the differences between induced pressure in the fracture for the elastic case (with leak-off) and poroelastic case, the differences between the curves for the impermeable case and permeable cases from Figure 33 are plotted in Figure 34. Indeed the pressure profiles for the elastic case (solid lines) show the maximum difference in pressure is at the injection point and decreases towards the extraction point. For the poroelastic case, the pressure profiles show the difference in pressure increases to a point and then decreases to the extraction point. Figure 34 shows this effect is enhanced by increasing the injection rate and the degree of leak-off. The reason for this effect is that the width contraction at the injection point will increase the pressure. However as fluid is lost to the formation and the width contraction is reduced, the pressure difference in Figure 34 will cease to increase and will decrease in a similar manner to the elastic case. This is a result of the poroelastic effects becoming negligible near the extraction point. That is the induced poroelastic pressure $\Delta p^{*}_{poro}(x,0,t)$ is reduced to zero because the pressure in the fracture and reservoir approach the same value at $x = L$. Figure 34 therefore illustrates the need to incorporate the poroelastic effects when fluid loss is present and injection rates are high.

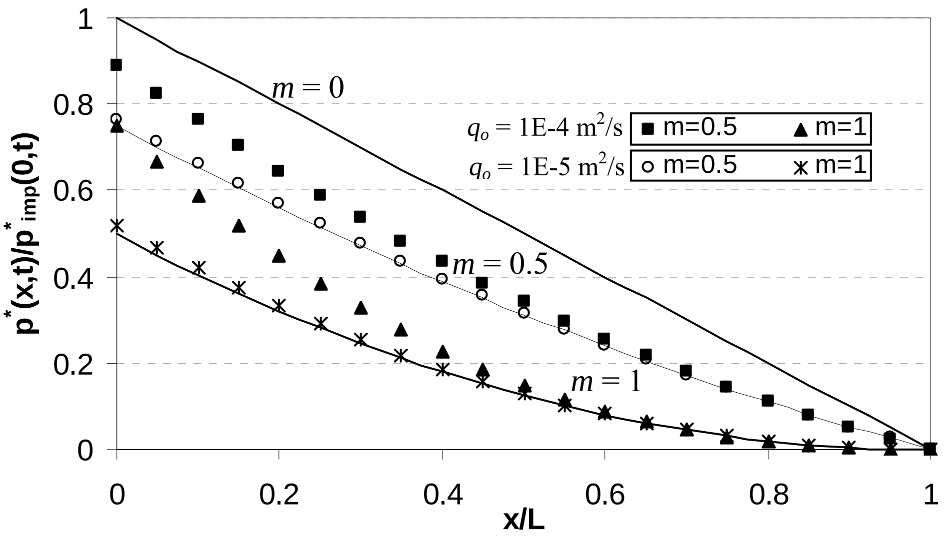

Figure 33. Normalized Induced Pressure in Fracture for no Leak-Off (m = 0), and Various Degrees of Leak-Off and Injection Rates after 6 months of Injection. Symbols: Poroelastic; Solid Curves: Elastic.

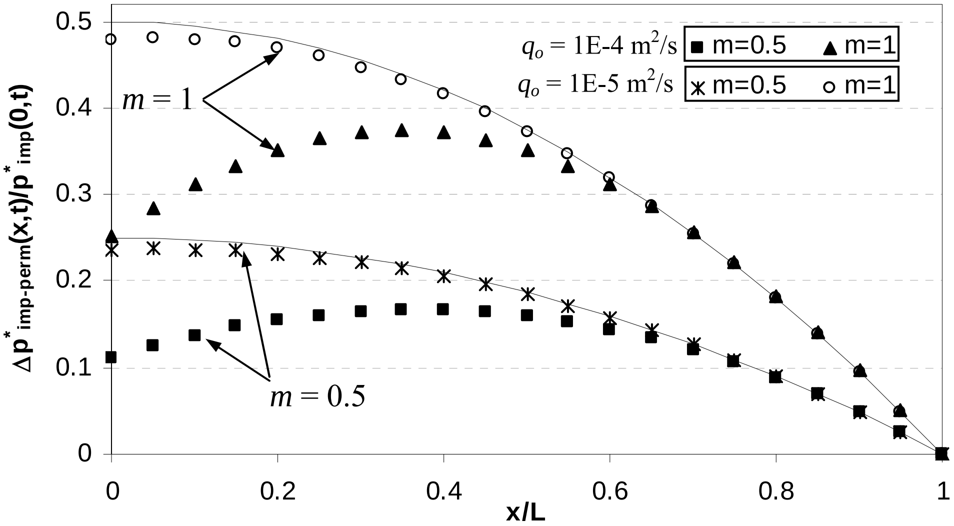

Figure 34. Difference between the Impermeable Normalized Induced Pressure and the Permeable Normalized Induced Pressure with and without Poroelastic Effects. Symbols: Poroelastic; Solid Line: Elastic.

Thermoelastic Effects

The isothermal assumption is now relaxed in the previous example. All other parameters and assumptions from the previous section are applicable (L = 1000 m and see Table 6). Figure 35 shows the temporal variation of normalized net fracture width

($\omega_t(x,t) = w_t(x,t)/w_o$) resulting from thermoelastic effects at the inlet for different leak-off values. The injection rate in Figure 35 is 1E-4 m^2/s. Inspection of (86) shows the normalized net fracture width is independent of the injection rate for the impermeable case at $x = 0$. However, as illustrated in Figure 36 ($\omega_{\text{imp}}(0,t)$ denotes net fracture width at inlet for impermeable case) the opening for permeable cases will increase with injection rate due to the enhanced thermoelastic effect as a result of the increased heat flux from leak-off. Figure 36 is after 1 month of injection. We note that Figure 35 has a similar shape to Figure 31; however its sign is the opposite. The contraction of the rock related to cooling leads to large displacements. Also, by comparison of Figure 35 with Figure 31 it appears the thermoelastic effects dominate, which would be expected for mechanically hard rock in the presence of a large temperature perturbation. This indicates that indeed *fracture permeability enhancement in EGS type environments are largely controlled by the thermoelastic effects and not the hydraulic effects.*

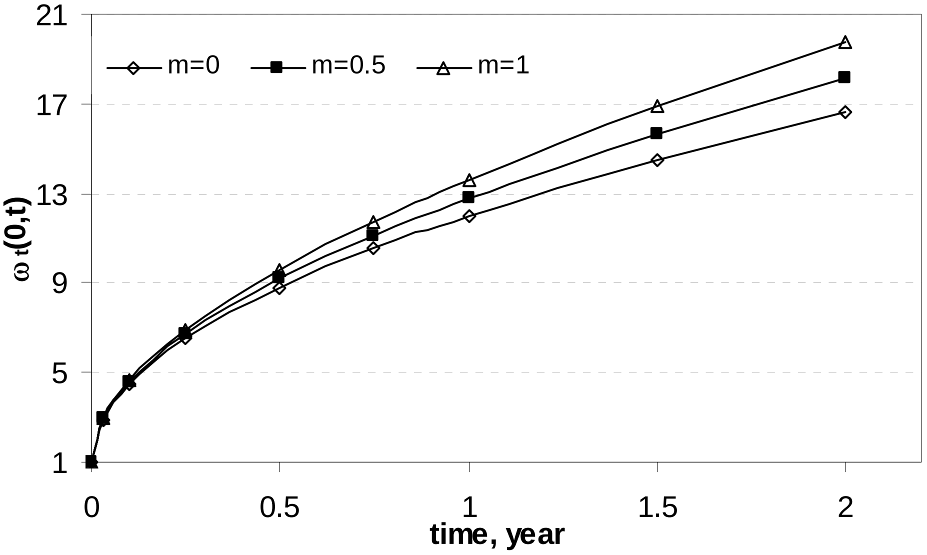

Figure 35. Normalized Net Fracture Width at the Inlet Resulting from Thermoelasticity.

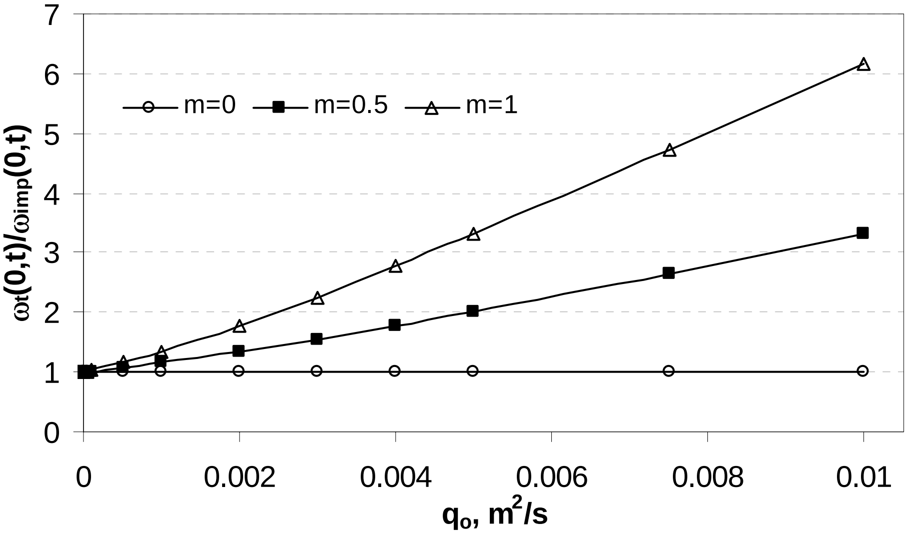

Figure 36. Variation of Net Fracture Width at Inlet Normalized with Respect to Impermeable Case for Various Injection Rates and Leak-Off Values after 1 Month.

Although for $m = 0$ the injection rate is independent of the opening at the injection point, Figure 37 shows there is a spatial relationship between the injection rate and width change. Figure 37 is after 3 months of injection. Indeed, the spatial extent of the induced width change increases with greater injection rates. This is due to the increase in the advective heat transport in the fracture.

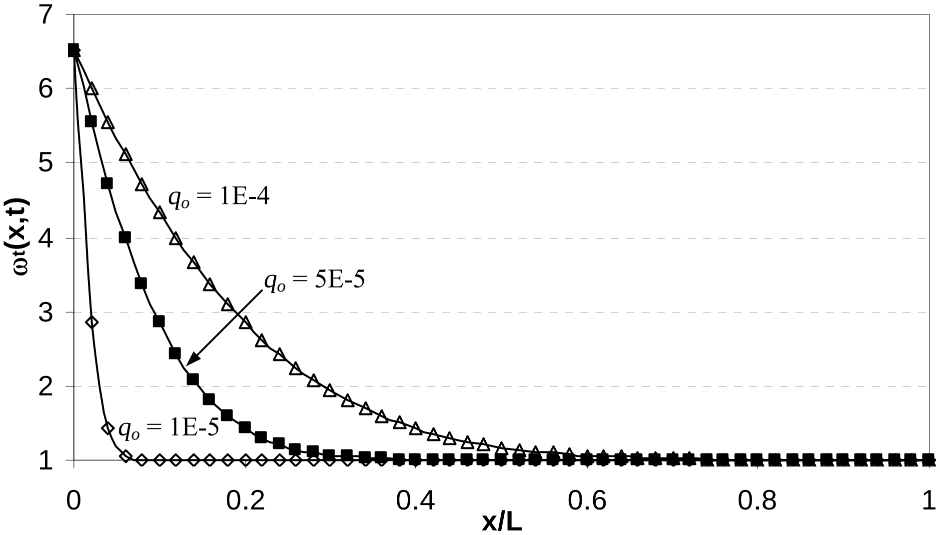

Figure 37. Normalized Net Width for Various Injection Rates after 3 Months of Injection.

The pressure distributions corresponding to the net fracture widths in Figure 37 are plotted in Figure 38. These pressures have been normalized with their respective isothermal impermeable injection pressures. It is readily observed the normalized pressure has decreased more for the higher injection rates. This is a result of the width increase extending further along the fracture trace for higher injection rates. As expected, beyond the zone influenced by thermoelastic width changes, the pressure profile follows the isothermal elastic case.

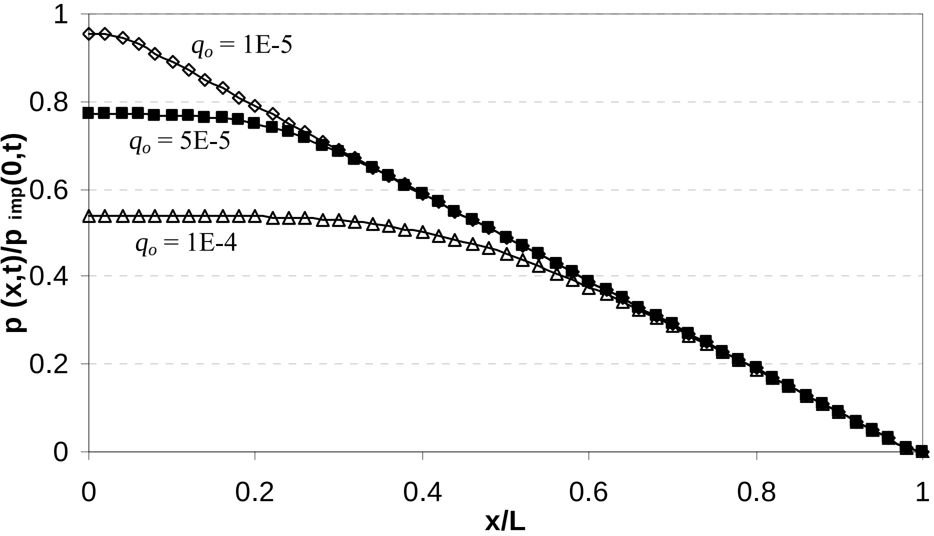

Figure 38. Thermoelastic Induced Normalized Pressure in Fracture for Various Injection Rates (in m^2/s) after 3 Months of Injection**.**

It is now of interest to investigate the temporal effects of the normalized thermoelastic net fracture width and the corresponding pressure for various degrees of leak-off. To do so a constant injection rate of 1E-4 m^2/s will be applied, all other parameters will be the same. The normalized net fracture width is shown in Figure 39 and the corresponding pressure distribution normalized with respect to the isothermal impermeable injection pressure is plotted in Figure 41. At early times it is evident the effect of leak-off on changes in the fracture width is negligible. This notion is readily observed in Figure 40 where the differences in the permeable and impermeable width opening from Figure 39 are plotted. Near the injection point the aperture increases more for the permeable case; however near the extraction point the aperture increases more for the impermeable case. The effect is enhanced with increasing time. This result is due to a longer residence time of the fluid in the fracture for the permeable case, and also a result of the added heat transport component in the rock, advection (from the leak-off velocity). This causes more heat flux into the rock so the thermoelastic effect is enhanced (near the injection point). As the fluid is lost into the formation, the fluid velocity decreases and the thermoelastic effect is reduced (near the extraction point). It is worth noting that although more heat can be extracted in the permeable cases the amount of total energy extracted is still greater for the impermeable case, because more water is extracted (Ghassemi and Cheng, 2001).

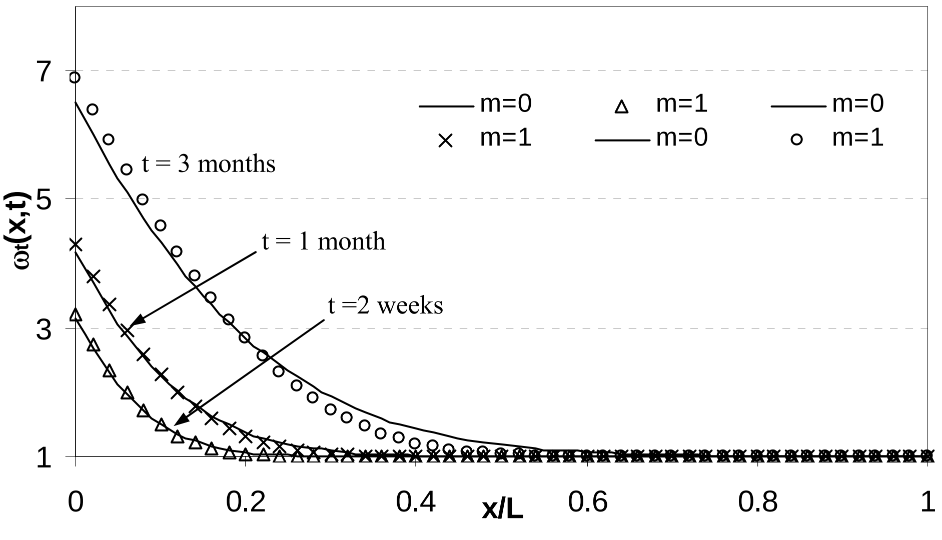

Figure 39. Thermoelastic Induced Normalized Net Width for Various Times and Degrees of Leak-Off. Solid: Impermeable; Symbols: Permeable.

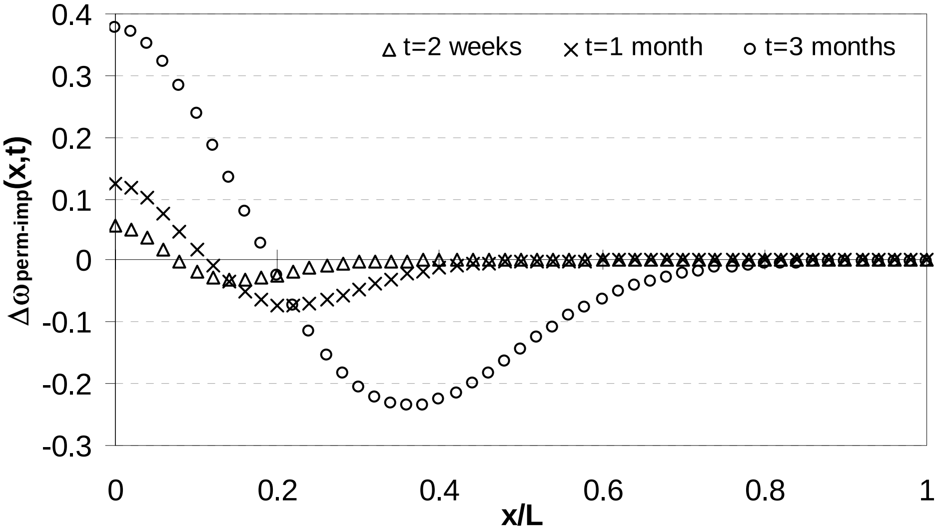

Figure 40 Difference between the Thermoelastic Induced Normalized Width for Permeable (m = 1) and Impermeable (m = 0) Cases at Various Times.

Figure 41 clearly indicates a difference in the resulting pressure distributions. This is further illustrated in Figure 42 where the permeable case has been subtracted from the impermeable case. The pressure gradients near the injection point have been greatly reduced because the same amount of fluid is passing through a larger conduit. Near the extraction point where the thermoelastic effects are not evident, the plot mirrors Figure 33. As a result of these effects at the injection and extraction point, the greatest pressure gradient is at the central section of the fracture trace for the permeable case. This is not the case for the impermeable case where there are no leak-off induced effects. As a result the greatest pressure gradient is near the extraction point.

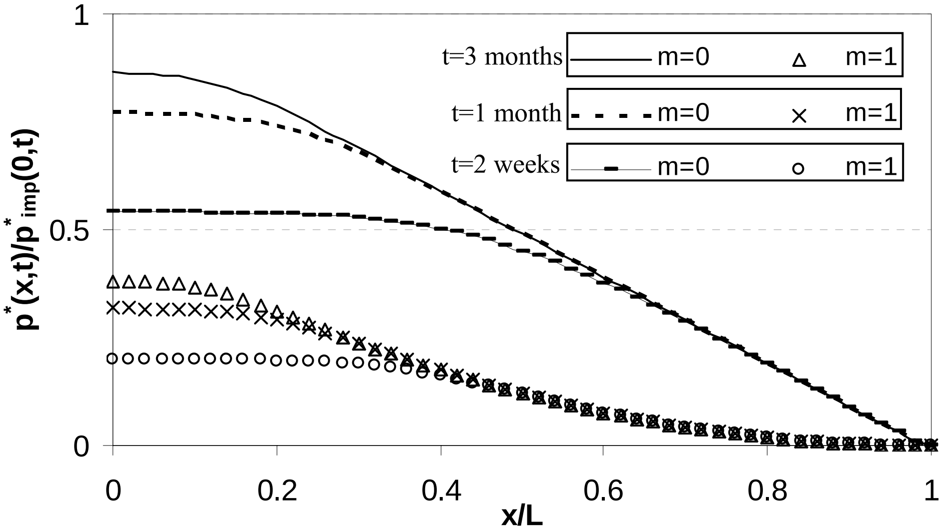

Figure 41. Normalized Induced Pressure in Fracture from Thermoelastic Effects for Different Times and Degrees of Leak-Off. Lines: Impermeable; Symbols: Permeable.

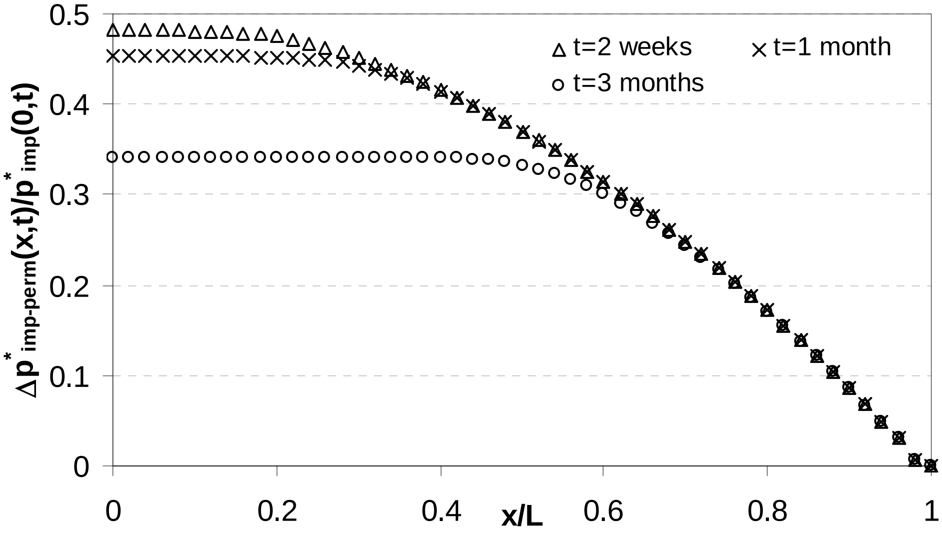

Figure 42. Difference between Normalized Induced Pressures for Thermoelastic Impermeable and Permeable Cases at Various Times.

Combined Thermoelastic and Poroelastic Effects

As already alluded to in Chapter IV, the principle of superposition may be applied to further investigate the combined effects of the thermo- and poroelastic loads on fracture aperture variation, and the resulting pressure distribution. The same parameters (*L* = 1000 m and Table 6) will be applied, except that an injection rate of 1E-4 m^2/s is used to enhance the poroelastic effects (see Figure 32 and 34). In doing this it is assumed the pressure and temperature fields in the rock are not coupled.

Figures 43 and 44 are obtained by adding the poroelastic effects to Figures 39 and 41, respectively. Note “t” implies only thermoelastic effects ($m = 1$ in this example), where as “tp” implies combined thermo- and poroelastic effects ($m = 1$ also). When only Figure 43 is considered, one could conclude that the poroelastic effects have a negligible effect because the width has only contracted a small amount relative to the thermoelastic induced width opening. However, Figure 44 shows that is not the case, and the pressure has been increased relative to the thermoelastic induced pressure by roughly 11% after two weeks, 16% after 1 month, and 24% after 3 months as a result of the rock expansion and poroelastic aperture reduction. The implication of this is that almost negligible changes in the fracture aperture can still result in non-negligible changes in the pressure at the inlet. This is even more apparent in Figure 45 where the differences between the normalized pressure for combined thermoelastic and poroelastic case and thermoelastic case are plotted. At early times the difference is only observed near the inlet. However as time increases the differences are observed at greater distances from the inlet, because of the thermoelastic effect perturbs the width further along the fracture trace. Also observed is that the largest deviation occurs at 1 month and not 3 months. The reason for this is that poroelastic effects have a more significant effect earlier and thermoelastic effects evolve slowly. Indeed, with increased time the thermoelastic effects will dominate as already illustrated by comparing Figures 31 and 35.

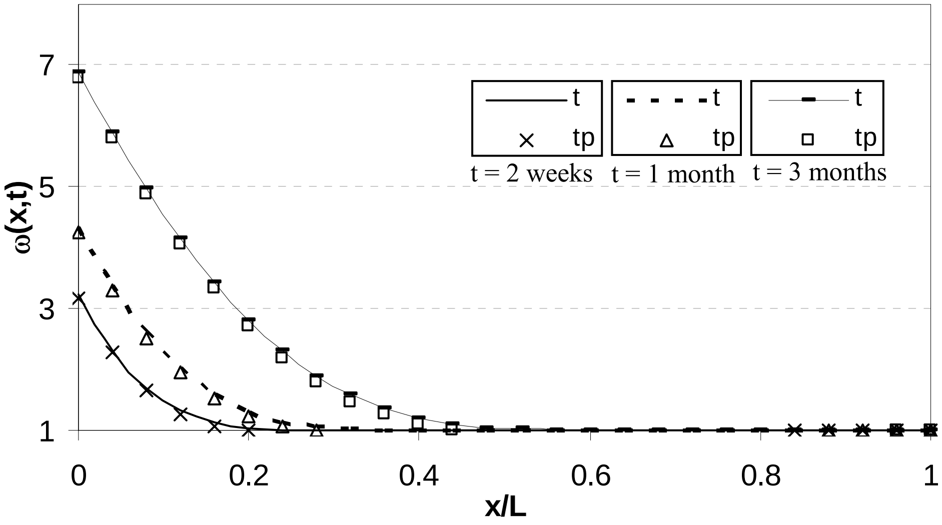

Figure 43. Combined Thermo- and Poroelastic and Thermoelastic Normalized Net Width at Various Times for *m* = 1. Lines: Thermoelastic; Symbols: Thermo- and Poroelastic.

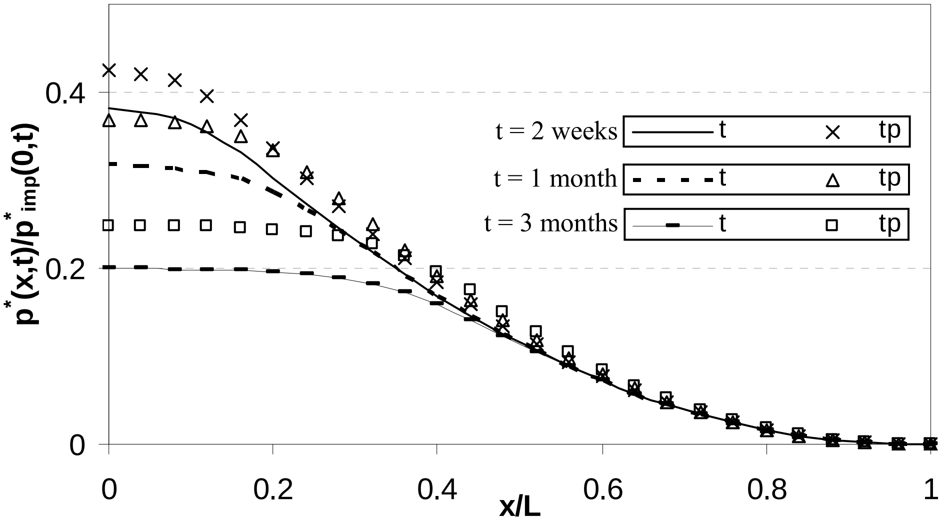

Figure 44. Normalized Induced Pressure in Fracture from Combined Thermo- and Poroelastic Effects and Thermoelastic Effects at Various Times for *m* = 1. Lines: Thermoelastic; Symbols: Thermo- and Poroelastic.

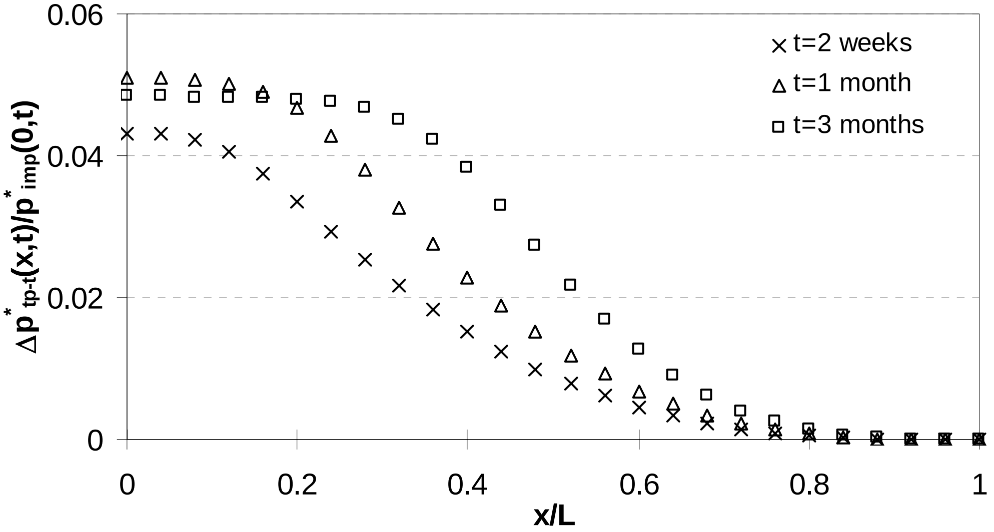

Figure 45. Difference between Normalized Induced Pressure for Combined Thermo- and Poroelastic Case and Thermoelastic Case at Various Times for *m* = 1.

CHAPTER VI

MECHANICAL EFFECTS OF WATER INJECTION INTO AN INFINITE RADIAL FRACTURE

In this chapter the derived expressions from Chapter IV for the induced effects of injection into an infinite radial fracture are applied. As already shown in Chapter IV only the *impermeable* case will be addressed as because it was found a constant leak-off solution created negligible changes. Furthermore hydraulic pressures needed to induced slip on a joint will not be considered, because as shown in Chapter V the thermoelastic induced effects dominate EGS permeability enhancement.

Thermoelastic Effects

First, it is of interest to investigate the time dependent opening at the injection point. This is illustrated in Figure 46 and uses the parameters from Table 6. The curve is same as the $m = 0$ curve in Figure 35. Comparison of (86) and (107) predicts this at the inlet. Initially the fracture width increase with respect to time is initially large, and decreases with increasing time.

The effects of injection rate on the thermoelastic fracture width are shown in Figure 47 after one month of injection. For this example, a large fracture radius of 500 m was chosen in order to satisfy the no flow boundary condition (91). The curves are different from Figure 37. In that near the injection point the induced width changes do not drop as steeply as in Figure 37. This is a direct result of radial varied flow equation (87). Near the injection point the fluid velocity is extremely high, and therefore the advective heat transport in the fracture is also high. However, as the radial distance increases the fluid velocity drops rapidly. The result is the induced thermoelastic width changes also rapidly decreases. This was also observed in the permeable cases of the line fracture, where the induced width changes dropped more rapidly than the impermeable cases as a result of leak-off and decreased fluid velocity.

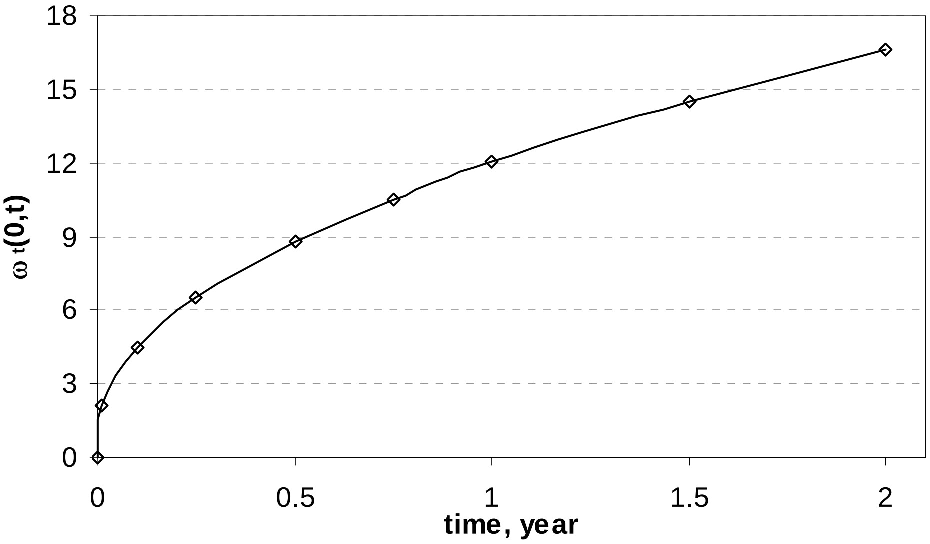

Figure 46. Time Dependent Thermoelastic Induced Normalized Net Width at Inlet.

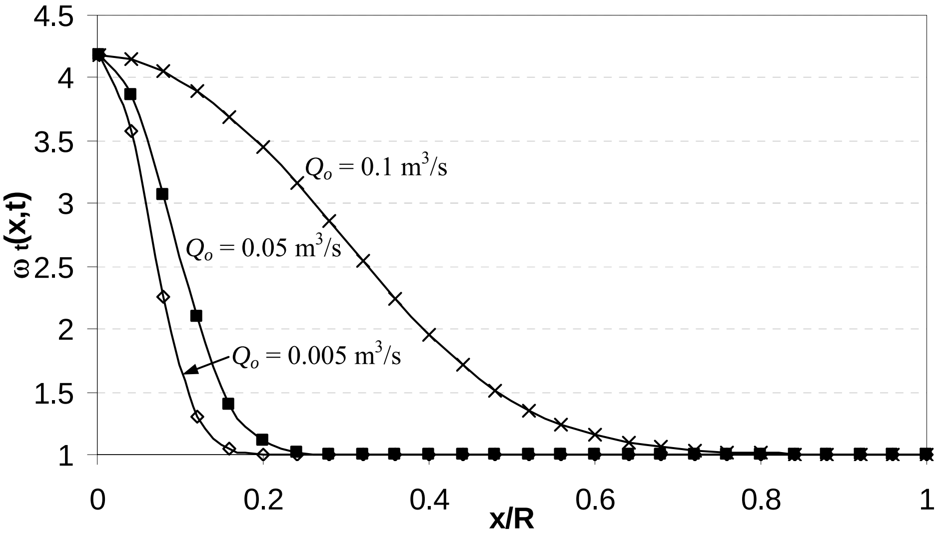

Figure 47. Thermoelastic Induced Normalized Net Fracture Width for Various Injection Rates after 1 month of Injection.

To examine the thermoelastic effects on the width change and pressure distribution with respect to time we will again assume a large fracture width of 500 m, and use a typical injection rate of 0.01 m^3/s (see e.g. Mossop and Segall, in-press) along with the appropriate parameters from Table 6. The normalized induced thermoelastic width changes are shown in Figure 48. The results are similar to Figure 39. However, the influence of the radial dropping flow rate is apparent. At points near the injection point the induced width change does not drop extensively with respect to distance as a result of the high fluid velocity. Away from the injection point this is not the case and the induced width changes drop rapidly due to decreased fluid velocity.

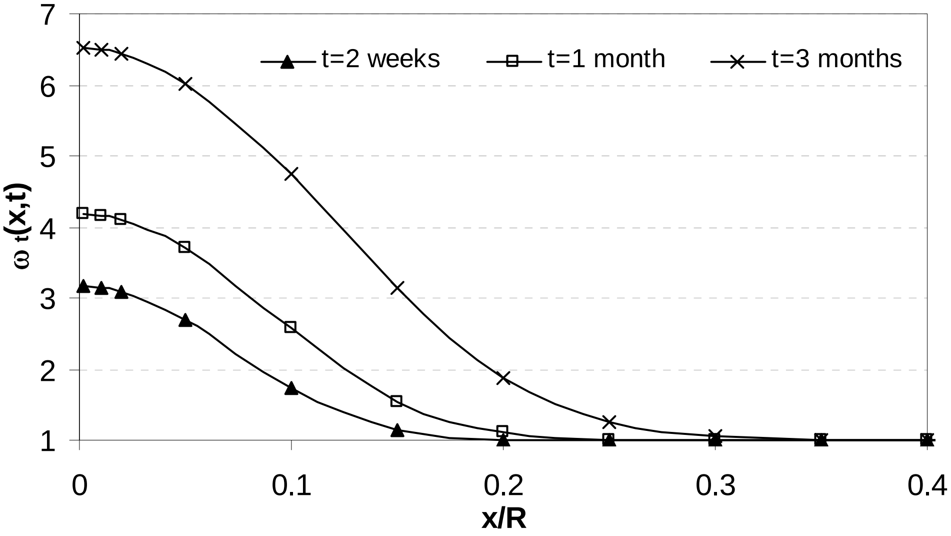

Figure 48. Thermoelastic Induced Normalized Net Fracture Width Change for Various Times.

In Figure 49 the corresponding normalized pressure distribution to Figure 48 has been plotted. It has been normalized to the isothermal injection pressure at r = 1 meter ($p^*_{imp}(1,t)$ = 0.11 MPa), because at r = 0 the injection rate is ∞ (see Eqn. 87 and 88). First, it is readily observed that the pressure distribution is logarithmic as predicted by (100). We also realized that the induced fracture width changes have significantly altered the pressure distribution around the injection point. Beyond the temperature perturbation the pressure is the isothermal induced pressure. In Figure 50 we have focused just on the areas where the induced pressure has been changed as a result of the thermoelastic effects. Near the injection point at early times there is still is small sign of a logarithmic pressure drop, which is a result of the radial varied flow. However this is not the case with increased time. The "3 months" curve in Figure 50 shows there is nearly no pressure gradient because of the large width increase. These results are similar to Figure 41. To further investigate the pressure decrease resulting from the fracture width opening, the normalized differences between the isothermal pressure distribution and the thermoelastic induced pressure distribution is plotted in Figure 51. It is observed the induced pressure difference as a result of the width increase drops with increasing radial distance. This is due to the decrease in the flow rate. It can therefore be concluded that as a result of the radial varied flow the thermoelastic effects on the fracture width and induced pressure are centralized to around the injection point.

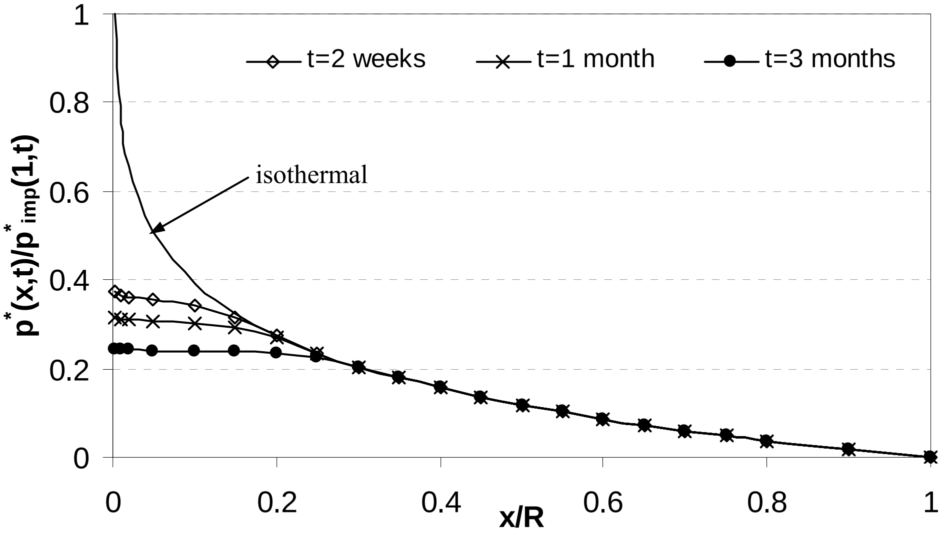

Figure 49. Normalized Induced Pressure in Fracture from Thermoelastic Effects for Various Times.

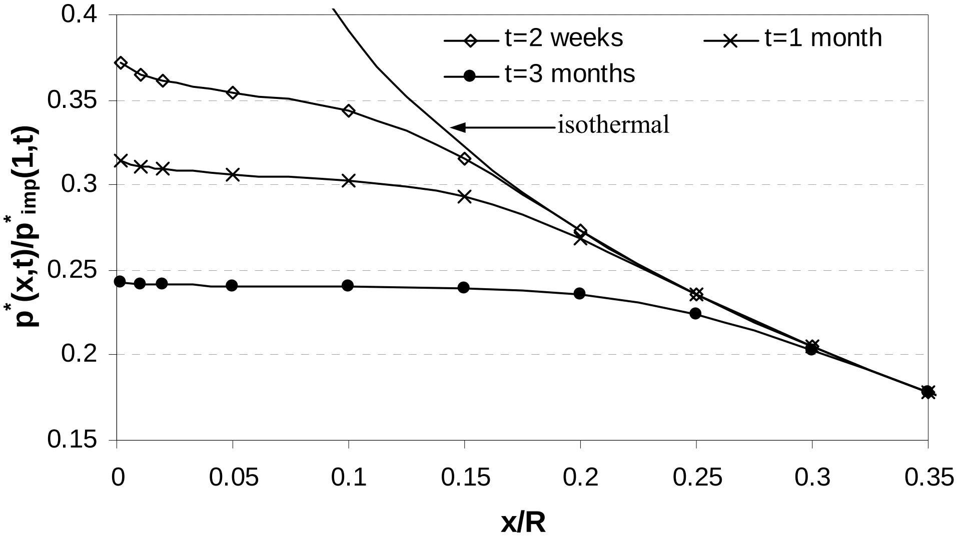

Figure 50. Zone of the Induced Normalized Pressure Changes Resulting from Thermoelastic Effects.

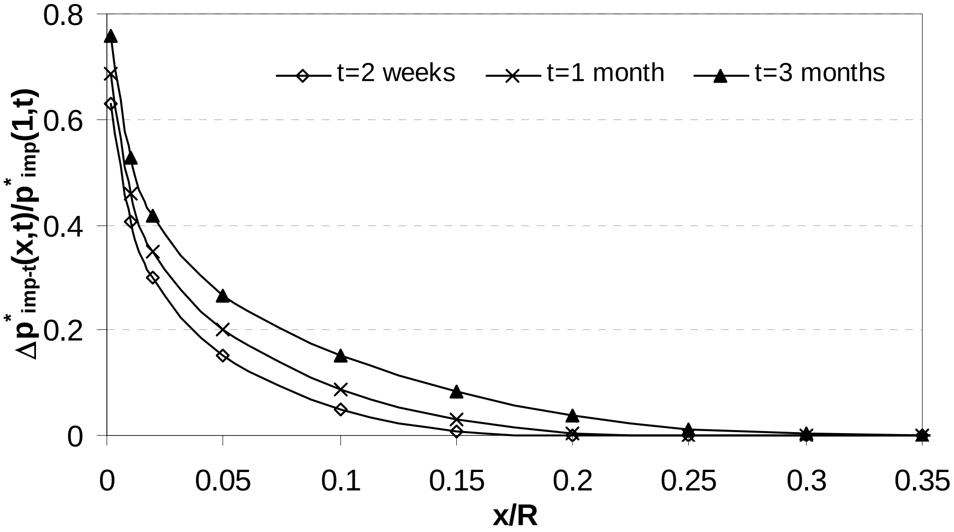

Figure 51. Normalized Induced Pressure Difference in Fracture between Isothermal and Thermoelastic Case for Various Times.

CHAPTER VII

MECHANICAL EFFECTS OF WATER INJECTION INTO A JOINT

In this chapter the model for injection into a joint derived in Chapter IV is applied to investigate the effects of fluid/solid coupling which was ignored in Chapters V and VI. The model is verified using an analytic solution and a sensitivity analysis is conducted on relevant variables. Then, the model is applied to examples including high and low injection rates including the induced elastic, poroelastic, and thermoelastic effects.

Model Validation and Sensitivity Analysis

To verify the model it will be compared to the analytic solution of a uniformly pressurized crack ($q_o = 0$), which was derived by Sneddon (1946) and given as:

$$\omega(\xi) = 1 + 4\overline{P}_{net}\sqrt{1-\xi^2} \tag{129}$$

Comparison of the model with (129) showed a % error of 0.1-0.6, and will be further elucidated on in the model results.

Before applying the model to the east flank of the Coso EGS it is of interest to investigate how the input parameters effect the model; namely q_o, L, and p_{net}. This is shown in Figures 52 and 53. Figure 52 is a plot of (129) for various p_{net} values. The normalized joint width is at the injection point ($x = 0$). We see as p_{net} in the joint is increased along with the joint length the aperture significantly increases at the center of the joint. This is expected since increasing the pressure will induce more displacement. This is further justified by Figure 53 where the effect of the injection rate on the relative width opening at the injection point (ω' is opening when $q_o = 0$) for various p_{net} values is shown. It is readily observed the greater the injection rate and the less the p_{net} value, the effects of injection are more pronounced. Conversely, when a high p_{net} exists and the injection rate is low, then the effects of injection are almost negligible. For our purposes it is of interest to investigate the effects of injection. Therefore a higher injection rate should be applied to a low p_{net} value. Finally, it should also be mentioned that extremely long joint lengths and high injection rates result in a non convergent solution because of the resulting large differences between γ and $\overline{P}_{net}$ (see Eqn. 112). That is why extremely high injection rates and long joint lengths will not be applied in this chapter.

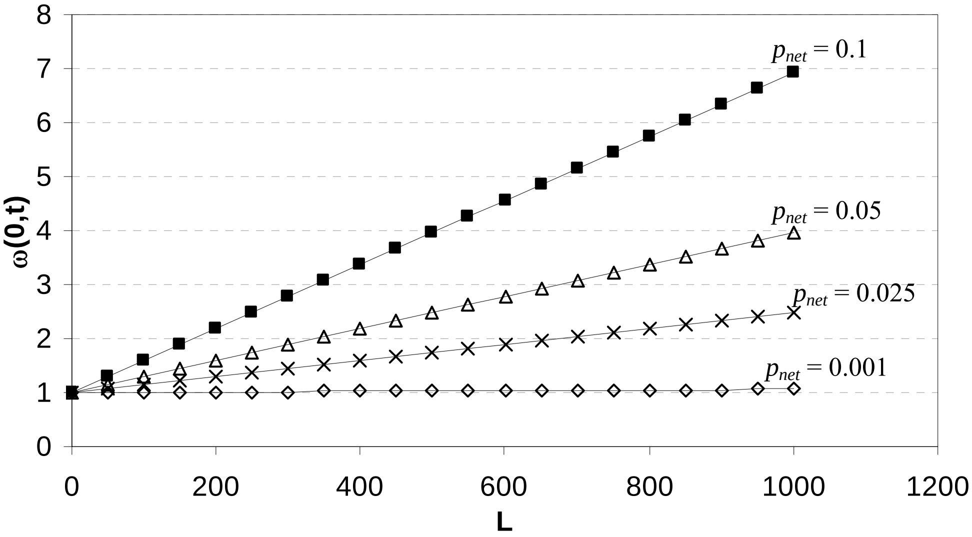

Figure 52. Relationship between Net Pressure (in MPa) in Fracture and Width Opening at Injection Point.

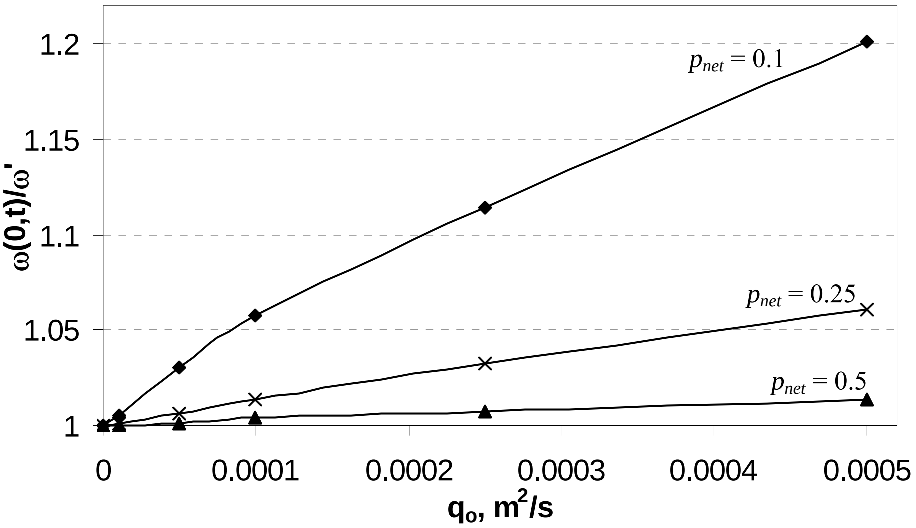

Figure 53. Influence of q_o on Relative Width Opening at Injection Point for Various p_{net} Values (in MPa).

Influence of Fluid Leak-Off On Joint Width and Pressure

Isothermal Poroelastic Effects

First, it is of interest to investigate the how the opening at the injection point is effected by the injection rate for conditions of leak-off. In light of the previous section, a small p_{net} value of 0.01 MPa is chosen, along with a shorter joint length of L = 200 m. Figure 54 shows the relationship between the opening and the injection rate for various degrees of leak-off. First, we realize the general trend is the same as the time dependent opening of the line fracture at the injection point (see Figure 31 or 35). It is expected that the opening will decrease with more leak-off because less pressure is exerted on the joint surface. Also, at low injection rates the differences in the joint width for various degrees of leak-off is not as noticeable as for higher injection rates. To illustrate this consider q_o = 0.0001 m^2/s in Figure 54. When m = 1 the same opening is attained for the m = 0 case with q_o = 0.000036 m^2/s, and with m = 0.5 the same opening is attained with q_o = 0.00005 m^2/s. Finally, it should be noted when $q_o = 0$ the opening is 1.1197, which is extremely close to the opening obtained by the analytic solution (129) of 1.1185.

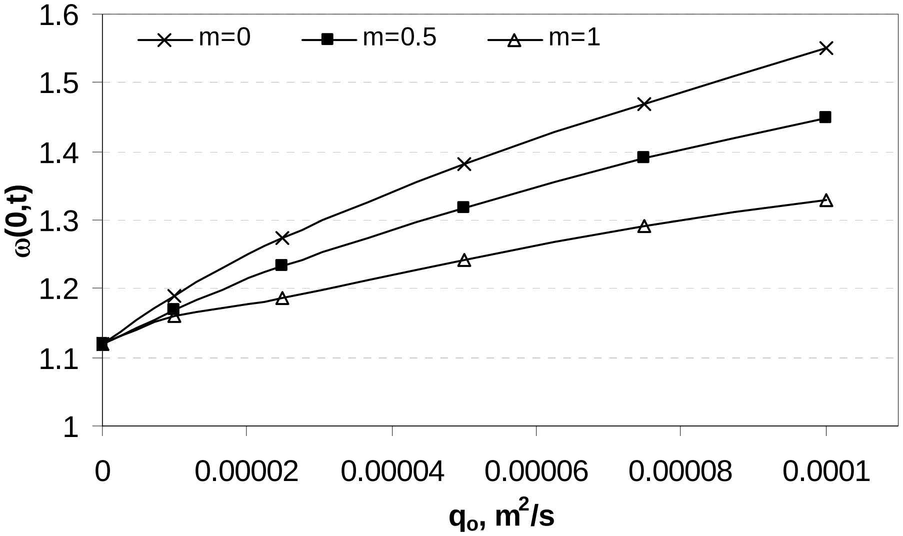

Figure 54. Relationship between the Normalized Joint Opening at the Injection Point and Injection Rate.

Now the spatial relationship under various degrees of leak-off will be looked at. We will consider $L = 200$ m, $p_{net} = 0.01$ MPa, a high injection rate of $q_o = 0.0002$ m^2/s, and the relevant parameters from Table 6. This high injection rate is used to exaggerate the poroelastic effects, and the fluid/solid coupling. The normalized net joint width is plotted in Figure 55 for the elastic case and poroelastic case with various degrees of leak-off after 3 months of injection. Indeed the poroelastic induced width changes have contracted the joint. However we note an interesting effect as a result of the fluid/solid coupling. In that the greatest width differences between the elastic and poroelastic cases occur near the central section of the joint. This effect is caused by the fluid/solid coupling, and is why this effect was not observed for the injection/extraction model into a line fracture in Chapter V. At the inlet, $\Delta p^*_{poro}(x,0,t)$ is reduced as a result of the fluid/solid coupling increasing the joint width (this will become more apparent when the pressure in the joint is considered). However, as a result of leak-off the fluid/solid coupling effect is decreased away from the inlet (less fluid in joint to exert pressure on the joint surface). As a result, $\Delta p^{*}_{poro}(x,0,t)$ increases and the poroelastic induced width contraction is enhanced. We note as a result of the unchanging width boundary condition at $x = L$, the curves converge to $\omega_p(L) = 1$.

To illustrate the effect observed in Figure 56 for different times, the poroelastic induced joint width has been subtracted from the elastic joint width (elastic curves in Figure 55) for various times and degrees of leak-off. It is readily observed that the increased contraction near the central section of the joint is enhanced with time. This would be expected because the elastic induced joint width is steady state; while the poroelastic induced joint width contraction will increase with time (see Eqn. 67).

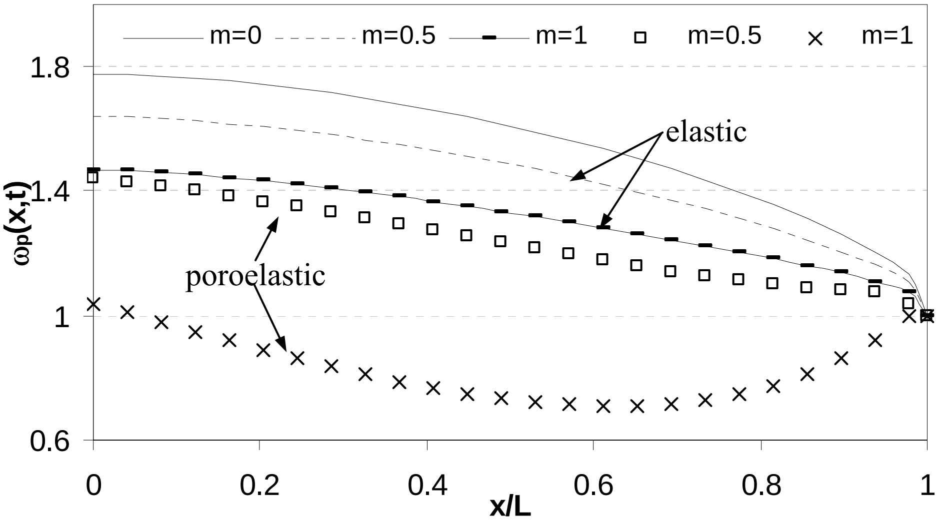

Figure 55. Elastic and Poroelastic Induced Joint Width for Various Degrees of Leak-Off after 3 Months of Injection. Elastic: Lines; Poroelastic: Symbols.

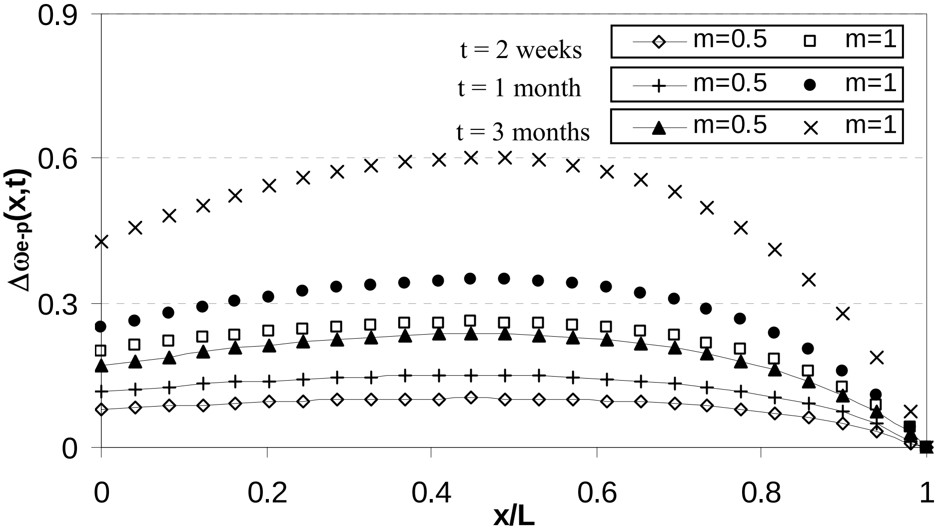

Figure 56. Differences between Elastic and Poroelastic Joint Widths for Various Times.

Now it is of interest to investigate the influence of poroelastic effects on the pressure distribution in the joint. Figure 57 shows the resulting pressure distribution normalized with respect to the isothermal impermeable injection pressure ($p^*_{imp}(0,t)$ = 7.1 MPa) from Figure 55 for the elastic case and the poroelastic case after 3 months of injection. The reason for the high $p^*_{imp}(0,t)$ value is a result of no fluid extraction, which allows for the pressure in the joint to increase till equilibrium is reached (similarly to blowing up a balloon).

Figure 57 illustrates as a result of the poroelastic effects contracting the width; the pressure at the inlet has increased the pressure in the joint. The reasons for the significant increases for the m = 1 case is a result of the high injection rate contracting the width (see Figure 55). Near the joint tip the pressure distributions are nearly identical because the difference between the reservoir and the joint pressure is small resulting in little poroelastic induced effects. Furthermore, it is observed the elastic case of m = 0.5 is nearly linear (similar to impermeable line fracture solution). The combined effect of fluid loss and fluid/solid coupling cause this because the fluid/solid coupling increases the pressure gradient near the joint tip, while the fluid loss decreases the pressure gradient. The result is a near linear distribution

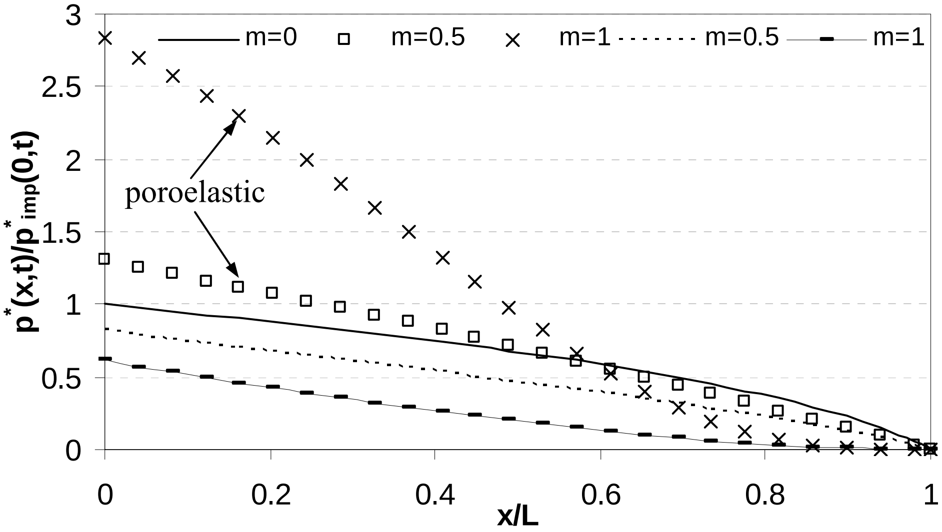

Figure 57. Normalized Induced Pressure Distribution for Elastic and Poroelastic Case after 3 Months of Injection.

To further illustrate the differences in the pressure caused by leak-off consider Figure 58. In Figure 58 the permeable elastic and poroelastic normalized pressures are subtracted from the impermeable normalized pressure. It is observed the greatest difference in pressure for the elastic case is at the central section of the joint, which readily shows why the greatest width changes were observed in the central section of the joint when including poroelastic effects (see Eqn. 66 and 67). The reason for this behavior is a result of the fluid/solid coupling reducing the poroelastic induced pressure $\Delta p^{*}_{poro}(x,0,t)$ at the inlet. That is why this was not observed in Figure 34 for the elastic case. We realize that the poroelastic pressure distribution in the joint has significantly increased as a result of the fracture width contraction observed in Figure 55.

Finally it is noted that similarly to Figure 34, near the joint tip the poroelastic and elastic curves are nearly the same as a result of the poroelastic induced effect becoming negligible.

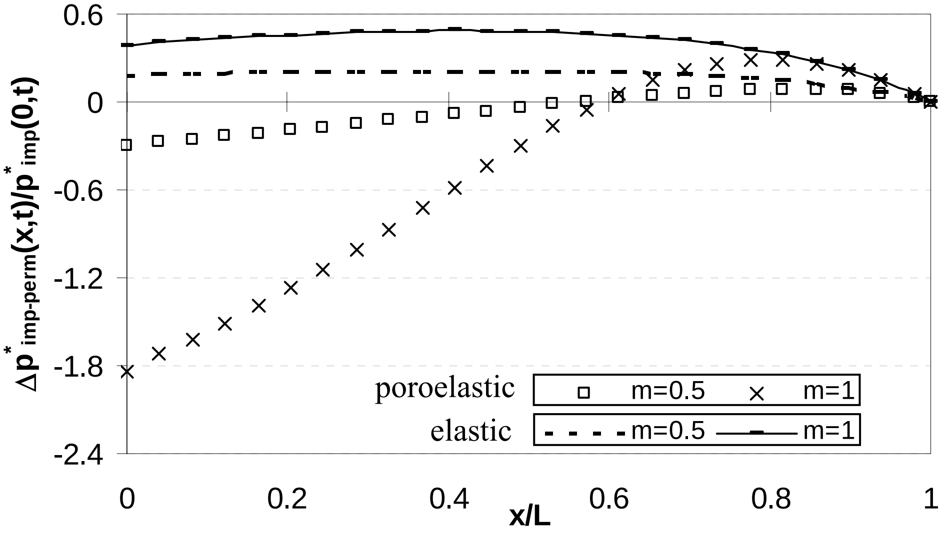

Figure 58. Difference between Impermeable and Permeable Normalized Pressures for Various Degrees of Leak-Off after 3 Months of Injection. Lines: Elastic; Symbols: Poroelastic.

Thermoelastic Effects

To include the thermoelastic effects the injection rate will be greatly reduced to allow for a longer time. This is done to satisfy the boundary condition $\omega(L) = 1$. Using the injection rate from the previous example results in a simulation time of only 10 days, because at 10 days $\omega(L) \neq 1$ for the $m = 0$ case. We will use $L = 200$ m, $p_{net} = 0.01$ MPa, an injection rate of 0.00005 m^2/s and the parameters in Table 6. First the elastic effects will be considered. The elastic width profile is plotted in Figure 59 for various degrees of leak-off. Also included is the case for a uniformly pressurized crack. The "DD" plot represents the DD model, and the "Sneddon" plot denotes the analytic solution. The match is quite good; there is a small (0.1-0.6%) overestimation, which is a result of the constant displacement assumption for each node (Crouch and Starfield, 1983).

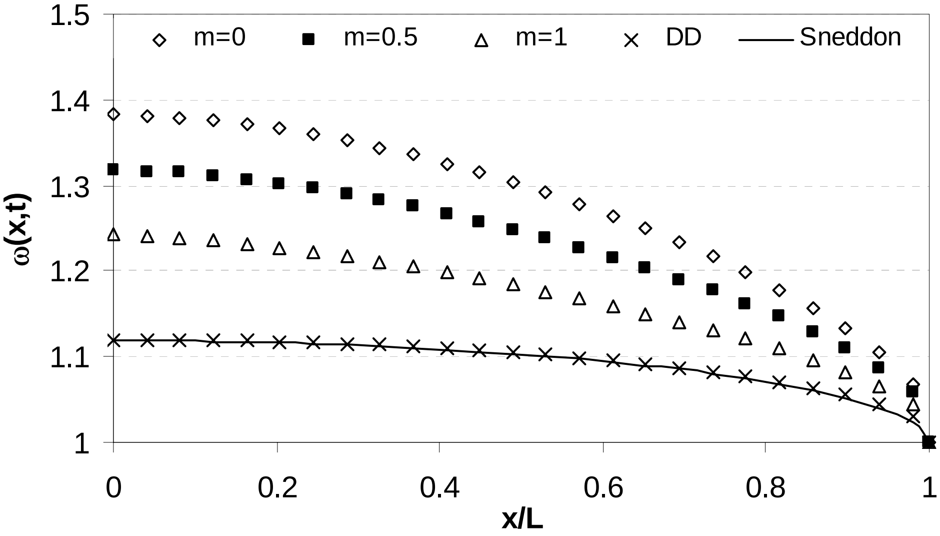

Figure 59. Normalized Elastic Width Opening for Various Degrees of Leak-Off.

Figures 60-63 illustrate the effect of leak-off and the thermoelastic effects of injection into a joint. These figures correspond to Figures 39-42 in Chapter V for the injection/extraction from a line fracture model. First let us consider Figure 60 which shows the normalized thermoelastic width for injection into a joint. It is readily observed near the inlet the differences between the permeable (m = 1) and impermeable case are negligible. However near the end of the respective temperature perturbations the differences are not negligible. This is illustrated in Figure 61 where the differences between the impermeable and permeable joint widths have been plotted. It can be observed that at early times the joint width for the impermeable case is larger (not observed in the line fracture model) at the inlet. This is due to the slow effects of the thermoelastic effects, and immediate effects of the fluid/solid coupling. With increased time, the permeable case will have a greater joint width at the inlet, because of the enhanced thermoelastic effect caused by leak-off. Furthermore it is noted the greatest difference between the curves occurs at some distance away from the inlet. This distance increases with time. The reason for this is that the thermoelastic effect perturbs further along the joint trace for the impermeable case because the fluid velocity is not retarded by leak-off. Figures 60 and 61 also show that near the end of the joint ($x = L$) there are no thermoelastic induced effects; this satisfies the boundary condition of $\omega(L) = 1$. The simulation time can be expanded by either reducing the injection rate, increasing the joint length, or a combination of both. However, it is should be stressed again that increases in the joint length can result in a non-convergent solution.

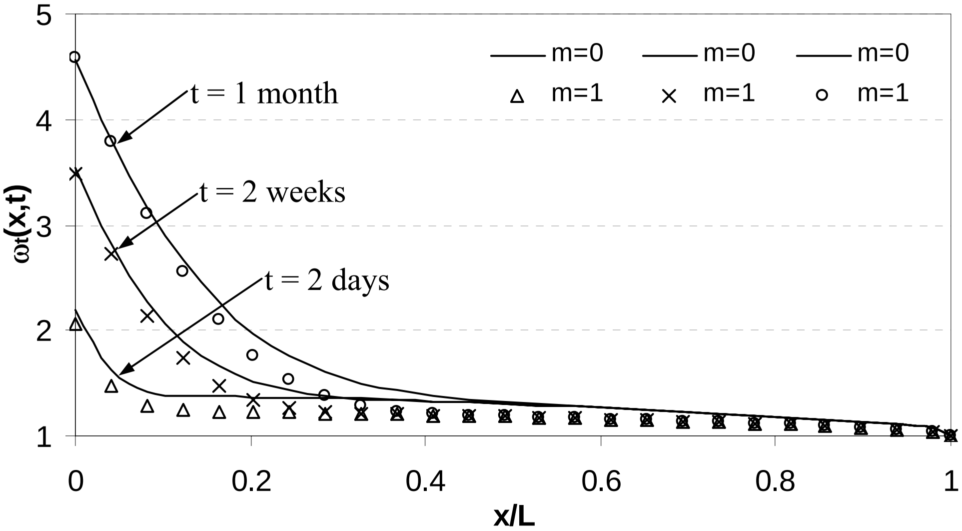

Figure 60. Thermoelastic Induced Normalized Joint Width for Various Times and Degrees of Leak-Off. Solid: Impermeable; Symbols: Permeable.

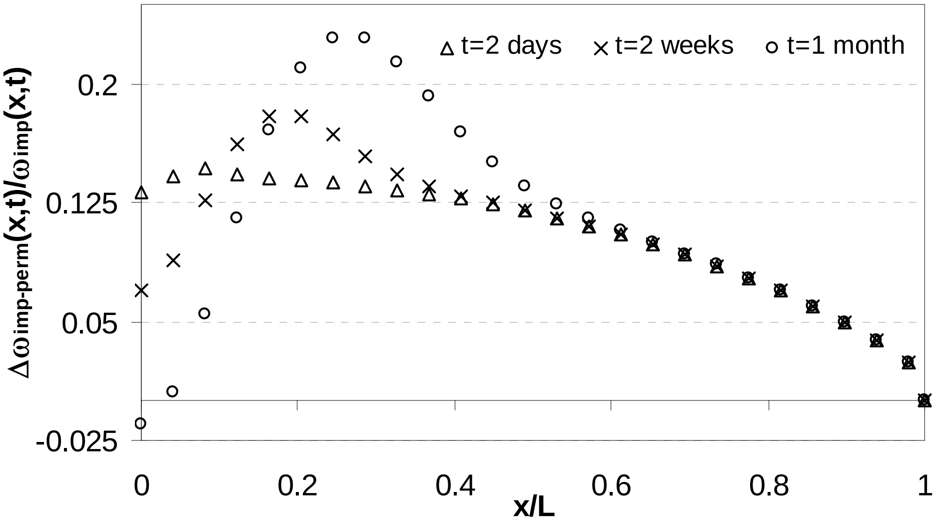

Figure 61. Difference between the Thermoelastic Induced Normalized Joint Width for Impermeable and Permeable (*m* = 1) Case at Various Times.

The pressure distribution corresponding to Figure 60 is plotted in Figure 62 (*m* = 0.5 case is now also included), which show as a result of leak-off the pressure distribution has significantly changed. Indeed, the pressure has been reduced at the inlet in response to increased aperture caused by the thermoelastic effects shown in Figure 60. Furthermore, it is observed that the suite of permeable ($m \neq 0$) curves become identical closer to the inlet than the suite of $m = 0$ curves. This is a result of temperature perturbation extending further into the joint, because for the $m = 0$ case the advective heat transport is not retarded as it is for the $m \neq 0$ cases due to fluid leak-off.

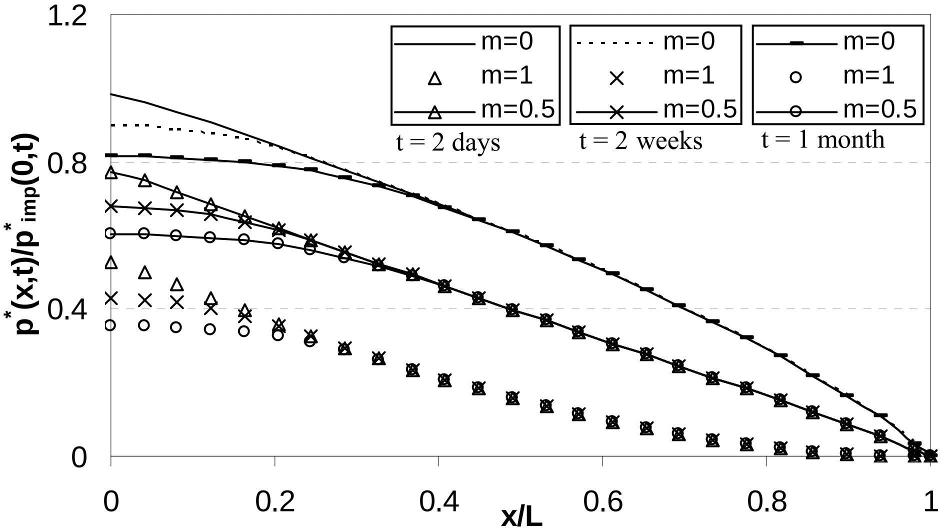

Figure 62. Normalized Induced Pressure in Joint from Thermoelastic Effects for Different Times and Degrees Leak-Off. Lines: Impermeable; Symbols: Permeable.

The amount of pressure reduction in the joint as a result of leak-off is illustrated in Figure 63 where the difference between the normalized impermeable and permeable thermoelastic pressure distributions is plotted. Indeed, the suites of curves for various leak-off values are similar. This is because the thermoelastic effects are similar in the impermeable and permeable cases (see Figure 60 and 61). Note that the differences in pressure between the impermeable and permeable cases slowly decrease with time. This is a result of the thermoelastic effects dominating that associated with leak-off with increasing time.

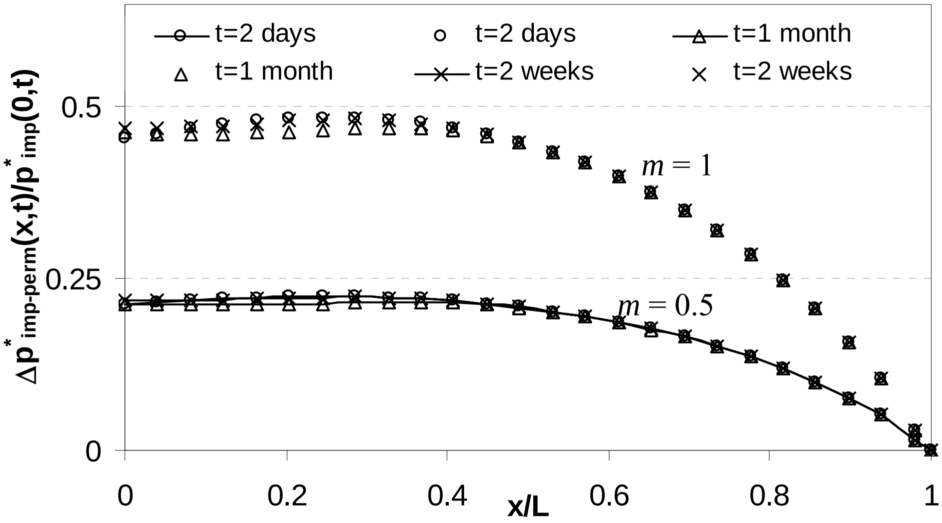

Figure 63. Difference between Impermeable Thermoelastic Pressure and Permeable Thermoelastic Pressure in Joint for Various Times and Degrees of Leak-Off.

Combined Thermoelastic and Poroelastic Effects

It is now of interest to include the poroelastic effects into the example from the *Thermoelastic Effects* section of this chapter. The appropriate parameters are L = 200 m, p_{net} = 0.01 MPa, an injection rate of 0.00005 m^2/s and the values in Table 6. Figure 64 illustrates a plot for the case of m = 1 comparing the induced joint width for the combined thermo- and poroelastic effects, and thermoelastic effects for various times. At early times the differences in the width are negligible, and as time increases we see only a small decrease in the width profile as a result of the poroelastic effects contracting the width, which was also observed in Figure 43. As shown in Figure 65 though, the normalized pressure profiles are indeed different. At the injection point the induced combined thermo- and poroelastic pressure has increased relative to the thermoelastic induced pressure by a 9%, 22%, and 37% after 2 days, 2 weeks, and 1 month respectively. This increase was also observed in Figure 44, and is a result of the poroelastic effects contracting the joint, and the thermoelastic effects expanding the joint. However, as shown in Figure 66, the total differences in the normalized pressure is decreasing with increasing time as a result of the thermoelastic effects becoming dominant, and reducing the pressure in the joint. Finally, it is realized near the tip of the joint the curves are similar to the elastic curves, because the induced thermo- and poroelastic effects are small.

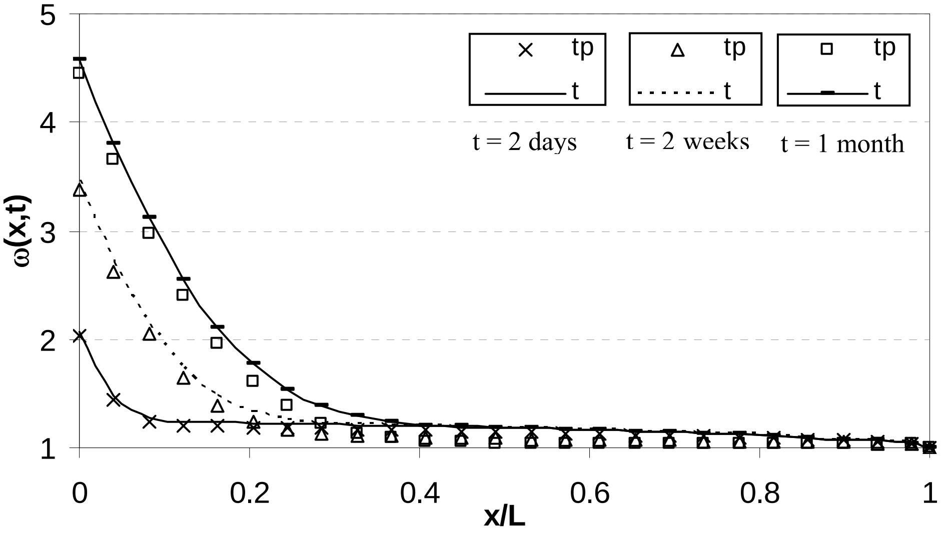

Figure 64. Combined Thermo- and Poroelastic and Thermoelastic Normalized Joint Width for Various Times when *m* = 1. Lines: Thermoelastic; Symbols: Thermo- and Poroelastic.

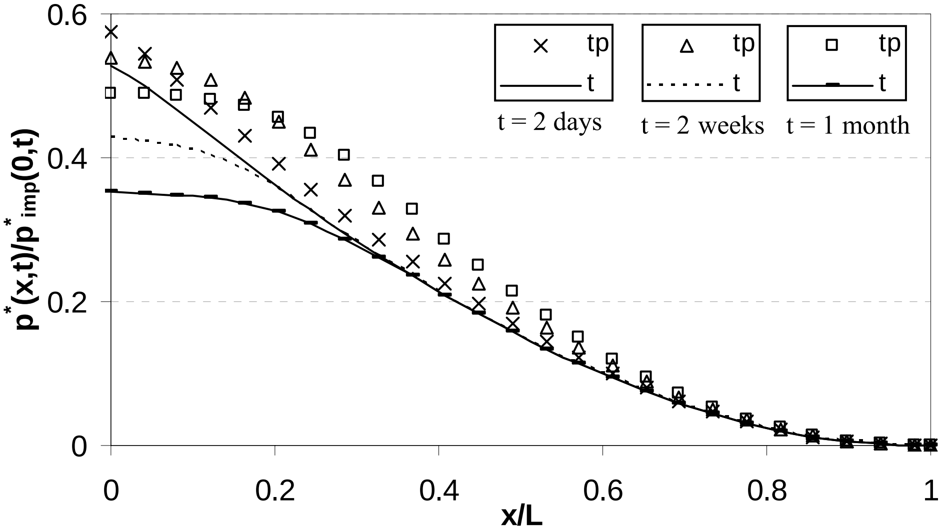

Figure 65. Normalized Induced Pressure in Joint from Combined Thermo- and Poroelastic Effects and Thermoelastic Effects for Various Times when *m* = 1. Lines: Thermoelastic; Symbols: Thermo- and Poroelastic.

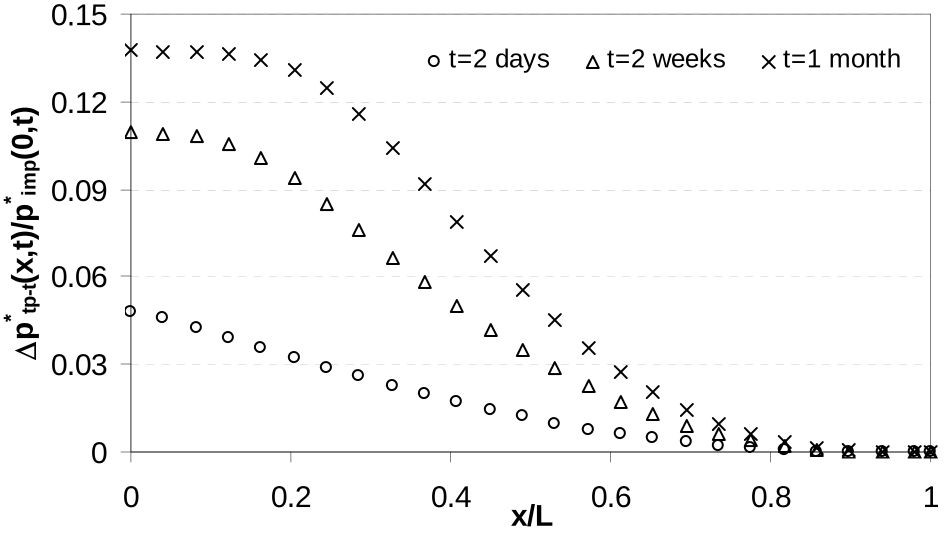

Figure 66. Difference between Normalized Induced Pressure in Joint for Combined Thermo- and Poroelastic Case and Thermoelastic Case at Various Times when *m* = 1.

At this point we will revisit the example from the *Isothermal Poroelastic Effects* section of this chapter, which had a high injection rate. The applicable parameters are L = 200 m, p_{net} = 0.01 MPa, q_o = 0.0002 m^2/s, and the values in Table 6. Figure 67 is a plot showing the time evolution of the joint width for the thermoelastic and combined thermoelastic and poroelastic effects for m = 1. Indeed as a result of the increased injection rate the width has increased more when compared to Figure 64. This is due to the fluid/solid coupling, and also the longer time enhancing the thermoelastic effects. We note the boundary condition of $\omega(L) = 1$ is still satisfied because at $x = L$ the injection rate is 0 (see Eqn. 57). In this example there is noticeable reduction in joint width from the poroelastic effects. As time increases the difference between the thermoelastic (t) and combined thermo and poroelastic (tp) curves becomes more pronounced. This is a result of the large poroelastic effects from the high injection rate. Although Figure 67 shows that the overall joint width is increasing showing the thermoelastic effects are in fact dominant.

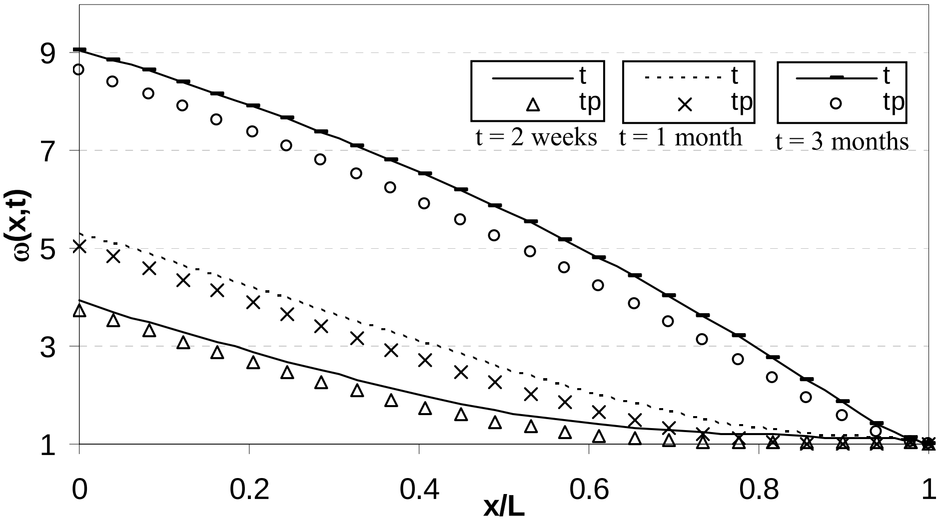

Figure 67. Combined Thermo- and Poroelastic and Thermoelastic Normalized Joint Width for Various Times when m = 1. Lines: Thermoelastic; Symbols: Thermo- and Poroelastic.

The corresponding normalized pressure distribution in the joint for the joint widths in Figure 67 is shown in Figure 68. It is evident that including the poroelastic effects significantly changes the pressure distribution in the joint. The increase in pressure for the combined thermo- and poroelastic effects relative to the thermoelastic effects is 54%, 67%, and 42% for 2 weeks, 1 month, and 3 months respectively. In Figure 68, the difference in the 3 months curves is not strongly evident because the pressure in the joint has been significantly reduced as a result of the increased width. The reason for the initial increase and the subsequent decrease between the thermoelastic case and combined poroelastic and thermoelastic case is the poroelastic contribution to the pressure distribution. This was not observed in the previous example of this section because the poroelastic effects were small as a result of the low injection rate and also smaller simulation time. Initially, at small times, the poroelastic pressure increases are more pronounced. Therefore, at early times the poroelastic effects increase the deviation between the thermoelastic case and combined poroelastic and thermoelastic case (from 54 to 67%), because of the slow response of the rock to the thermoelastic effects. Eventually, the thermoelastic effect will become dominant and result in the deviations between the thermoelastic case and combined poroelastic and thermoelastic case becoming smaller (hence the decrease from 67 to 42%). In light of these apparent deviations, the difference between the combined thermo- and poroelastic effects and thermoelastic pressure distributions are plotted in Figure 69. It is readily observed that the overall difference decreases to zero with increasing time, because at later times the thermoelastic effects will dominate the resulting pressure profile in the joint.

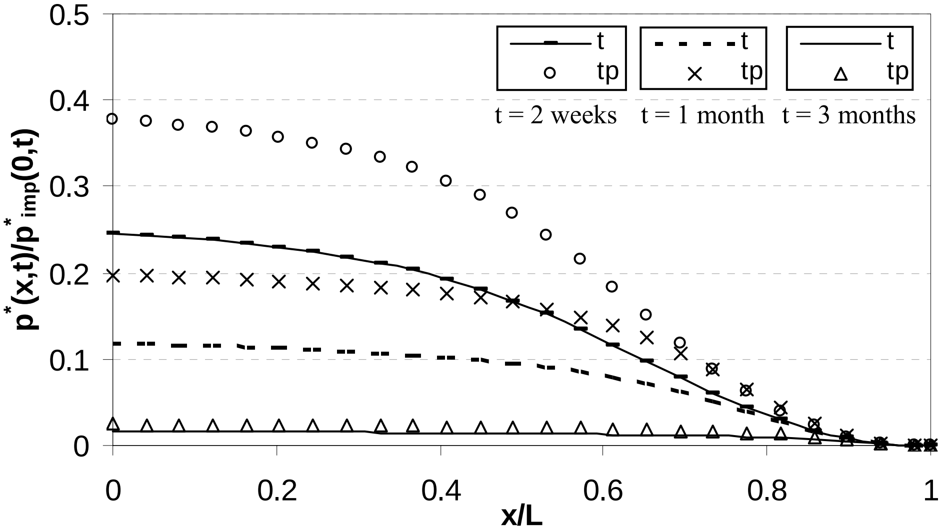

Figure 68. Normalized Induced Pressure in Joint from Combined Thermo- and Poroelastic Effects and Thermoelastic Effects for Various Times when *m* = 1. Lines: Thermoelastic; Symbols Thermo- and Poroelastic.

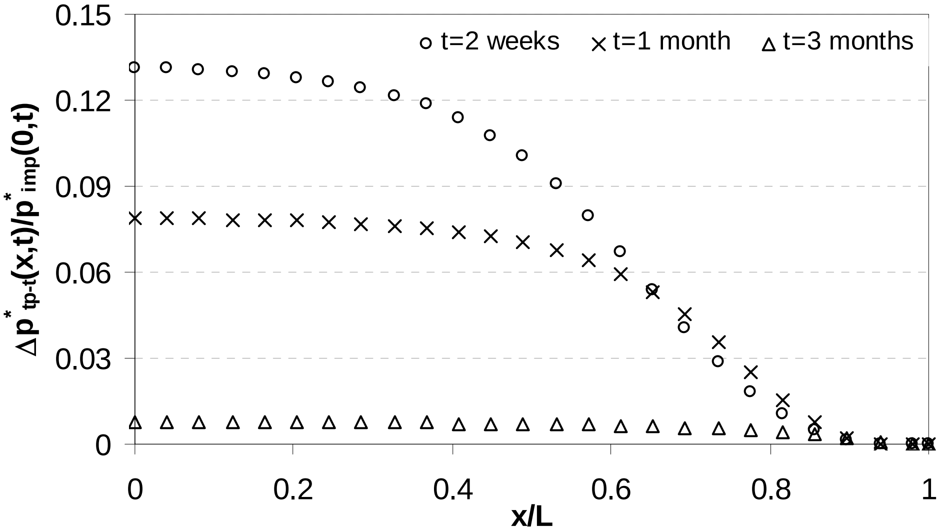

Figure 69. Difference between Normalized Induced Pressure in Joint for the Combined Thermo- and Poroelastic Case and the Thermoelastic Case at Various Times.

CHAPTER VIII

SUMMARY, CONCLUSIONS, AND FUTURE WORK

Certain reservoir geomechanics issues in the east flank of the Coso EGS have been addressed. First, a *lower bound* estimate of the S_{Hmax} was found utilizing a fracture mechanics analysis of drilling induced tensile fractures observed in well 38C-9 incorporating the influence of thermal stresses. The S_{Hmax} estimate was further constrained by comparison with other published values of S_{Hmax}, and a fracture propagation study. Only the lower range *lower bound* estimate resulted in no extensive fracture propagation. Based on this estimate, the stress regime at the east flank transition from $\sigma_1 = S_{Hmax}$ to $\sigma_1 = S_v$ with increasing depth. This characterization is consistent with the network of *fractures with significant aperture* (Sheridan and Hickman, 2004) in well 38C-9. The stress regime at the proposed injection depth corresponds to a normal faulting regime ($\sigma_1 = S_v$).

A linear and non-linear failure criterion was used to conduct a critical stress analysis on the network of *fractures with significant apertures*. In general, it was found that critically oriented ($\beta = \beta_{crit}$) joints having a friction angle less than 25º can be critically stressed at any depth. Joints with friction angles greater than 25º were found to be critically stressed in the S_{Hmax}-S_{hmin} plane only to a critical depth that is well above the proposed injection interval. This is because $S_{H\max}\big|_{z=0} \neq 0$ which results in the limiting stress ratio, R, in the S_{Hmax}-S_{hmin} plane becoming hyperbolically related to depth (see Eqn. 26 in Chapter III).

For joints with friction angles greater than 25° the pressure increase needed to induce slip (p_o^+) was found by using Terzaghi's definition of effective stress. Also, the corresponding injection rate needed to induce slip was calculated using a simplified injection/extraction model. The estimated injection rates appear to be high for most joint orientations. The orientation of joints most conducive to slip prior to jacking ($\theta_{q(\max)}$) was found to be a function only of the loading. In deviatoric loaded environments, like Coso, joints oriented near $\theta_{q(\max)}$ will readily slip relative to jacking.

Constraining whether $S_{h\min}\big|_{z=0} \neq 0$ can readily allow the above critical stress analysis to become more accurate. This will further constrain the stresses acting on the joint network. To accomplish this hydraulic fracturing tests or over-coring tests can be conducted at different depths allowing for best fit curves of S_{hmin} to be constructed (see e.g. Pine, 1983).

A simplified plane strain model was developed and used to assess the poroelastic and thermoelastic effects associated with water injection into a permeable deformable fracture. Three sub-models were applied: (i) injection/extraction into a line fracture, (ii) injection into an infinite radial fracture, (iii) injection into a finite joint. The sub-models (i) and (iii) were developed by considering the case of constant injection rate, constant leak-off, and obtaining analytical solutions for the fracture width based on one-dimensional heat transfer and fluid loss in the rock. Both poroelastic and thermoelastic effects were accounted for in the sub-model (i), and (iii). Sub-model (ii) represents an alternative geometry and was solved for the case of impermeable rock to allow analytical treatment.

The thermoelastic effects in all sub-models (i-iii) were found to increase the fracture or joint width at the inlet with increased time and leak-off (for sub-model i and iii) due to the increased heat flux. Increasing the injection rate extended the spatial extent the of the thermoelastic effects. The spatial extent of the perturbation was retarded by the effects of fluid loss reducing the fluid velocity. The thermoelastic effects were found to decrease the pressure in the fracture as a result of the increased fracture width providing a larger flow conduit. This effect was enhanced with increased time.

The poroelastic effects in models i and iii were found to decrease the fracture width at the inlet. This effect was enhanced with increased leak-off, time, and injection rate because the pressure difference between the reservoir and fracture was increased. As a result of the decrease in fracture width the pressure in the fracture increased. It was found even small contractions in the fracture width could result in non-negligible changes in the pressure at the inlet. However, with increased distance along the fracture or joint trace the poroelastic effects became negligible, because the pressure in the reservoir and fracture were approaching the same value.

The combined thermoelastic and poroelastic effects in models i and iii were compared with the thermoelastic effects to further investigate the relative importance of the poroelastic effects. It was found that at early times under high injection rates the poroelastic effects resulted in non-negligible changes in fracture and joint geometries and the resulting pressure distributions. Overall it was found with increased time the thermoelastic effects were dominant, which showed the *thermoelastic effect is the key* *component to fracture permeability enhancement*. However, poroelastic effects are also important and contribute to evolution of fracture geometry and the resulting pressure in the fracture or joint.

Sub-model (ii) showed the impermeable solution of the induced fracture width behaved similarly to the permeable sub-model (i) results, because in both cases the fluid velocity decreased with increased distance along the fracture. This effect was more pronounced in sub-model (ii) because of the hyperbolic reduction (i.e. $1/r$) in fluid velocity rather than the linear reduction in fluid velocity for the permeable case of sub-model (i). The results for sub-model (ii) showed the induced thermoelastic effects were centralized near the injection point. As a result of the thermoelastic effects around the inlet, the pressure distribution dropped in response to the increased aperture around the injection point.

The incorporation of fluid/solid coupling in sub-model (iii) increased the joint aperture resulting in a decrease in the pressure in the joint. This effect was enhanced for joints under a small net pressure (p_{net}) subject to high injection rates. It was also observed the poroelastic effects were more pronounced because of the increased pressure difference between the reservoir and the joint. As a result, a significant increase in the pressure distribution of the joint was observed. However including the thermoelastic effects showed overall the joint aperture will increase, which indicated the thermoelastic effects were dominant.

This simplified model can be improved by utilizing a pressure dependent leak-off formulation (e.g. Ghassemi and Zhang, 2005), which could allow for leak-off to be realistically and rigorously incorporated into sub-model (ii). Also, the coupling between temperature and pressure can be considered. Sub-model (i) can be further enhanced by incorporation of a two dimensional heat extraction solution (e.g. Cheng et al., 2001), and sub-model (ii) can be further enhanced by incorporation of a three dimensional heat extraction solution (e.g. Ghassemi et al., 2003). It is also realized that use of two or three dimensional elasticity in the formulation of the induced width changes can yield more accurate results which can preserve certain conclusions, and reveal other aspects of thermo-poroelastic phenomena. For example, ahead of the tensile stresses exists an area of compressional stresses (Ghassemi et al. 2005). This is due to the strain compatibility condition. Since in a one dimensional formulation it is assumed $u_x = 0$ and $e_{xx} = 0$, the zone of compression can not be taken into account.

APPENDIX A
Derivation of Cubic Law

The geometry for this problem is seen in Figure 70. The constant aperture of the fracture is w_o, the length of the fracture is L, and the height of the fracture is h. The fracture walls are treated as smooth impermeable parallel plates.

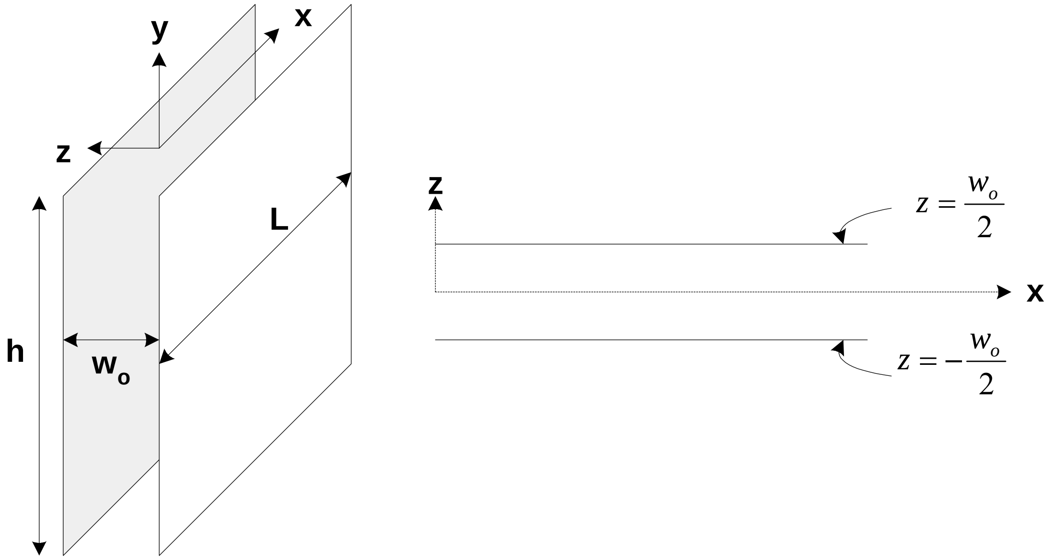

Figure 70. Geometry and Problem Set up for Cubic Law Derivation.

It will be assumed the injection fluid, water, behaves as a Newtonian fluid, and the flow is laminar. These assumptions allow for the fluid flow to be governed by the Navier-Stokes Equation:

$$\rho_f\left(\frac{\partial}{\partial t}+u\frac{\partial}{\partial x}+v\frac{\partial}{\partial y}+w\frac{\partial}{\partial z}\right)=\rho_f\vec{\mathbf{F}}-\nabla p+\mu_f\nabla^2\vec{\mathbf{v}}+(\mu_f+\lambda)\nabla(\nabla\cdot\vec{\mathbf{v}}) \qquad \text{(A.1)}$$

where $\nabla\cdot$ is the divergence operator, ∇ is the gradient operator, ∇^2 is the Laplacian operator, u, v, and w are components of the velocity vector $\vec{v}$ in the x, y, and z directions respectively, $\vec{\mathbf{F}}$ is the body force vector, and λ is the second viscosity coefficient. Since water is relatively incompressible, changes in the density can be ignored. This implies no change in the velocity components with respect to their spatial directions. Therefore the last term in (A.1) on the left hand side is zero. Furthermore it will be assumed the walls are impermeable, this implies at the fracture surface the velocity is zero. Although there is a three dimensional velocity distribution we can ignore the velocity distribution in the *z* direction since the $L >> w_o$ ($w = 0 \rightarrow \partial p/\partial z = 0$). Finally assuming body forces, $\vec{\mathbf{F}} = 0$, (ie gravity, heat, electromagnetic) are negligible (A.1) can be written in a two dimensional form as:

$$\begin{aligned} \rho_f\left(\frac{\partial u}{\partial t} + u\frac{\partial u}{\partial x} + v\frac{\partial u}{\partial y}\right) &= \mu_f \nabla^2 u - \frac{\partial p}{\partial x} \\ \rho_f\left(\frac{\partial v}{\partial t} + u\frac{\partial v}{\partial x} + v\frac{\partial v}{\partial y}\right) &= \mu_f \nabla^2 v - \frac{\partial p}{\partial y} \end{aligned} \tag{A.2}$$

The next assumption will be steady state flow, which will imply the time derivatives in (A.2) will go to zero. This assumption also results in negligible changes for velocity in the direction of flow. This then implies $\frac{\partial u}{\partial x} = \frac{\partial u}{\partial y} = \frac{\partial v}{\partial x} = \frac{\partial v}{\partial y} = 0$. However the velocity changes in the direction of flow are not negligible, thus (A.2) now becomes:

$$\begin{aligned} \frac{\partial p}{\partial x} &= \mu_f \frac{\partial^2 u}{\partial z^2} \\ \frac{\partial p}{\partial y} &= \mu_f \frac{\partial^2 v}{\partial z^2} \end{aligned} \tag{A.3}$$

Eqn. (A.3) is the solution system requiring two boundary conditions given as:

$$\left.\frac{\partial u}{\partial z}\right|_{z=0} = \left.\frac{\partial v}{\partial z}\right|_{z=0} = 0 \tag{A.4}$$

$$u = v = 0\Big|_{z=\frac{w_o}{2}} \tag{A.5}$$

Eqn. (A.4) is a result of a symmetry assumption which occurs at the center of the flow regime. Eqn. (A.5) is a result of the zero velocity condition at the fracture walls.

To solve (A.3) each are integrated to give expressions for the velocity in terms of the pressure gradient:

$$\begin{aligned} u &= \frac{z^2}{2\mu_f}\frac{\partial p}{\partial x} + C_1 z + C_2 \\ v &= \frac{z^2}{2\mu_f}\frac{\partial p}{\partial y} + C_3 z + C_4 \end{aligned} \tag{A.6}$$

Applying (A.4) result in C_2 and C_4 being zero, and (A.5) result in C_1 and C_3 being zero. Now using the fact z is defined over the interval from 0 to $w_o/2$, (A.6) can be written as:

$$\begin{aligned} u &= \frac{1}{2\mu_f}\left(z^2 - \frac{w_o^2}{4}\right)\frac{\partial p}{\partial x} \\ v &= \frac{1}{2\mu_f}\left(z^2 - \frac{w_o^2}{4}\right)\frac{\partial p}{\partial y} \end{aligned} \tag{A.7}$$

Eqn. (A.7) shows the velocity profile is parabolic, which is a laminar flow velocity. Since (A.7) has velocity components that change across the fracture aperture, it is of interest to find the average velocity, which is accomplished by integrating the velocity components over the entire fracture, and dividing by the fracture aperture:

$$\begin{aligned} \bar{u} &= \frac{1}{2\mu_f w_o}\frac{\partial p}{\partial x}\int_{-w_o/2}^{w_o/2}\left(z^2 - \frac{w_o^2}{4}\right)dz = \frac{z^3}{3} - \frac{w_o^2 z}{4}\Bigg|_{z=-w_o/2}^{z=w_o/2} = \frac{2w_o{}^3}{24} - \frac{6w_o{}^3}{24} = -\frac{w_o^2}{12\mu_f}\frac{\partial p}{\partial x} \\ \bar{v} &= \frac{1}{2\mu_f w_o}\frac{\partial p}{\partial y}\int_{-w_o/2}^{w_o/2}\left(z^2 - \frac{w_o^2}{4}\right)dz = \frac{z^3}{3} - \frac{w_o^2 z}{4}\Bigg|_{z=-w_o/2}^{z=w_o/2} = \frac{2w_o{}^3}{24} - \frac{6w_o{}^3}{24} = -\frac{w_o^2}{12\mu_f}\frac{\partial p}{\partial y} \end{aligned} \tag{A.8}$$

Multiplication of (A.8) by the cross sectional area and expressing as a flow rate per unit height yields the cubic law:

$$
\begin{aligned}
q_x &= -\frac{w_o^3}{12\mu_f}\frac{\partial p}{\partial x} \\
q_y &= -\frac{w_o^3}{12\mu_f}\frac{\partial p}{\partial y}
\end{aligned}
\tag{A.9}
$$

APPENDIX B
Derivation of Thermoporoelastic Displacement Equation

First, we will introduce of static equilibrium condition which is a result of the displacement and stress conditions satisfying Newton's 2nd Law:

$$\frac{\partial \sigma_{xx}}{\partial x} = 0 \qquad \frac{\partial \sigma_{yy}}{\partial y} = 0 \qquad \frac{\partial \sigma_{xy}}{\partial y} = 0 \qquad \frac{\partial \sigma_{yx}}{\partial x} = 0 \tag{B.1}$$

where σ is stress. Let us also define strain (e) in terms of displacements ($\bar{\mathbf{u}}$):

$$e_{xx} = \frac{\partial u_x}{\partial x} \qquad e_{yy} = \frac{\partial u_y}{\partial y} \qquad e_{xy} = \frac{1}{2}\left(\frac{\partial u_x}{\partial y} + \frac{\partial u_y}{\partial x}\right) \qquad e_{yx} = \frac{1}{2}\left(\frac{\partial u_y}{\partial x} + \frac{\partial u_x}{\partial y}\right) \tag{B.2}$$

Eqns. (B.2) are compatibility equations which state that continuity exists in the strain field. A complete derivation of Eqns. (B.1) and (B.2) can be found in Boresi et al. (1993), and are not developed here because of the length involved in there derivations. In order to relate (B.1) and (B.2) a constitutive relation must be used. Hooke's Law for thermoporoelasticity is:

$$\begin{aligned}
\sigma_{xx} &= 2G\left(e_{xx} + \frac{v}{1-2v}\left(e_{xx} + e_{yy}\right) - \frac{(1+v)\alpha_T}{1-2v} T(x,y) - \alpha p(x,y)\right) \\
\sigma_{yy} &= 2G\left(e_{yy} + \frac{v}{1-2v}\left(e_{xx} + e_{yy}\right) - \frac{(1+v)\alpha_T}{1-2v} T(x,y) - \alpha p(x,y)\right) \\
\sigma_{xy} &= 2Ge_{xy} \qquad \sigma_{yx} = 2Ge_{yx}
\end{aligned} \tag{B.3}$$

where G is the shear modulus, v is Poisson's ratio, α_T is the linear expansion coefficient, T is the temperature ,p is pressure, α is Biot's effective stress coefficient and δ_{ij} is the Kronecker delta. Note the shear stresses are functions of elasticity only.

Since it is of interest to relate the displacement caused by the loading for the above conditions in (A.1), (A.2), and (A.3) let us substitute (A.2) into (A.3):

$$
\begin{aligned}
\sigma_{xx} &= 2G\left(\frac{\partial u_x}{\partial x}+\frac{v}{1-2v}\left(\frac{\partial u_x}{\partial x}+\frac{\partial u_y}{\partial y}\right)-\frac{(1+v)\alpha_T}{1-2v}T(x,y)-\alpha p(x,y)\right)\\
\sigma_{yy} &= 2G\left(\frac{\partial u_y}{\partial y}+\frac{v}{1-2v}\left(\frac{\partial u_x}{\partial x}+\frac{\partial u_y}{\partial y}\right)-\frac{(1+v)\alpha_T}{1-2v}T(x,y)-\alpha p(x,y)\right) \qquad \text{(B.4)}\\
\sigma_{xy} &= 2G\frac{1}{2}\left(\frac{\partial u_x}{\partial y}+\frac{\partial u_y}{\partial x}\right) \qquad \sigma_{yx} = 2G\frac{1}{2}\left(\frac{\partial u_y}{\partial x}+\frac{\partial u_x}{\partial y}\right)
\end{aligned}
$$

We now apply the static equilibrium conditions to (A.4) by (A.1):

$$
\begin{aligned}
\frac{\partial \sigma_{xx}}{\partial x} &= 2G\left(\frac{\partial^2 u_x}{\partial x^2}+\frac{v}{1-2v}\left(\frac{\partial^2 u_x}{\partial x^2}+\frac{\partial u_y}{\partial y \partial x}\right)-\frac{(1+v)\alpha_T}{1-2v}\frac{\partial T}{\partial x}-\alpha\frac{\partial p}{\partial y}\right)=0\\
\frac{\partial \sigma_{yy}}{\partial y} &= 2G\left(\frac{\partial^2 u_y}{\partial y^2}+\frac{v}{1-2v}\left(\frac{\partial u_x}{\partial x \partial y}+\frac{\partial^2 u_y}{\partial y^2}\right)-\frac{(1+v)\alpha_T}{1-2v}\frac{\partial T}{\partial y}-\alpha\frac{\partial p}{\partial y}\right)=0 \qquad \text{(B.5)}\\
\sigma_{xy} &= 2G\frac{1}{2}\left(\frac{\partial^2 u_x}{\partial y^2}+\frac{\partial u_y}{\partial x \partial y}\right)=0 \qquad \sigma_{yx} = 2G\frac{1}{2}\left(\frac{\partial^2 u_y}{\partial x^2}+\frac{\partial u_x}{\partial y \partial x}\right)=0
\end{aligned}
$$

Note that in (B.5) *T* = *T*(*x*,*y*) and *p* = *p*(*x*,*y*). We now sum all the equations in (B.5) setting them equal to zero and dividing by 2G:

$$
\begin{aligned}
&\left(\frac{\partial^2 u_x}{\partial x^2}+\frac{v}{1-2v}\left(\frac{\partial^2 u_x}{\partial x^2}+\frac{\partial u_y}{\partial y \partial x}\right)-\frac{(1+v)\alpha_T}{1-2v}\frac{\partial T}{\partial x}-\alpha\frac{\partial p}{\partial y}\right)\\
&+\left(\frac{\partial^2 u_y}{\partial y^2}+\frac{v}{1-2v}\left(\frac{\partial u_x}{\partial x \partial y}+\frac{\partial^2 u_y}{\partial y^2}\right)-\frac{(1+v)\alpha_T}{1-2v}\frac{\partial T}{\partial y}-\alpha\frac{\partial p}{\partial y}\right) \qquad \text{(B.6)}\\
&+\frac{1}{2}\left(\frac{\partial^2 u_y}{\partial x^2}+\frac{\partial u_x}{\partial y \partial x}\right)+\frac{1}{2}\left(\frac{\partial^2 u_x}{\partial y^2}+\frac{\partial u_y}{\partial y \partial x}\right)=0
\end{aligned}
$$

Eqn. (B.6) needs algebraic manipulation. First we note the last two expressions in (B.6) must be equal by symmetry of the strain tensor, therefore each of the components are equal to each other. Taking this into consideration we write:

$$\left(\frac{\partial^2 u_x}{\partial x^2}+\frac{\partial^2 u_y}{\partial y^2}+\frac{\partial^2 u_y}{\partial x^2}+\frac{\partial^2 u_x}{\partial y^2}\right)+\frac{v}{1-2v}\left(\frac{\partial^2 u_x}{\partial x^2}+\frac{\partial^2 u_y}{\partial y \partial x}+\frac{\partial^2 u_x}{\partial x \partial y}+\frac{\partial^2 u_y}{\partial y^2}\right)$$
$$-\frac{(1+v)\alpha_T}{1-2v}\left(\frac{\partial T}{\partial x}+\frac{\partial T}{\partial y}\right)-\alpha\left(\frac{\partial p}{\partial x}+\frac{\partial p}{\partial y}\right)=0 \quad \text{(B.7)}$$

Since we are dealing with a vector $\vec{\mathbf{u}}$ it is noteworthy to introduce the vector operators. First we define the divergence of the vector $\vec{\mathbf{u}}$:

$$\nabla \cdot \vec{\mathbf{u}}=\frac{\partial u_x}{\partial x}+\frac{\partial u_y}{\partial y} \quad \text{(B.8)}$$

and applying the gradient operator to result in:

$$\nabla[\nabla \cdot \vec{\mathbf{u}}]=\frac{\partial}{\partial x}\left(\frac{\partial u_x}{\partial x}+\frac{\partial u_y}{\partial y}\right)+\frac{\partial}{\partial y}\left(\frac{\partial u_x}{\partial x}+\frac{\partial u_y}{\partial y}\right) \quad \text{(B.9)}$$

The Laplacian of a vector field is:

$$\nabla^2 \vec{\mathbf{u}}=\frac{\partial^2 u_x}{\partial x^2}+\frac{\partial^2 u_y}{\partial y^2}+\frac{\partial^2 u_y}{\partial x^2}+\frac{\partial^2 u_x}{\partial y^2} \quad \text{(B.10)}$$

Thus substitution of (B.9) and (B.10), multiplying by G and noting

$K = 2G(1+v) / [3(1-2v)]$ yields:

$$G\nabla^2 \vec{\mathbf{u}}+\frac{G}{1-2v}\nabla[\nabla \cdot \vec{\mathbf{u}}]=3K\alpha_T \nabla T+\alpha \nabla p \quad \text{(B.11)}$$

APPENDIX C

Explanation of Influence Coefficient A_{ij}

To better illustrate the influence coefficient, we will consider a 4 x 4 matrix of Eqn. (117):

$$\begin{bmatrix} \overline{P}_1 \\ \overline{P}_1 \\ \overline{P}_3 \\ \overline{P}_4 \end{bmatrix} = \begin{bmatrix} A_{11} & A_{21} & A_{31} & A_{41} \\ A_{12} & A_{22} & A_{32} & A_{42} \\ A_{13} & A_{23} & A_{33} & A_{43} \\ A_{14} & A_{24} & A_{34} & A_{44} \end{bmatrix} \times \left[(\omega_1 - 1) \quad (\omega_2 - 1) \quad (\omega_3 - 1) \quad (\omega_4 - 1)\right] \tag{C.1}$$

From (C.1) we can write the following relationships:

$$\overline{P}_1 = A_{11}(\omega_1 - 1) + A_{21}(\omega_2 - 1) + A_{31}(\omega_3 - 1) + A_{41}(\omega_4 - 1) \tag{C.2}$$

$$\overline{P}_2 = A_{12}(\omega_1 - 1) + A_{22}(\omega_2 - 1) + A_{32}(\omega_3 - 1) + A_{42}(\omega_4 - 1) \tag{C.3}$$

$$\overline{P}_3 = A_{13}(\omega_1 - 1) + A_{23}(\omega_2 - 1) + A_{33}(\omega_3 - 1) + A_{43}(\omega_4 - 1) \tag{C.4}$$

$$\overline{P}_4 = A_{14}(\omega_1 - 1) + A_{24}(\omega_2 - 1) + A_{34}(\omega_3 - 1) + A_{44}(\omega_4 - 1) \tag{C.5}$$

It follows that (C.2)-(C.5) are four equations with four unknowns (ω_1 through ω_4), because the influence matrix *A* is known from the discretization and problem geometry and $\overline{P}$ is known from the discretized flow equation (Eqn. 120 and 121). Indeed substitution of *n* in place of 4 in (C.1) would result in (117) and (118). More importantly it illustrates that the DD method utilizes the superposition of all the individual displacement discontinuities to determine the overall displacement at each node. It is also realized that the superposition principle in reality becomes the discretized form of the integral in Eqn. (113).

REFERENCES

Abe, H., H. Niitsuma, and H. Murphy, 1999. Summary of discussions, structured academic review of HDR/HWR reservoirs. *Geothermics*, v. 28, pp. 671-979.

Abou-Sayed, A. S., C. E. Bretchel, and R. J. Clifton, 1978. In situ stress determination by hydrofracturing: a fracture mechanics approach. *J. Geophys. Res.*, v. 83, pp. 2851-2862.

Adachi, J. I., and E. Detournay, 2002. Self-similar solution of a plane-strain fracture driven by a power-law fluid. *Int. J. Numer. Analy. Meth. Geomech.*, v. 26, pp. 579-604.

Adams, M., J. Moore, S. Bjornstad, and D. Norman, 2000. Geologic History of the Coso Geothermal System. *GRC Transactions*, v. 24, p. 205-209.

Atkinson, P. G., 1998. A continuing evolution. *GRC Bulletin*, August/September issue.

Barton, C., D. Moos., and M. D. Zoback, 1995. Fluid flow along potentially active faults in crystalline rock. *Geology*, v. 23, p. 683-687.

Barton, C., and M. D. Zoback, 1994. Stress perturbations associated with active faults penetrated by boreholes: possible evidence for near complete stress drop and a new technique for stress magnitude measurement. *J. Geophys. Res.*, v. 99, pp. 9373-9390.

Barton, C., S. H. Hickman, R. Morin, and M. D. Zoback, 1998. Reservoir-scale fracture permeability in the Dixie Valley, Nevada, Geothermal Field, paper SPE 10911.

Barton, N., 1976. The shear strength of rock and rock joints. *Int. J. Rock Mech. Min. Sci. & Geomech. Abstr.* v. 13, 255-279.

Barton, N., and V. Choubey, 1977. The shear strength of rock joints in theory and practice. *Rock Mech.*, v. 10, 1-54.

Barton, N., and S. Bandis, 1980. Some effects of scale on the shear strength of joints. *Int. J. Rock Mech. Min. Sci. & Geomech. Abstr.*, v. 17, 69-73.

Baumgartner, J., and R. Jung, 1998. in Kaltschmitt and Huengens (Ed.), Enrgiegewinnung aus Erdwarme, Deutscher Verlag fur Grundstoffindustrie.

Bodvarsson G., 1969. On the temperature of water flowing through fractures. *J. Geophy. Res.* v. 74, no. 8; 1987-1992.

Boresi, A. P., R. J. Schmidt, and O. M. Sidebottom, 1993. Advanced Mechanics of Materials, 5th edition, John Wiley & Sons: NY, NY.

Bower, K. M., and G. Zyvoloski, 1997. A numerical model for thermo-hydro-mechanical coupling in fractured rock. *Int. J. of Rock Mech. and Min. Sci.*, v. 34, pp. 1201-1211.

Brudy, M., and M. D. Zoback, 1999. Drilling-induced tensile wall-fractures: Implications for determination of in-situ stress orientation and magnitude, *Int. J. Rock Mech. & Min. Sci.*, v. 36, no. 2, pp. 191-215.

Calfrac Well Services Limited. Calfrac Resources: *Oil Field Services Glossary*. Retrieved June, 2005 from the World Wide Web: http://www.calfrac.com/glossary.php?list=L&category=General

Cheng, A. H.-D., and A. Ghassemi, 2001. Effect of fluid leak off on heat extraction from a fracture in hot dry rock, GRC 2001 Annual Meeting.

Cheng, A. H-D., A. Ghassemi, and E. Detournay, 2001. Integral equation solution of heat extraction from a fracture in hot dry rock. *Int. J. Numer. Analy. Meth. Geomech.*, v. 25, 1327-1338.

Crouch, S. L, A. Starfield, 1983. *Boundary Element Methods in Solid Mechanics*. NY, NY: Routledge.

Detournay, E., and R. Carbonell, 1994. Fracture mechanics analysis of the breakdown process in minifrac or leak-off tests. *SPE/ISRM Eurock 94*, The Netherlands.

Duchane, D., and Brown, D., 2002. Hot Dry Rock (HDR) geothermal energy research and development at Fenton Hill, New Mexico. *GRC Bulletin*, December issue, pp. 15-19.

Edwardson, M. J., H. M. Girner, H. R. Parkinson, H.R. Williams, and C.S. Matthews, 1962. Calculation of formation temperature disturbances caused by mud circulation, *J. of Pet. Tech.*, April, pp. 416-426.

Ghassemi, A. and A. H-D. Cheng, 2005. Solution of heat extraction from hot dry rock by mesh reduction techniques. Manuscript in preparation.

Ghassemi, A. and Q. Zhang, 2004. Poro-thermoelastic Mechanisms in Wellbore Stability & Reservoir Stimulation. *29th Stanford Geothermal Workshop*, Stanford, 2004.

Ghassemi, A., S. Tarasovs, and A. H.-D., Cheng, 2003. An integral equation solution for three-dimensional heat extraction from planar fracture in hot dry rock. *Int. J. Numer. Analy. Meth. Geomech.*, v. 27, pp. 989-1004.

Ghassemi, A., S. Tarasovs, and A. D.-H Cheng, 2005. Integral equation solution of heat extraction induced thermal stress in enhanced geothermal reservoirs. *Int. J. Num. Analy. Meth. Geomech.* v. 29, pp. 829-844.

Goodman, R.E., 1980. *Introduction to Rock Mechanics 2nd Edition*, John Wiley & Sons: NY, NY, p. 165.

Gringarten, A. C., P. A. Witherspoon, and Y. Ohnishi, 1975. Theory of heat extraction from fractured hot dry rock. *J. Geophy. Res.*, v. 80, pp 1120-1124.

Hadamard, J., 1923. *Lectures on Cauchy's Problem in Linear Partial Differential Equations*. New Haven, CT: Yale University Press.

Haimson, B., and C. Fairhurst, 1967. Initiation and extension of hydraulic fracture in rocks. *Soc. Petro. Eng. J.*, September, pp.310-318.

Haimson, B., 1968. Hydraulic fracturing in porous and non-porous rock and its potential for determining in-situ stresses at great depth. Ph.D. thesis, University of Minnesota.

Hayashi, K., and Ito T., 2003. Role of stress-controlled flow pathways in HDR geothermal reservoirs. *Pure and Applied Geophysics* 160, p. 1103-1124.

Hubbert, M., and D. Willis, 1957. Mechanisms of hydraulic fracturing. *Trans. Am. Inst. Min. Engrs.*, v. 210, pp. 153-168.

Jaegar, J.C., and N.W, Cook, 1979. *Fundamentals of Rock Mechanics 3rd Edition*, Chapman and Hall: London, England.

Jeffrey R. G., van As, A., 2003. Hydraulic fracture growth in naturally fractured rock mine though mapping and analysis. *NARMS-TAC*, Toronto, Canada.

Jung, R., J. Baumgartner, O. Kappelmeyer, F. Rummel, and H. Tenzer, 1997. HDR-technologie-geothermische energiegewinnung der Zukunft., Geowissenschaften 15, heft 8, Ernst and Sohn.

Kohl, T., K. F. Evans, R. J. Hopkirk, and L. Ryback, 1995. Coupled hydraulic, thermal, and mechanical considerations for the simulation of hot dry rock reservoirs. *Geothermics*, v. 24, pp. 345-359

Kolditz, O., 1995. Modeling flow and heat transfer in fractured rocks: Dimensional effect of matrix heat diffusion. *Geothermics*, v. 24, pp. 421-437

Kolditz, O., and C. Clauser, 1998. Numerical simulation of flow and heat transfer in fractured crystalline rocks: Application to the hot dry rock site in Rosemanowes (U.K.). *Geothermics*, v. 27, pp.1-23.

Kumar, S., and A. Ghassemi, (in-press). Numerical modeling of non-isothermal quartz dissolution and precipitation in a coupled fracture-matrix system. *Geothermics*.

Lowell, R. P., 1976. Comments on Theory of heat extraction from fractured hot dry rock by A.C Gringarten, P. A. Witherspoon, and Y. Ohnishi. *J. of Geophy. Res.*, v. 81, pp. 359-360.

McTigue, D., 1986. Thermoelastic response of fluid-saturated porous rock. *J. Geophys. Res.*, v. 91, pp. 9533-9542.

Monastero, F. C., 2002. Model for Success. *GRC Bulletin*, September/October, pp. 188-194.

Moos, D., and M. D. Zoback, 1990. Utilization of observations of well bore failure to constrain the orientation and magnitude of crustal stresses: Application to continental, deep sea drilling project and ocean drilling program boreholes. *J. Geophys. Res.*, v. 95, pp. 9305-9325.

Mossop, A. and P. Segall, in press. Injection induced stresses in geothermal fields. *J. Geophys. Res*.

Murphy, H., D. Brown, R. Jung, I. Matsunaga, R. Parker, 1999. Hydraulics and well testing of engineered geothermal reservoirs. *Geothermics*, v. 28, pp. 491-506.

Paris, P. C., and G. C. Sih, 1965. Stress analysis of cracks. In: *Fracture Toughness Testing and its Applications*. American Society for Testing and Materials. pp. 30-83.

Pine, R. J., and A. S. Batchelor, 1984. Downward migration of shearing in jointed rock during hydraulic injections. *Int. J. Rock Mech. Min. Sci. & Geomech. Abstr*., v. 21, no. 5, pp. 249-63.

Pine, R. J., P. Ledingham, and C. M. Merrifield, 1983. In situ stress measurement in the Carnmenellis granite-II. Hydrofracture tests at Rosemanowes quarry to depths of 2000 m. *Int. J. Rock Mech. Min Sci. and Geomech. Abstr.*, v. 20, pp. 63-72.

Potter, R. M., E. S. Robinson, M. C. Smith, 1974. Method of extracting heat from dry geothermal reservoirs, US Patent #3,786,858.

Ritchie, R. H., and A.Y. Sakakura, 1956. Asymptotic expansions of solutions of the heat conduction equation in internally bounded cylindrical geometry. *J. App. Phy.,* v. 27, no. 12, pp. 1453-1459.

Rose, P., S. Hickman, C. Barton, J. McCulloch, J. Moore, K. Kovac, C. Kasteler, M. Adams, M. Mella, P. Wannamaker, D. Ekart, B. Julian, G. Foulger, P. Swanson, S. Gosavi, J. Sheridan, P. Spielman, K. Richards-Dinger, F Monastero, R. Weidler, and S. Baisch, 2003. Creation of an Enhanced Geothermal System through Hydraulic and Thermal Stimulation. University of Utah Energy and Geoscience Inst. Annual Report.

Rose, P., S. Hickman, C. Barton, J. McCulloch, J. Moore, K. Kovac, C. Kasteler, M. Adams, M. Mella, P. Wannamaker, D. Ekart, B. Julian, G. Foulger, P. Swanson, S. Gosavi, J. Sheridan, P. Spielman, K. Richards-Dinger, F Monastero, R. Weidler, and S. Baisch, 2004. Creation of an Enhanced Geothermal System through Hydraulic and Thermal Stimulation. University of Utah Energy and Geoscience Inst. March Quarterly Report.

Rummel, F., 1987. Fracture mechanics approach to hydraulic fracturing stress measurements. In: Atkinson BK. editor. *Fracture Mechanics of Rock.* London: Academic Press, pp. 217-40.

Rummel, F., O. Kappelmeyer, and O.A. Herde, 1992. Geothermal energy, future energy source? Facts-research-future, MesyGmbH (Ed.) Bochum.

Savitski, A., 2001. Injection of a viscous fluid in a joint. Progress Report to the Department of Geology and Geological Engineering, University of North Dakota.

Sheridan J., K. Kovac, P. Rose, C. Barton, J. McCulloch, B. Berard, J. Moore, S. Petty, and P. Spielman. 2003. In situ stress, fracture and fluid flow analysis-east flank of the Coso geothermal field. 28th Stanford Geothermal Workshop, Stanford, Ca, pp. 34-49.

Sheridan J., and S. Hickman, 2004. In situ stress, fracture, and fluid flow analysis in well 38C-9: An enhanced geothermal system in the Coso Geothermal Field. 29th Stanford Geothermal Workshop, Stanford, California, pp. 268-276.

Sneddon, I. N, 1946. The distribution of stress in the neighborhood of a crack in an elastic solid. *Proc. Roy. Soc. London*, Ser. A, v. 187, pp. 227-260.

Sneddon, I. N., Lowengrub M., 1969. *Crack Problems in the Classical Theory of Elasticity*. Wiley: NY, NY.

Stehfast, H., 1970. Numerical inversion of Laplace transforms. *Comm. ACM*, v. 13, p. 47-49, 624.

Stephens G., B. Voight, 1982. Hydraulic fracturing theory for conditions of thermal stress. *Int. J. Rock Mech. and Min. Sci*., v. 19, pp. 279-84.

Tenzer, H., 2001. Development of hot dry rock technology. *GRC Bulletin*, December, pp 14-22.

Tester, J., D. W. Brown, R. M. Potter, 1989. Hot dry rock geothermal energy-A new energy agenda for the 21st century. Los Alamos National Laboratory report LA-11514-MS.

United States Department of Energy Office of Energy Efficiency and Renewable Energy: Geothermal Technologies Program. *A history of geothermal energy in the United States*. Retrieved June, 2005 from the World Wide Web: http://www.eere.energy.gov/geothermal/history.html

United States Department of Energy Office of Energy Efficiency and Renewable Energy: Geothermal Technologies Program. *Enhanced Geothermal Systems*. Retrieved June, 2005 from the World Wide Web: http://www.eere.energy.gov/geothermal/pdfs/egs.pdf

Wang, Y., and E. Papamichos, 1994. Conductive heat flow and thermal induced fluid flow around a wellbore in a poroelastic medium. *Water Resources Research,* v. 30, pp. 3375-3384.

Zoback M. D., F. Rummel, R. Jung, C. Raleigh, 1977. Laboratory hydraulic fracturing experiments in intact and pre-fractured rock. *Int. J. Rock. Mech. Min. Sci. and Geomech. Abstr*. v. 14, pp. 46-58.